Ph.D. Thesis

VERY HIGH ENERGY GAMMA-RAY ASTRONOMY WITH THE ARGO-YBJ DETECTOR: SENSITIVITY TO POINT-LIKE SOURCES.

Candidate: Carla Bleve

Advisor: Dr. Daniele Martello

Coordinator: Prof. Boris Konopelchenko

Università degli Studi di Lecce - Dipartimento di Fisica
Dottorato di Ricerca in Fisica - XV ciclo
August 2003

Università degli Studi di Lecce
Dottorato di ricerca in fisica - XV ciclo

Sommario della Tesi

Very High Energy γ-ray astronomy with the ARGO-YBJ detector: sensitivity to point-like sources.

Candidato: Carla Bleve
Tutore: Dott. Daniele Martello

Questa tesi è stata sviluppata nell'ambito dell'esperimento ARGO–YBJ, un osservatorio per la rivelazione della radiazione cosmica attualmente in costruzione in Tibet. L'obiettivo principale dell'esperimento è lo studio delle sorgenti di raggi γ ad energie superiori ai 100 GeV.
Questo lavoro di ricerca è incentrato sullo sviluppo e lo studio dei metodi per la ricostruzione degli eventi e per l'analisi dei dati finalizzata alla rivelazione di sorgenti puntiformi di raggi γ di energia molto elevata (VHE).

Il primo capitolo è dedicato a una introduzione generale alla γ–astronomia e alle sue motivazioni fisiche. Dopo una breve panoramica sullo stato attuale delle osservazioni e sulle sorgenti di raggi γ VHE, vengono descritte le tecniche sperimentali utilizzate per la γ-astronomia di alta energia con particolare attenzione ai rivelatori *ground–based*.

Il secondo capitolo fornisce una descrizione tecnica del rivelatore ARGO–YBJ; sono descritte in particolare le caratteristiche peculiari che consentono una osservazione continua del cielo con una soglia energetica più bassa di circa un ordine di grandezza rispetto ai tradizionali rivelatori di sciami atmosferici. Viene poi presentato lo stato attuale dell'esperimento e viene delineato schematicamente il problema dell'analisi dati. Un'analisi dei diversi fattori che intervengono nella sensibilità dell'apparato consente, infine, di introdurre e giustificare un criterio per il confronto degli algoritmi di

ricostruzione degli eventi.

Nel terzo capitolo sono illustrate in dettaglio le simulazioni Monte Carlo di sciami indotti da γ, protoni e nuclei di elio effettuate per questo lavoro. Più di 70 milioni di eventi sono stati simulati in modo tale da riprodurre le distribuzioni attese per gli eventi reali. Un sistema di pesi viene usato per tenere conto dello spettro e del moto di una sorgente puntiforme generica. Una stima delle rate di trigger per gli eventi segnale e gli eventi di fondo viene data nel caso della Crab Nebula, la sorgente considerata la "candela standard" per la γ–astronomia.

Nel quarto e quinto capitolo sono descritti in dettaglio gli algoritmi sviluppati nell'ambito del programma di analisi dati dell'esperimento per ricostruire la posizione del core di uno sciame (Cap.4) e la direzione della particella primaria (Cap.5). Viene quindi fatto un primo confronto fra i diversi metodi ed è discussa la dipendenza della ricostruzione da diversi parametri rilevanti quali l'angolo di zenith, la posizione del core e la molteplicità dell'evento. Viene anche studiata la possibilità di usare la ricostruzione del core per la reiezione degli eventi esterni tramite un opportuno taglio di area. Una valutazione del contributo dei diversi passi di ricostruzione alla sensibilità dell'apparato mostra che la loro interdipendenza richiede, per un confronto completo, uno studio congiunto dell'intera catena di ricostruzione.

Nell'ultimo capitolo è affrontato il problema di stimare la sensibilità del rivelatore ARGO–YBJ. Per prima cosa viene determinata una strategia di analisi ottimale applicando il criterio, scelto nel secondo capitolo, di rendere massima la sensibilità alla Crab Nebula. I passi di ricostruzione descritti nei capitoli precedenti sono combinati in catene di ricostruzione e confrontati utilizzando due diversi approcci per la trattazione dei dati. La procedura per determinare l'analisi migliore conduce infine alla stima della sensibilità alla Crab Nebula. Tenendo conto delle incertezze sul flusso della sorgente e sul flusso del fondo viene valutato l'errore su tale stima. Infine la sensibilità a una sorgente generica è stimata in funzione del suo flusso, dell'indice spettrale e della posizione.

Università degli Studi di Lecce
Dottorato di ricerca in fisica - XV ciclo

Summary of the Thesis

Very High Energy γ-ray astronomy with the ARGO-YBJ detector: sensitivity to point-like sources.

Candidate: Carla Bleve
Advisor: Dr. Daniele Martello

The present thesis has been developed in the ARGO–YBJ experiment, an observatory for cosmic radiation presently under construction in Tibet. The main physical issue of the experiment is to detect the sources of γ-rays at a threshold energy of about 100 GeV.
This research has been concentrating on the development and the study of event reconstruction and data analysis methods for the detection of point sources of very high energy (VHE) γ–rays.

The first chapter is dedicated to a general introduction to VHE γ-ray astronomy and to the physical motivations for this discipline. After a short review on the present status of the observations and on the known emitters of VHE γ–rays, experimental techniques are described with particular attention to ground–based detectors.

The second chapter provides a technical description of the ARGO–YBJ detector focused on the distinctive features that allow for a continuous all-sky monitor at a threshold energy that is unprecedented for an air–shower array. The present status of the experiment is then presented and the event reconstruction and data–analysis problems are outlined. On the basis of the different contributions to the detector sensitivity, a criterion for the algorithm comparison is presented and justified.

The Monte Carlo simulations of extensive air showers performed for this

work (initiated by γ, protons and helium nuclei) are detailed in the third chapter. More than 70 million events have been simulated in a manner that allows to reproduce the expected distributions of real events. A system of weights is applied to take into account the spectrum and motion of a point source of γ–rays. The estimate of signal and background trigger rates is given in the case of the Crab Nebula, the "standard candle" for γ–ray astronomy.

The fourth and fifth chapters give a full description of the algorithms developed and implemented in the ARGO–YBJ analysis code for the reconstruction of the shower core position (Ch.4) and of the primary particle direction (Ch.5). A first comparison among different methods is carried out and the dependence of the reconstruction on a number of relevant parameters (zenith angle, true core position, event multiplicity) is discussed. Further, the possibility of using the reconstructed core position for the identification of external showers, through an appropriate area cut, is evaluated. The contribution of each reconstruction method to the detection sensitivity is discussed and it is shown that reconstruction steps and events selections have to be studied simultaneously due their complex interplay.

In the last chapter the problem of estimating the ARGO–YBJ sensitivity is addressed. Firstly an optimized event reconstruction strategy is found by applying the criterion of maximizing the sensitivity to the Crab Nebula. The reconstruction steps described in the previous chapters are combined into reconstruction chains and compared making use of two different strategies to treat data. The procedure for determining the best analysis gives in turn an estimate of the sensitivity to the Crab Nebula. The error on this estimate is then quantified by taking into account the uncertainties on the source and background flux. Finally, the expected sensitivity for a detection of a generic source is studied as a function of its flux, spectral index and position.

Contents

Acknowledgements

There are many people who have played an important role in my career as a Ph.D. student. I'm grateful to all of them.

First and foremost I would like to thank my advisor Dr. Daniele Martello for having spent long hours in evaluating my ideas, revising this thesis and answering to my questions. His physics knowledge together with his patience has been essential to the development of this work. In particular I appreciated his invaluable help when I was getting started with C++ programming.

I would also like to thank Prof. Giovanni Mancarella for having always found the time to ask me how the work was going on. Since I was an undergraduate student he has been teaching me what does it mean doing scientific research.

The members of the ARGO–YBJ Collaboration also deserve thanks: this thesis could not be written without the work of all of them. In particular I am in debt to Dr. Paola Celio for her technical help with simulations, to Dr. Antonio Surdo and Prof. Paolo Bernardini who patiently gave me full details about the detector response and trigger simulation, to Dr. Silvia Vernetto and Dr. Pino Di Sciascio for having checked step by step the results I was obtaining, for their suggestions and constructive criticism.

Next, I would like to thank all the people with whom I shared my room at University during these three years, in particular Lorenzo and Giovanni.

I owe a great deal of gratitude to Mrs. Adriana Rugge and her numerous family who were my neighbours for eight years. They always treated me like one of them.

Last but not least I thank my family. This thesis is dedicated to my grandmother Enza for her encouragements and unconditioned support.

Chapter 1

Introduction to VHE γ-ray Astronomy.

During the last 15 years γ-astronomy has emerged as a powerful tool to gain insight into a number of physical problems related with the most extreme phenomena that occur in the Universe including the origin and acceleration mechanisms of Cosmic Rays and the study of the last stages of stellar evolution (Supernova Remnants, neutron stars, black holes, etc.).
This chapter provides a short introduction to VHE γ-ray astronomy (as defined in the next section) with digressions about the HE range. After an overview of the field, the sources and detection techniques will be described.

1.1 Definition of terms.

Photons with energy > 0.511 MeV are known as γ-rays. The high-energy domain (above 30 MeV) spans several decades in the highest end of the observable electromagnetic spectrum, thus requiring different detection techniques. For this reason the high energy γ-ray spectrum is conventionally divided into subranges approximately corresponding to the energy bands over which the different experimental techniques are used (see Tab.1.1 and Fig.1.1). It should be noted that the boundaries of these energy regions are very loose due to the rapid developments of the detection strategies.

To date, no source emitting γ-rays above 50 TeV has been detected: nitrogen fluorescence detectors are used to observe the highest energy cosmic rays and will not be considered here.

High Energy (HE)	30 MeV - 30 GeV
Very High Energy (VHE)	30 GeV - 30 TeV
Ultra High Energy (UHE)	30 TeV - 30 PeV
Extremely High Energy (EHE)	>30 PeV

Table 1.1: *Conventional subdivisions of the γ-ray spectrum* [1].

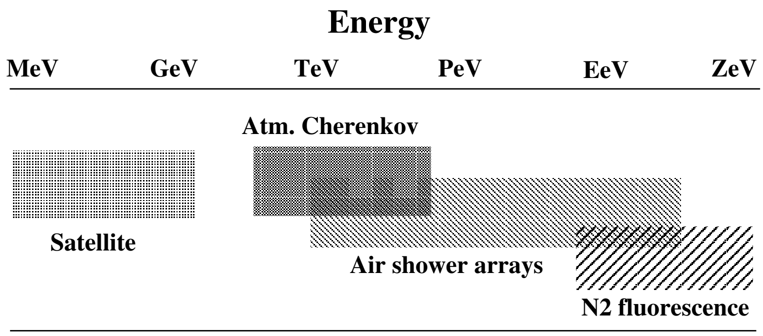

Figure 1.1: *Detection techniques used to observe γ-rays in different energy ranges* [2].

1.2 A broad overview.

VHE γ-ray astronomy was born as a viable branch of the main stream astronomy with the development of the imaging Cherenkov telescopes. This technical improvement in the detection methods allowed in 1989 for the first observation of the Crab Nebula with 9 standard deviations statistical significance (Whipple Collaboration [3]).
The next important development for the HE/VHE γ-ray astronomy was the successful launch of the NASA Compton Gamma Ray Observatory (CGRO), in 1991, whose results provided indications of what may be bright in the VHE sky.

1.2.1 Present status of HE/VHE observations.

The EGRET instrument aboard CGRO detected more than 250 sources with γ-rays at energies between 100 MeV and 30 GeV. Fig.1.2 shows a galactic map of the γ-ray point sources detected by EGRET as published in their third catalogue [4] based on $\sim$4 years of observation (April 1991 - October 1995). The identified sources consist of 5 pulsars, 1 solar flare, 66 high–

confidence blazars identifications, 27 possible blazars, 1 radio galaxy (Cen A) and the Large Magellanic Cloud (LMC). The remaining 170 sources, mostly located along the galactic plane, are not yet identified with known objects, since they have no observed counterparts at other wavelengths.

Despite the large number of sources detected by EGRET, only 14 sources (plus 2 additional claimed observations) have been observed since 1989 in the VHE range at energies above 200 GeV. Their locations in galactic coordinates are shown in Fig.1.3. Of the 14 confirmed/probable sources, 3 are plerions, 3 are shell–type supernova remnants, 6 are active galactic nuclei, 1 is a starburst galaxy and 1 source is unidentified.

The limited number of known objects compared with those detected in the lower energy range by EGRET, indicates that our present knowledge of the VHE sky is far from being complete and that only the brightest sources have been detected. However the observations are rapidly increasing (remarkably 6 of the 14 sources have been discovered in the past three years).

A number of new improved experiments are on–going or planned for the next years. Their main goals are:

- to improve the flux sensitivity (for the detection of fainter objects)
- to achieve a continuous monitoring of the whole sky
- to bridge the energy range between 20 GeV and 200 GeV that has been only marginally observed

1.2.2 Scientific motivations for VHE γ–ray astronomy.

There are many phenomena in the Universe that may produce TeV γ-rays; the list of 14 known emitters contains indeed at least 4 different types of sources, both galactic and extragalactic. Therefore, the first motivation for VHE γ–astronomy is the phenomenology of these astrophysical sources. From this point of view this field can be regarded as the natural extension of the optical observations toward the highest energies.

Since non-thermal spectra are a common feature of the observed VHE sources, observations of TeV sources can provide constraints on the models of objects in which acceleration and radiation processes occur at extreme astrophysical conditions. An additional intriguing perspective is the possible discovery of new kinds of sources.

An important related topic is the origin of Cosmic Rays (CRs). If γ-rays are produced in hadronic interactions they can provide a proof (together with neutrinos) of the acceleration of these charged particles. Since they are not

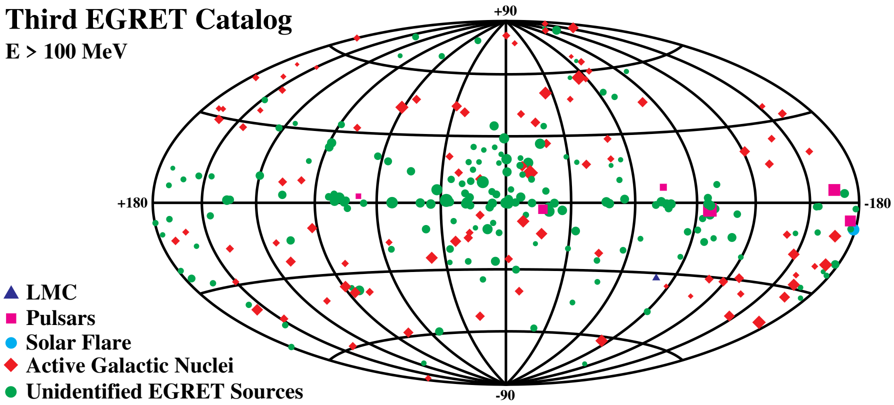

Figure 1.2: *catalogue in galactic coordinates of the γ–ray point sources detected by EGRET above 100 MeV. The size of each symbol is proportional to the source intensity* [5].

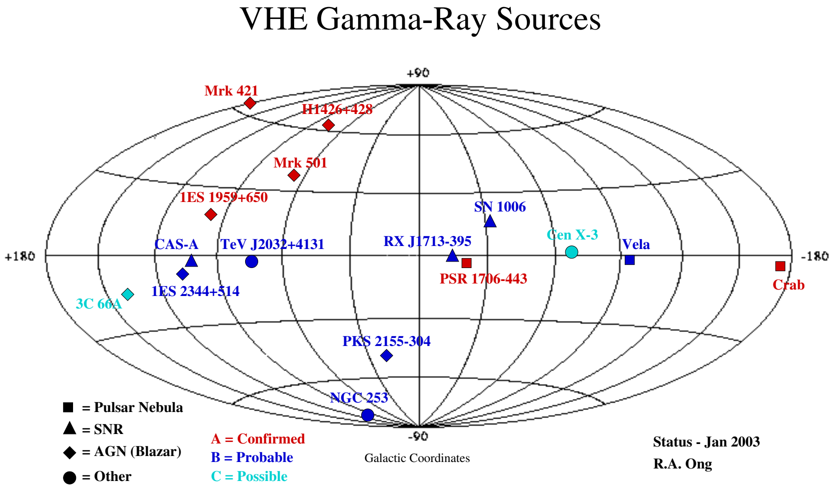

Figure 1.3: *Galactic map of the VHE sky. The detected sources are classified as Confirmed (A) if detected at high significance levels by different experiments, Probable (B) if detected by one group at high sensitivity level, Possible (C) in the case of a single claimed observation to be confirmed* [6]

deviated by magnetic fields, their detection allows to trace back the sources of CRs. The attention is focused both on galactic (SNRs) and extragalactic (AGNs) possible sources.
TeV γ-astronomy may also shed light on cosmology (e.g. through the measurement of the infrared background radiation or the study of primordial black holes) and particle physics beyond the Standard Model (e.g. possible evidence of supersymmetric particles).

What emerges is the depiction of a field in rapid evolution, addressing a wide range of physical issues and with strong links to other fields (ν-astronomy, cosmic rays, etc.). The number of present and planned experiments demonstrates the growing interest of the scientific community in VHE γ–ray astronomy.

1.3 Physical processes that produce γ-rays.

To understand which astrophysical sources can be viewed in the VHE sky, is useful to start from a more fundamental question: what kind of elementary known processes produce high energy γ–rays?
The most important are:

1. Bremsstrahlung
2. Synchrotron radiation
3. Inverse Compton Scattering (IC)
4. Decay of neutral pions

Bremsstrahlung is the emission of a photon by a charged particle with energy E accelerated in the Coulomb field of a nucleus. The energy E_γ of the emitted photon is equal to the change in kinetic energy of the charged particle. If the parent particle has a power-law spectrum, the resulting γ-ray spectrum is itself a power-law and has the same spectral index ($N(E) \sim E^{-\alpha} \rightarrow N_\gamma(E_\gamma) \sim E_\gamma^{-\alpha}$).

Synchrotron photons are radiated by a charged particle with energy E moving relativistically in a magnetic field H. In this case the energy E_γ of the photon is $\propto H^2\gamma^2$ where $\gamma = 1/\sqrt{1-(v/c)^2}$ is the Lorentz factor of the parent particle. As in the case of Bremsstrahlung, a power law spectrum results from a parent power law spectrum ($N_{parent}(E) \sim E^{-\alpha} \rightarrow N_\gamma(E_\gamma) \sim E_\gamma^{-\beta}$) but the index changes: $\beta = (\alpha+1)/2$. Synchrotron radiation by sufficiently high energy electrons can produce HE γ–rays, but most of the synchrotron radiation is emitted in the radio and X–ray range and is responsible for much of the non-thermal broadband emission observed from many astrophysical sources.

Processes (1) and (2) occur with electrons and protons, however in the latter case are rather inefficient due to the higher mass of the proton ($m_p/m_e = 1836$) since the radiated energy is $\propto 1/m^2$.

VHE (and UHE) photons are mainly produced by processes (3) and (4). In (3) an ambient photon with low energy ϵ is scattered to very high energy by a relativistic electron. If E_e is the energy of the electron and γ its Lorentz factor, the energy of the Compton boosted photon is:

$$E_\gamma \sim \epsilon\gamma^2 \text{ if } \gamma\epsilon \ll m_e c^2$$
$$E_\gamma \sim E_e \text{ if } \gamma\epsilon \gg m_e c^2$$

The two extreme cases correspond to an energy of the photon in the rest frame of the relativistic electron respectively much lower or much higher than the electron mass. If α (β) is the spectral index of electrons (photons) the following relations hold in the two cases: $\beta = (\alpha + 1)/2$ and $\beta \sim \alpha$. This pure electromagnetic process is important when the density of ambient photons is high. If the ambient photons come from the synchrotron radiation of the electrons themselves, the process is called *Synchrotron Self-Compton* (SSC). This mechanism is very efficient in transferring energy from electrons to photons.

The interaction of protons with matter[1] produces neutral pions which in turn decay mainly into photons via $\pi^0 \rightarrow \gamma + \gamma$ with a lifetime of about $1.68 \times 10^{-16} s$ (process (4)). The resulting spectrum roughly follows the same power law of the protons ($N_p(E_p) \sim E_p^{-\alpha} \rightarrow N_\pi(E_\pi) \sim E_\pi^{-\alpha} \rightarrow N_\gamma(E_\gamma) \sim E_\gamma^{-\alpha}$) and the energy of the photons is about 5-10% of the proton energy. VHE and UHE γ-rays can therefore result from the hadronic interactions of protons with sufficiently high energy. In the hypothesis of hadronic collisions also charged pions are produced. In this case neutrinos are emitted as well as γ-rays.

The processes described above require an acceleration mechanism capable to provide a beam of high-energy parent particles and a sufficiently dense medium in which they can interact.

[1] Pions are also produced in the interaction of hadrons with the 2.7 K cosmic background radiation. This process is relevant at extragalactic distances and produces EHE γ–rays.

1.4 VHE sources

1.4.1 Supernova Remnants.

When a massive star ends its life a Supernova (SN) explosion takes place. The stellar core collapses and the outer layers of the progenitor star are blown off. What remains after the explosion is a compact object, which can be a neutron star or a black hole depending upon its mass. The SN explosion itself drives a blast wave into the interstellar medium (ISM), which results in an expanding shell of hot shocked material called Supernova Remnant (SNR). SNRs are classified as Plerions if the progenitor star becomes a Pulsar (discussed in the next section) or as shell-type characterized by the emission from the roughly spherical shell bounding the remnant.

In the SN explosion there is an energy release of roughly 10^{53} erg, most of which is radiated in the form of neutrinos. This means that the SNR has a total energy of $\sim 10^{51}$ erg. The shock wave can accelerate particles by a mechanism known as Diffusive Shock Acceleration (DSA) [7], a realization of first order Fermi acceleration [8]. Energetics favour these objects as candidate sources of CRs up to the knee (around 10^{15} eV). Following the famous argument of Ginzburg and Syrovatskii [9]: since a SN occurs in our Galaxy once every 30-50 years, the power emitted by SNRs is $\approx 10^{51}$ erg $/10^9$ s $=$ 10^{42} erg s^{-1}. If a small percentage of the energy goes into the acceleration of protons and hadrons the power emitted in CRs by the Milky Way ($\approx 10^{40}$ erg s^{-1}) is energetically explained. Moreover, taking into account that the CR spectrum as observed at Earth is modified by the transport of CR in the galaxy, the source spectrum should have an index 2.2 [15] remarkably close to the value of 2.0 expected from DSA. Despite of these arguments, however, the observed VHE γ-ray spectra of the detected shell-type SRNs (SN1006, RXJ 1713-3946, Cassiopeia A) can be explained with pure leptonic models with no compelling evidence of accelerated hadrons.

1.4.2 Pulsars.

Pulsars are rapidly rotating neutron stars with typical periods ranging from few milliseconds to about ten seconds. They are characterized by strong magnetic fields ($\sim 10^{12}$ Gauss) and relativistic jets of plasma and radiation streaming from their magnetic poles. The name is due to the radio and X–ray pulsed emission observed from the jets as they rotate on an axis (not aligned with the magnetic axis) through the line of sight of a terrestrial observer. To date, no pulsed emission has been detected in the TeV range.

However, VHE unpulsed emission has been observed from three plerions (Crab Nebula, PSR 1706-44, Vela). Models of plerions indicate that TeV photons are produced in the surrounding nebula by relativistic electrons powered by the central pulsar. SSC emission by these electrons can explain the observed spectra.

Crab Nebula

The brightest and best known source detected at TeV energies is the Crab Nebula. This plerion is the remnant of a SN exploded in 1054. At its centre there is a young optical pulsar surrounded by a ~ 4 pc extended nebula.
Since the first observation by the Whipple group [3], at least 8 different experiments have detected VHE steady emission from the Crab Nebula up to 50 TeV with no evidence for a cutoff. The energy spectrum is relatively well determined and is characterized by a falling power law with differential index ~ 2.5 (see Tab.1.2). Multiwavelength measurements of the unpulsed γ–ray emission are summarized in Fig.1.4. This spectrum can be explained in terms of pure leptonic production: the lower energy bump is due to synchrotron emission by electrons, the second bump by SSC [10].

Since the Crab flux is strong and steady, this source has become the "standard candle" for VHE γ–ray astronomy. Observation of the Crab are used to demonstrate that an experiment works, and to refine the data-analysis methods.

Measurement	$I_0 \times 10^{-12}$ $(TeV^{-1}cm^{-2}s^{-1})$	E_0 (TeV)	α
HEGRA [11]	27.9±0.2±5	1.0	2.59±0.06
WHIPPLE [12]	32.0±1.7±6	1.0	2.49±0.07
CANGAROO [13]	0.201±0.036	7.0	2.53±0.18
As–γ [14]	4.61±0.90	3.0	2.62±0.17

Table 1.2: *Measurements of the differential flux from the Crab Nebula as detected by various instruments sensitive to TeV γ–rays. The differential flux is written in the form $I_0\,(E/E_0)^{-\alpha}$. Table shows the differential flux normalization I_0, the median energy E_0 (to which the flux is normalized) and the spectral index α.*

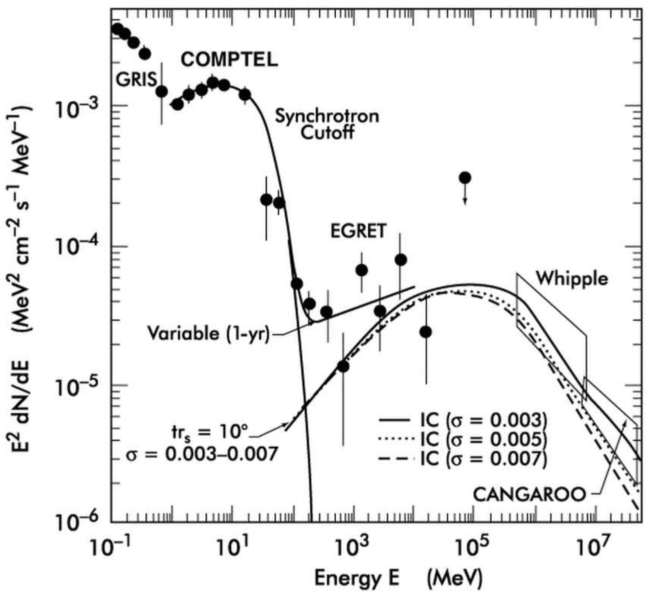

Figure 1.4: *Multiwavelength measurements of the Crab Nebula unpulsed emission compared with the prediction of the SSC model (σ is a parameter of the model).*

1.4.3 Active Galactic Nuclei.

Active Galactic Nuclei (AGN) are the bright central engine of the so-called active galaxies. AGNs are known to emit radiation over the entire electromagnetic spectrum, from radio waves to VHE γ-rays. They are very luminous, extremely compact objects that exhibit large luminosity variations on time scales of hours to years. The behaviour of individual AGNs varies dramatically, thus numerous classes and subclasses of AGNs exist based on the observed optical and radio properties. Nevertheless, a unified model has emerged (Fig.1.5) that includes a central engine, probably a massive black hole, surrounded by an accretion disk and by fast-moving clouds. Under the influence of the strong gravitational field, these clouds emit Doppler broadened lines. A thick torus of gas and dust obscures the central part so that for transverse lines of sight only the narrow–line emitting clouds are seen (since clouds more distant from the centre emit narrower lines) [16]. In radio–loud objects there is in addition a relativistic jet of particles roughly orthogonal to the disk (otherwise the AGN is called radio–quiet). Apart this difference, it is believed that different observed properties are due to different viewing angles with respect to the rotation axis.

All the six AGNs detected in the TeV range belong to the subclass of *blazars*, which represent, within the unified model, $\sim 10\%$ of the radio–loud AGNs (the fraction viewed at angles $\leq 20° - 30°$). The blazars' spectral energy distribution (SED) consists in two components in a double peaked shape (see Fig.1.6). The low energy component is probably due to incoherent synchrotron radiation from relativistic electrons in the jet. For the high energy component there are two models: IC of lower energy seed photons [18] (the most popular is the SSC variation [19] by high–energy electrons themselves) and the proton–initiated cascade model [20]. The latter is appealing since it makes AGNs the natural candidates for extragalactic CR acceleration. However, proton models have difficulty in reproducing the observed rapid flaring activity since protons are massive compared to electrons and are not easily accelerated or cooled.

The AGNs detected at TeV energies are: Mrk421, Mrk501, 1ES2344+514, 1ES1959+650, PKS2155-304 and H1426+428.
Mrk421 and Mrk501 are the two most extensively studied AGN at TeV en-

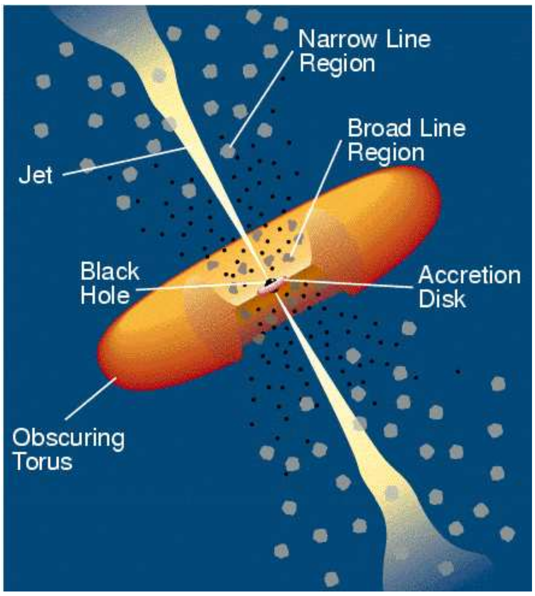

Figure 1.5: *Unified model of AGN. Black hole accretion powers relativistic jets of material. Due to the obscuring torus, we detect emission from sources which are beamed in our line of sight.*

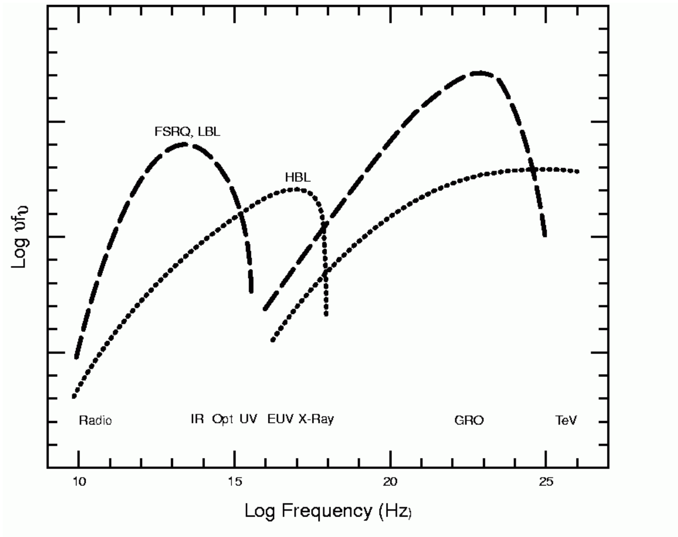

Figure 1.6: *Averague spectral shapes of blazars from radio to TeV γ–rays* [17]. *The two different curves refer to low–frequency peaked (LBL) and high–frequency peaked (HBL) BL-Lacs as defined on the basis of their X–ray to radio fluxes.*

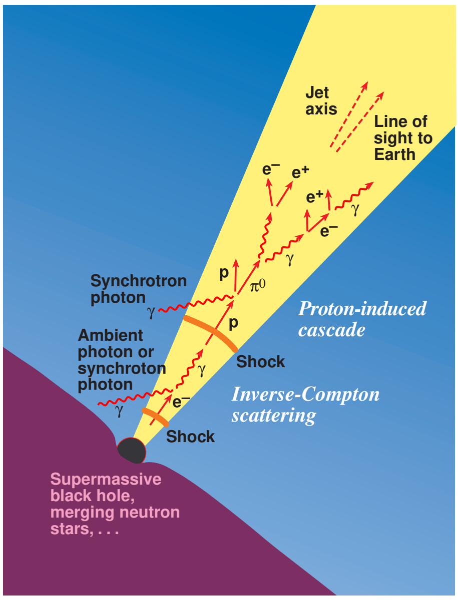

Figure 1.7: *Sketch of the two models for the high energy component of the AGNs' spectral energy distribution. In the jets, electrons or protons are accelerated to high energies via shocks. High energy γ-rays are produced either by IC of electrons or from proton-initiated cascades.*

ergies. The TeV flux found from these objects is characterized by a low quiescent level which can increase dramatically during flaring non-periodic episodes, when they can become the brightest sources of the TeV sky. In Fig.1.8 the dramatic activity period of Mrk501 in 1997 can be seen as detected by the Whipple group.

Further VHE γ-rays observations of AGNs should help to better understand the emission mechanisms and the underlying physical properties of these extreme objects.

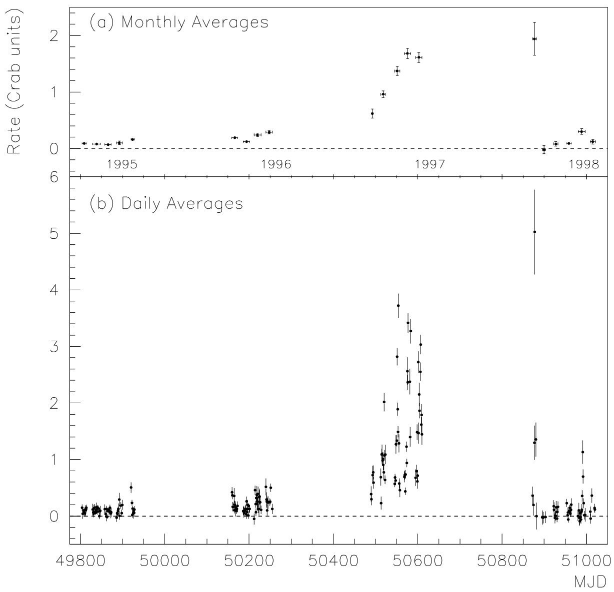

Figure 1.8: *Mrk501 flux as recorded by Whipple during 4 year observation in the energy range 250 GeV- 20 TeV. A dramatic increase in the average flux and in its variability can be seen in 1997* [21].

1.4.4 Other detected sources.

Two other objects complete the catalogue of confirmed/possible VHE sources: the starburst galaxy NGC253 and TeVJ2032+4131.

NGC 253 TeVγ-ray emission has been recently detected by the CANGAROO group [22]. This object is one of the closest starburst galaxies ($\sim$2.5 Mpc), has a very high star formation rate (about 0.3 SN/year) that should imply, in turn, a rate of CR production 10-100 times higher than our galaxy. Hence a high level of diffuse γ-ray emission is expected and is consistent with the spatial extension of the detected emission.

Recently the first unidentified source at TeV energies has been discovered: TeV J2032+41310 (HEGRA [24]). This object shows a steady flux, whose integral above 1 TeV is ~ 0.03 Crab Units, and a differential spectral index ~ -1.9. The most interesting possibility is that this is a new kind of source that does not emit in other wavebands.

1.4.5 Possible sources

Given the small number of known sources, other objects that can be emitters of VHE photons should be examined. Some of them are described below[2].

Unidentified EGRET sources.

It has been mentioned that most of the sources detected by EGRET are unidentified. There has been a great deal of speculation about their nature and presently seems likely that they consist of several classes of objects. Some possibilities include unresolved AGNs, SNRs, and possibly a new type of source [25].

Galactic Plane.

Cosmic Rays are trapped in our Galaxy by Galactic magnetic fields. Their interaction with the interstellar medium through a variety of processes is expected to produce γ-rays in the highest energy regions. Diffuse emission from the galactic plane has been observed up to 30 GeV (EGRET) therefore is likely that a diffuse glow of TeV photons is produced as well.

Gamma Ray Bursts.

Since their discovery 30 years ago thousands of Gamma Ray Bursts (GRBs), short duration (from $1\,ms$ to few ten s) emissions of γ-rays, have been detected. Fig.1.9 shows the map of GRBs detected by BATSE [26] in the energy range between 100 KeV and 1 MeV. At the same time EGRET detected high–energy γ–rays, in some cases with energies above 1 GeV, in

[2]There are other phenomena theoretically predicted that could produce TeV γ–rays e.g. evaporation of primordial black holes and neutralino annihilation. In any case, it is uncertain that if they exist, the associated signal would be observable with current detectors.

coincidence with 6 BATSE GRBs and, most importantly, with no evidence of high–energy cutoff. On the theoretical side, there is an almost general agreement on their cosmological distance[3] while the physics of this objects is not well understood. However, some models predict TeV γ-ray emission. This possibility is strengthened both by the previously mentioned EGRET detections, and by a claimed observation of TeV emission from GRB 970417a with the MILAGRITO detector[4] that could imply an emission above 650 GeV [27] [28].

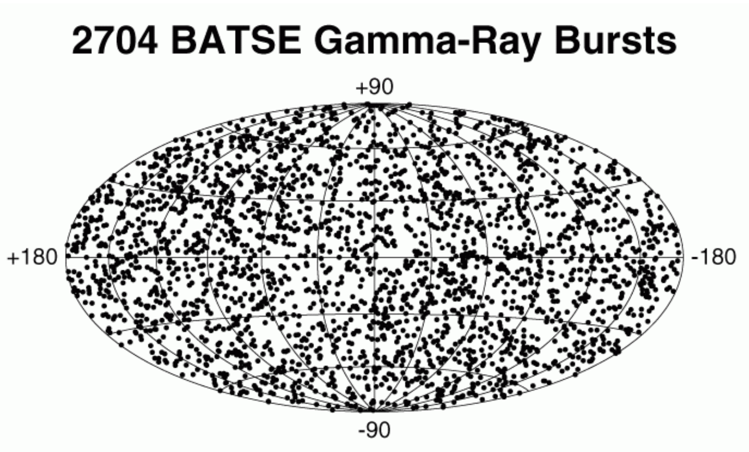

Figure 1.9: *Galactic map of the GRBs detected by BATSE in the energy range 100 KeV-1 GeV. A notable feature is their almost isotropic distribution that suggested cosmological distances of GRBs.*

1.5 Detection techniques.

The detection techniques that can be used in HE/VHE γ–ray astronomy are determined by the properties of the sources and by external disturbing factors:

1. All the known sources exhibit a typical differential spectrum in the

[3]Detections in the X–rays and optical wavebands have given important information. In particular the detection of the optical afterglows has allowed to determine the redshift of about 20 GRBs. These measurements have confirmed that at least these GRBs are at cosmological distances as suggested by their isotropic spatial distribution.

[4]MILAGRITO was a small scale prototype version of MILAGRO, see Sec.1.5.5

form of a rapidly decreasing power–law:

$$\frac{dN}{dE} \propto E^{-\gamma}$$

with $\gamma \sim 2 - 3$.

2. The isotropic CR flux forms a formidable background exceeding by many orders of magnitude even the strongest steady sources flux. It consists largely in protons and heavier nuclei.

3. The Earth's atmosphere is opaque to γ–rays being about 28 radiation lengths thick at sea level. Therefore, γ-rays cannot be directly observed by ground–based detectors.

Given the limitations imposed by this facts, a terrestrial observer can use different strategies to face the problem of the detection.

1.5.1 Satellites

Making use of detectors flown on satellites is the simplest way to avoid the problem of the atmosphere. Satellite detectors consist mainly of a converter layer in which HE photons produce a pair $e^+ e^-$, a tracking detector in which the electron/positron is traced (used to reconstruct the direction of the incident photon with an angular resolution of $\sim 1°$) and a total absorption calorimeter that allows for an energy estimate (resolution ~ 15 %.)
The problem of CR background is solved with a charged particle veto counter that efficiently rejects charged CRs. In the scheme shown in Fig.1.10 the various elements can be recognized.
The strong limitation for this technique is the point (1): since the size of detectors is constrained by the weight that can be placed on satellites, their collection area is ~ 1 m^2. Hence the rapid decreasing of the typical fluxes determines a maximum energy at which the collection area suffices for a statistical significant detection. In the case of EGRET this energy was ~ 30 GeV while the next generation satellite instrument GLAST [29] (shown in Fig.1.10) should be sensitive up to ~ 300 GeV.

1.5.2 Ground–based detection.

In the VHE range the low fluxes and the spectral slope of the typical sources require the use of very large detectors. Therefore, observations must be done from the Earth's surface. Due to the opacity of the atmosphere to VHE photons, only the secondary effects of the atmospheric absorption can

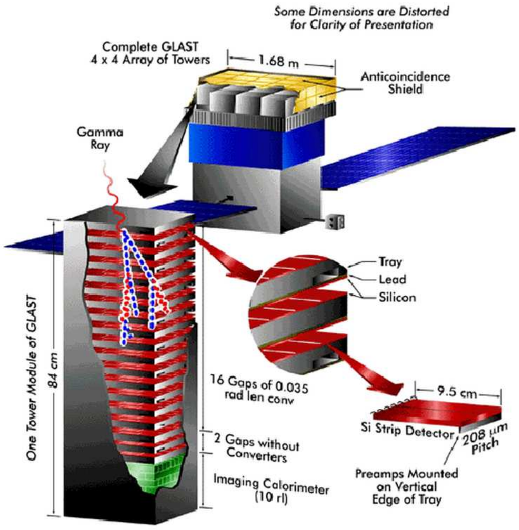

Figure 1.10: *Scheme of the GLAST detector. The silicon strip layers alternated with absorber layers serve as trackers to determine the γ–ray incident direction, the imaging CsI calorimeter is used to reconstruct the energy. The anticoincidence shield (in yellow) allows for an efficient rejection of charged cosmic rays.*

be detected. These detectable effects are the so-called extensive air showers (EAS) and the related emission of Cherenkov light.

Extensive Air Showers

When a photon enters the atmosphere, it interacts with atmospheric nuclei predominantly via pair production. The initial e^+e^- pair produces photons through bremsstrahlung, which in turn convert into more electron-positron pairs and so on. The result is a cascade of particles whose number grows nearly exponentially[5]. The energy of the primary photon is divided among the resulting particles. Therefore, when the mean energy of electrons and positrons goes below the critical energy in air ($\sim$ 85 MeV) ionization losses become predominant and the number of particles gradually decreases.
The lateral extent of such a shower, resulting from multiple Coulomb scattering of electrons and positrons, is of the order of one hundred meters (the actual extent depends on the energy of the photon and on the depth in at-

[5] More details on air showers can be found for example in [30] and [31]

mosphere). Since the particles in the EAS are relativistic, they retain the original direction of the primary particle to a high degree. The result observed at ground level is a large disk of secondary particles, few meters thick and orthogonal to the direction of the primary photon.
The charged CRs also produce EAS superficially not very dissimilar to those induced by photons.

Cherenkov light

Since secondary particles in EAS propagate faster than the local speed of light in air, they emit Cherenkov radiation. Due to the small emission angle ($\sim 0.8°$ at the depth of maximum size, see Fig.1.11), the result at ground level is a light pool similar in size to the front of the EAS, with a density distribution almost flat out to $\sim$ 125 m from the shower axis and with a tight time structure ($\sim$ 5 ns).

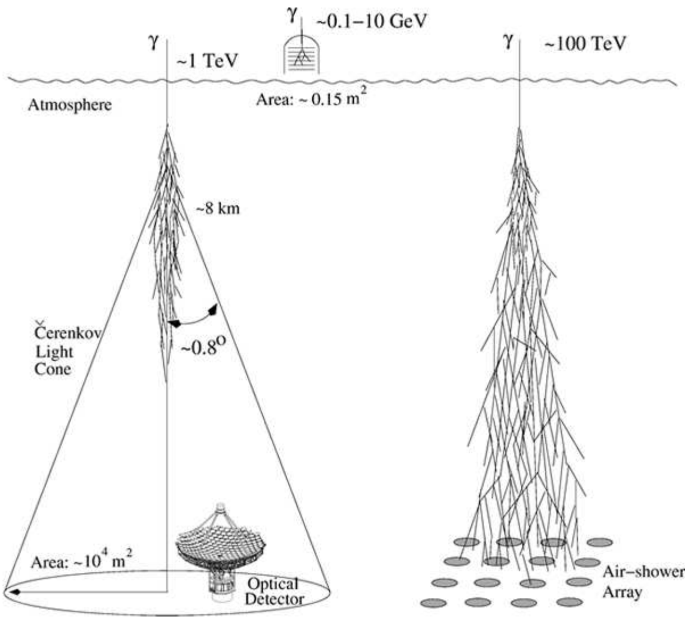

Figure 1.11: *Experimental techniques used for the detection of HE/VHE γ-rays. The picture (not in scale) gives the values of the effective collection areas, and the typical median energy to which the different kinds of detectors are sensitive.*

General characteristics of ground–based detectors.

The ground–based detection of VHE photons is indirect: nature, direction and energy of the primary particle have to be inferred from the measurable properties of the secondary particles (in the case of EAS Arrays) or of the Cherenkov flash (for Cherenkov detectors). In particular, it is not possible to unambiguously identify and reject the charged cosmic ray background. This means that ground–based instruments detect a source as an excess of events from a certain direction over an overwhelming uniform background. For this reason their sensitivities are expressed in units of standard deviations of the CR background:

$$S = \frac{N_\gamma}{\sqrt{N_B}} \tag{1.1}$$

S depends essentially on the angular resolution because, at least for point sources, a better reconstruction of the direction produces a narrower spatial distribution of the signal (see Fig.1.12) which can be more clearly distinguished over the background. In this sense, the pointing of the source is the most effective way to limit the problem (2).
Further improvements in the sensitivity level can be achieved by rejecting part of the background on the basis of subtle differences in the cascades initiated by photons and hadrons.

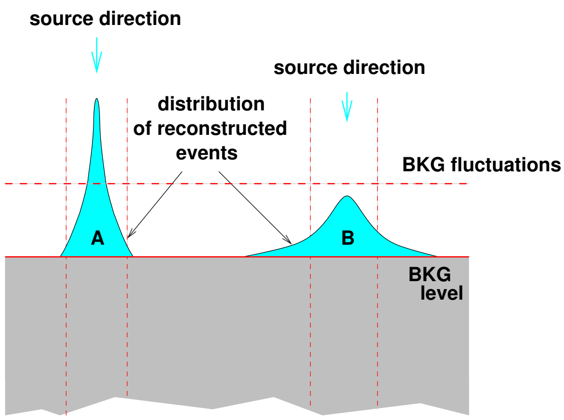

Figure 1.12: *Simplified two dimensional sketch showing that the direction reconstruction results in a distribution of events centred at the true source direction. A good angular resolution produces a narrow distribution (case A) that can be seen as an excess over the background fluctuations while in case B the excess is below the fluctuations level.*

On the other hand, the fact that the atmosphere can be considered a part of the detector itself allows for a further increase of the detection area: due to their lateral extension, EAS can be detected even if they partially intersect the detector active area. Therefore, the collection area of a ground–based detector can be much larger than its geometrical extension.

Together with the angular resolution and the γ/hadron separation, the following relevant properties characterize a ground–based detector:

- energy threshold
  Given a minimum number of secondary particles (or Cherenkov photons) required to trigger the detector, the threshold energy is determined by the atmospheric absorption. This implies that the threshold varies with the zenith angle because of the increasing thickness of atmosphere and that the threshold becomes lower with increasing altitude above sea level.

- field of view (FOV)
  The FOV is the portion of the overhead sky that can be seen at a time. Therefore, it represents the spatial limit for the continuous monitoring of the sky.

- duty cycle
  The fraction of time of actual data taking is the temporal limit to the continuous monitoring of the sky.

As will be shown in the next sections, these characteristics are significantly different in the two cases of atmospheric Cherenkov detectors and EAS arrays.

1.5.3 Atmospheric Cherenkov Telescopes

The most successful instruments in the history of VHE γ–ray astronomy have been the Imaging Atmospheric Cherenkov Telescopes (IACTs). These detectors typically make use of a parabolic or spherical mirror to focus the Cherenkov photons onto a tightly packed array of photomultiplier tubes (PMTs) placed in the focal plane. Properties of the primary particles can be inferred by the resulting image of the shower (see Fig.1.13). IACTs are typically sensitive at energies$> 200 - 300$ GeV, have excellent angular resolution ($\sim 0.1^\circ - 0.15^\circ$) and moderate energy resolution ($\sim 20 - 40\%$). However their excellent results are actually due to their ability to perform an efficient γ/hadron separation using the shape of the image [32]: γ-rays

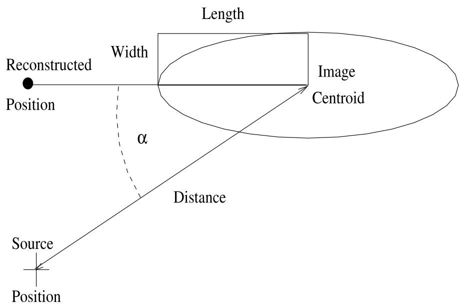

Figure 1.13: *Scheme of the elliptical image produced by an air shower on the pixel camera of a IACT. The point marked as "source position" represents the center of the pixel camera. The Hillas parameters, defined here, are used to perform background rejection.*

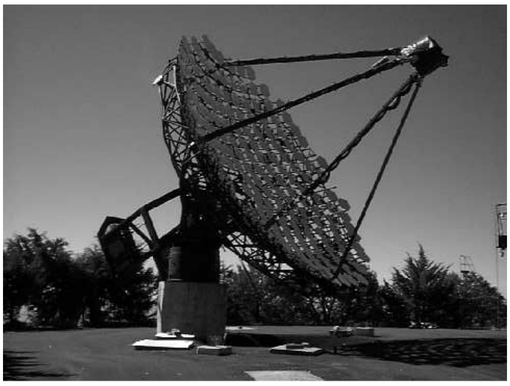

Figure 1.14: *The 10 m diameter Whipple reflector (Mt. Hopkins, US). This detector was the first to successfully experience the imaging technique.*

give a smooth, elliptical image that points toward the centre of the field of view, while CRs images are broader and more chaotic[6]. IACTs can reject more than 99% of the background while retaining $\sim 50\%$ of the signal thus increasing sensitivity by a factor 5.

The most famous IACT is certainly the Whipple telescope (diameter 10 m), which developed the imaging technique. Other successful IACTs are CAT (Pyrenees, 3 m), CANGAROO (Australia, 3.8 m) and HEGRA that

[6]Actually the background rejection makes indirectly use of the direction reconstruction: requiring that the axis of the elliptical image intersects the centre of the FOV is equivalent to the selection of showers whose direction is parallel to the mirror axis (i.e. primary particles coming from the pointed direction). In fact the background rejection is not so good in the case of diffuse sources.

uses 5 mirrors (3 m). The technique is being developed in two different directions: MAGIC will use a single enormous mirror (17 m diameter) to reduce the energy threshold at 20-30 GeV, while experiments like VERITAS (Arizona, 7×12 m mirrors) and HESS (Namibia, 16×12 m) will make use of arrays of traditional reflectors to obtain a stereoscopic view of the shower.

Another group of Cherenkov detectors includes the solar towers: CELESTE, STACEE and Solar2. Pre–existing arrays of heliostat mirrors (used in solar power plants) are utilized to focus the Cherenkov light on a secondary mirror which in turn reflects the radiation onto an array of PMTs. The advantage is the very large mirror area that can be instrumented at low cost. This approach allows reaching low threshold energies (20-50 GeV). Recently the first ground–based observations of the Crab Nebula in this energy range have been published by STACEE [33] and CELESTE [34].

Both IACTs and solar towers have two important limitations. Due to the small FOV ($< 5^\circ$) they must be pointed. Furthermore, they have a low duty cycle (<10%) since Cherenkov radiation can be detected only during moonless cloudless nights. Given that the flux from TeV sources is generally highly variable, these limitations make the identification of new sources and the observation of flaring states of known sources difficult. This is evident in Fig.1.8 where 8 months per year in the Whipple detection of Mrk501 have no experimental points because in those periods the transit of the source occurred during daytime.

1.5.4 Extensive Air Shower Arrays

Instruments that detect the secondary charged particles reaching the ground level are known as EAS arrays. Typically they consist of 50 to 1000 charged particle detectors, usually ~ 1 m^2 scintillation counters, spread over an area of $10^4 - 10^5$ m^2 with a spacing of 10-20 m. The total sensitive area is therefore less than 1% of the total enclosed area. The shower is sampled at a single depth (the observation level) and with an additional sampling of the shower front at fixed points. This results in a high degree of uncertainty in the reconstruction due to fluctuations[7]
The sparse sampling sets the energy threshold ($\sim$ 50 TeV) and determines a poor energy resolution ($\sim$100%). The direction of the incoming primary

[7]For a comparison, Cherenkov detectors record information related to the whole longitudinal and lateral development of the shower summarized by the elliptical image on the pixel camera

particle is reconstructed with the *fast timing* method making use of the relative times at which the individual detection units are fired by the shower front. Also the angular resolution is limited by the shower fluctuations ($\sim 0.5^\circ - 1^\circ$). Measuring the muon content with muon detectors placed around the scintillators performs background rejection. However the ability to discriminate γ and hadron induced showers is quite limited.
In addition the dependence of threshold and reconstruction capabilities on the zenith angle is higher than for Cherenkov detectors: since the active area is horizontal, its projection onto a plane perpendicular to the shower axis is smaller than the geometrical area[8]. On the other hand, EAS arrays have a large field of view ($\sim 2sr$) and a 100% duty cycle. These characteristics give them the capability to serve as all–sky monitors.
To date, however, EAS arrays have only placed upper limits to the fluxes, with the remarkable exception of AS-γ([35]) that has detected at least the Crab Nebula and Mrk501 [36]. In any case, no new source has been discovered by these instruments, primarily because of their high energy threshold.

1.5.5 New generation EAS arrays: Milagro and ARGO–YBJ

In order to meet the requirements of high duty cycle, large field of view and low energy threshold, a variation of the EAS arrays technique is being developed. By making use of *full–coverage* detectors (i.e. the enclosed area is completely instrumented) the Milagro and ARGO–YBJ experiments will be able to perform all-sky monitoring with an energy threshold comparable with the IACTs.

Milagro (Los Alamos, latitude $35^\circ 52' 43''$ North, 2650 m a.s.l.) achieves an energy threshold of 400 GeV by using the water Cherenkov technique [37]. The detector is a covered, light tight pond filled with purified water and instrumented with 723 PMTs deployed in two layers of PMTs (Fig.1.15). Milagro detects the Cherenkov light emitted in water by secondary particles (including photons) reaching the ground level. The upper layer is used to measure the arrival time and density of air shower particles, the lower layer is used to detect penetrating muons for the background rejection.

[8]Cherenkov telescopes point the source therefore their area is always orthogonal to the shower axis. The degradation of the detector performances with zenith is simply due to the increasing thickness of atmosphere.

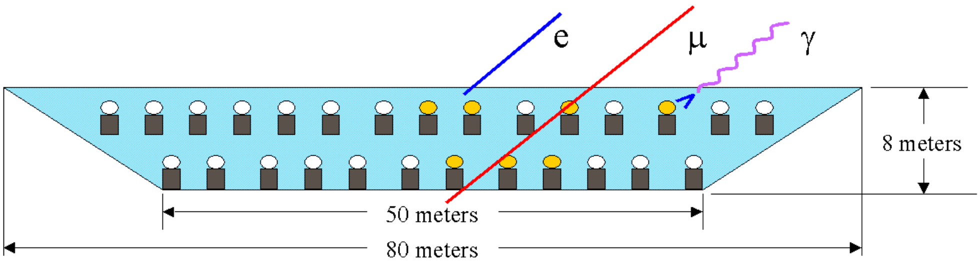

Figure 1.15: *Scheme of the Milagro detector cross-section. PMTs are deployed into a man–made pond filled of water.*

The Milagro group has recently presented the detection of the Crab Nebula [38] at ∼6 standard deviation significance level (referred to about three years data taking) and a first attempt of a sky map, shown in Fig.1.16. Although if the sensitivity is not impressive, important improvements are expected in particular from refinements of the background rejection technique and from an on–going upgrade of the detector.
ARGO–YBJ will be described in the next chapter. With respect to Milagro, it benefits from the much higher altitude (4300 m a.s.l.).

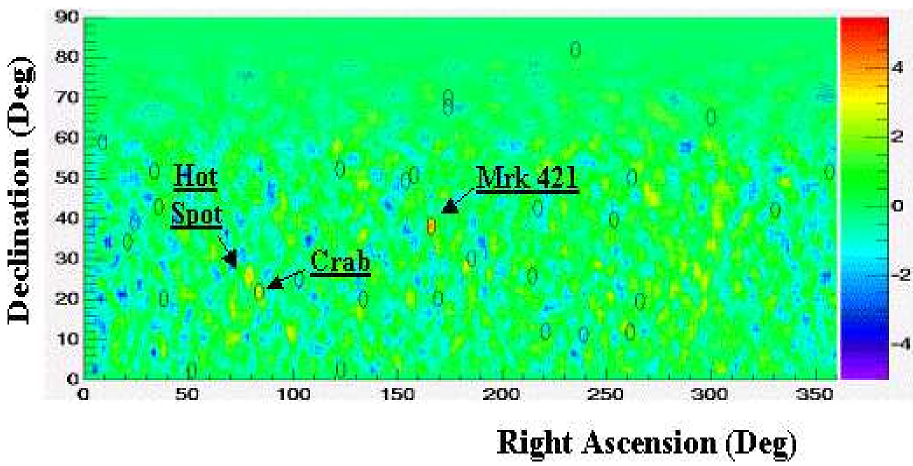

Figure 1.16: *Milagro all-sky survey* [39].

Chapter 2

The ARGO-YBJ Experiment.

The ARGO–YBJ[1] gamma–ray observatory, presently under construction, will be a unique air shower array which, employing a full-coverage technique, will be able to continuously monitor the Northern sky in the declination band $-10^\circ < \delta < 70^\circ$ to search for astrophysical gamma radiation at a low energy threshold (some hundreds GeV) that is unprecedented for an EAS array.

The experimental design is conceived for the detection of small size air showers through the use of a full-coverage carpet of charged particles detectors covering an area of about 6500 m^2, and through the choice of an extremely high altitude (4300 m a.s.l.) location. The full-coverage technique maximizes the percentage of detected charged particles (sampling of $\sim 90\%$ of charged particles falling within the detector area, to be compared with a 1% sampling of traditional EAS arrays). At the same time, the altitude allows to approach the level at which low-energy showers reach their maximum development. The combined effect is a significant lowering of the threshold energy for the shower detection. Furthermore, a high spatial granularity over a continuous large active detection area and an excellent time resolution give to the ARGO–YBJ detector the capability of imaging in space and time the charged particles component of the shower front with high resolution.

The innovative characteristics of the ARGO–YBJ detector allow for the study of a wide range of fundamental issues in cosmic ray and astroparticle

[1]ARGO–YBJ is an acronym for Astroparticle Radiation with a Ground–based Observatory at YangBaiJing

physics [40], among which are:

- γ–ray astronomy at a threshold energy of some hundreds GeV
- Gamma Ray Bursts physics at energies above 10 GeV
- Solar and Heliosphere Physics
- measurement of the antiproton to proton ratio in the TeV range
- measurement of the primary proton spectrum
- studies of the showers properties (e.g. space and time distribution of particles, presence of substructures in the particle distribution)

In particular, with regard to γ–astronomy, ARGO–YBJ conjugates the advantages of EAS arrays such as wide aperture and high duty cycle with a lower energy threshold comparable with current IACTs one. The ability to continuously monitor all sources in overhead sky even during daytime transit make ARGO–YBJ well suited for the possible discovery of unknown sources of VHE photons, but also for the quick identification of flaring states in known sources, as well as for the observation of transient sources.

This chapter provides a brief description of the technical characteristics of the detector and of the present status of the experiment. The data analysis problem addressed to the detection of point γ–ray sources will be introduced at the end of the chapter.

2.1 The ARGO–YBJ detector.

The ARGO–YBJ detector is presently under construction at the Yangbaijing (YBJ) High Altitude Cosmic Ray Laboratories (Tibet, P.R. China). The site is 90 km North-East from Lhasa at latitude $30°06'38''$ N and longitude $90°31'50''$ E (the same location of the AS-γ EAS array). The elevation of 4300 m above sea level corresponds to an atmospheric depth of 606 $\mathrm{g\,cm^{-2}}$ for vertical showers.
The ARGO–YBJ experiment will make use of a full-coverage detector consisting of a layer of single gap Resistive Plate Chambers (RPCs). RPCs allow for the low-cost instrumentation of large areas being particularly suited for an experiment that requires a large active detection area.
The $\sim 78 \times 74$ m^2 of the central carpet are completely covered with 1560

RPCs. The surrounding area, up to $\sim 111 \times 99$ m^2, is partially instrumented with 280 additional RPCs used to enlarge the collection area for showers whose core falls outside the central carpet. Fig.2.1 shows the scheme of the detector

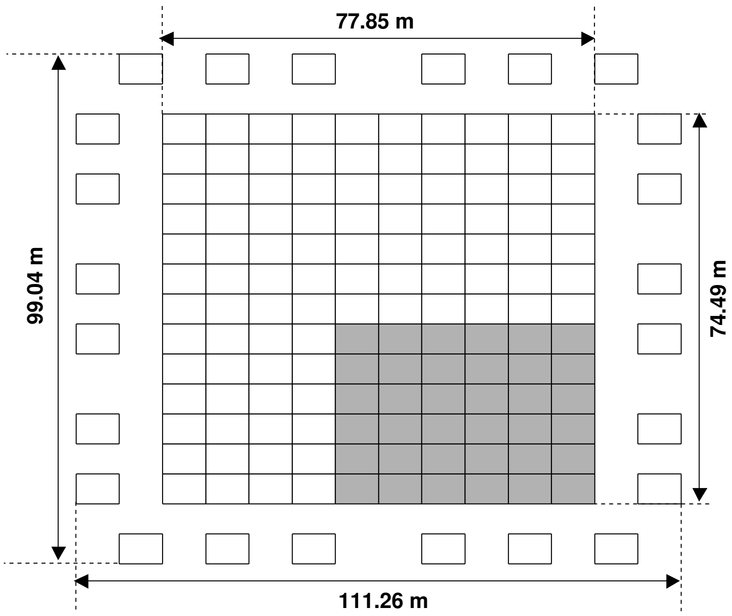

Figure 2.1: *Scheme of the ARGO–YBJ detector. Each rectangle represents a logical unit called Cluster (see text). 36 Clusters, corresponding to the grey area, have been already installed at YBJ and are ready to take data.*

2.1.1 Resistive Plate Chambers

The ARGO–YBJ RPC consists in two bakelite (phenolic polymers with high resistivity $\rho \geq 5 \times 10^{11}\Omega$ cm) electrode plates 2 mm thick whose area is 125×280 cm^2. They are separated by a 2 mm gap filled with gas.
The RPCs operate in streamer mode with a gas mixture of Ar (15%), C_4H_{10} (10%) and $C_2H_2F_4$ (75%) specifically studied for the operation at extreme environmental condition (low atmospheric pressure and low temperature). At the YBJ site, the detection efficiency of charged particles is ~95% at an operating voltage of $\sim$ 7 kV.

The RPC's signal pick–up consists of 80 copper strips 6.7 cm wide and 62 cm long, glued on one side of a 3 mm thick foam sheet with a separation between two adjacent strips of 3.0 mm.

Each RPC is placed in a box of $282 \times 128 \times 7$ cm^3. The box is light (50 kg) self supporting structure consisting of 2 foam layers with Al sheets glued on both surfaces. The box contains the RPC active detector, the pick-up strips and the front–end electronics. On the top of boxes a lead converter and a 5 cm thick layer of foam with 3 mm iron sheets glued on both surfaces are placed (see Fig.2.2).

2.1.2 Lead converter

At the YBJ altitude photons in an air shower are ~ 7 time more numerous than electron/positrons. Therefore a detection of shower photons is desirable. This can be achieved with the use of a layer of dense high Z converter placed on the RPCs. In the case of ARGO–YBJ a lead converter 0.5 cm thick will be used with the following consequences:

- high energy shower photons convert into pairs of detectable particles
- high energy electrons and positrons can undergo multiplicative processes with a further increase in the number of particles traversing the RPCs
- low energy particles are absorbed

The thickness of the lead layer has been chosen in order to achieve an overall gain in the number of the detected particles ($\simeq 1.8$ with respect to the case of no converter used). At the same time, the absorption process removes particles with a large time delay (due to the low energy), thus reducing the intrinsic time spread of the shower front and allowing for a better angular resolution.

2.1.3 DAQ and raw events.

RPCs are the ARGO–YBJ physical detecting units. Nevertheless, the detector is divided into logical units (Fig.2.4) on the basis of the read–out, DAQ and trigger system organization.

Each RPC is logically divided in 10 PADs ($56 \times 65 cm^2$ each) consisting of 8 ORed strips. Logical PADs represent the elementary "pixels" of the ARGO–YBJ detector: their dimensions and time resolution define the space–time granularity of the carpet. The total number of PADs is 15600 in the central carpet (18480 including the ring).

On a larger scale the detector is organized in groups of 12 chambers (6×2) called Clusters (drawn as small rectangles in Fig.2.1). The information of

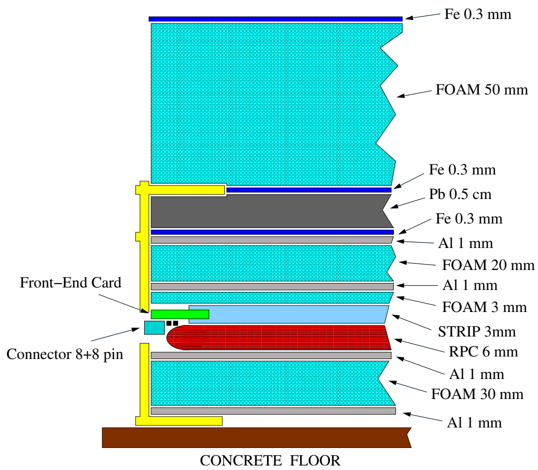

Figure 2.2: *Schematic cross–section of the ARGO–YBJ detector. The upper foam layer is the walking floor.*

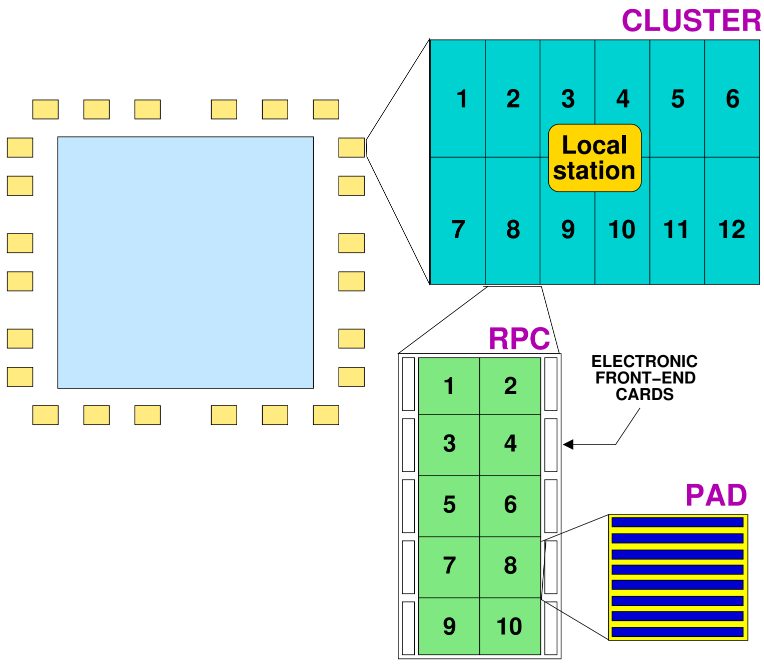

Figure 2.3: *Logical subdivisions of the ARGO–YBJ detector. 18480 PADs (15600 on the central carpet) each with 8 read out strips represent the detector space-time logical pixels. Their dimension are* $\sim 56 \times 62\,cm^2$*, the time resolution is 1 ns.*

a single Cluster is collected and managed by a Local Station. A Central Station collects the information from Local Stations, provides the trigger and manages the data collection.

After the trigger criteria have been met, the information from all the PADs fired within a 2 μs window are recorded to DLT tape and constitute what is called the ARGO–YBJ raw event. The number of fired PADs is called event multiplicity.

The information stored for each fired PAD is:

1. the mask of fired strips within the PAD
2. the PAD time

The number of fired strips (strip multiplicity) is an almost direct measurement of the number of charged particles traversing the PAD's area[2]. The times are read by means of a TDC with a 1 ns bin, operating in common stop. The time resolution is 1 ns, as experimentally determined by means of the coincidence counts of a 3 RPCs small telescope [42].

2.1.4 Trigger logic

Due to ambient radioactivity and hardware effects, the detection of air showers is affected by a high noise rate measured at YBJ as 400 Hz per PAD. Given that the time window opened for a recorded event is 2 μs and assuming that the noise has a Poisson distribution, ~ 12.5 noise hits per event have to be expected on average. In this condition a smart trigger logic is required to reduce the noise contamination. The trigger system makes use of a common clock at 33 MHz. At the level of Local Stations the signal from the 120 PADs of a single Cluster are stretched to 150 ns and their sum is updated every clock cycle. The Cluster logic outputs one of the multiplicity buses when respectively $\geq 1, \geq 2, \geq 3, \geq 4, \geq 5, \geq 6, \geq 7, \geq 16, \geq 32, \geq 64$ PADs are fired in the Cluster. It can be roughly thought as a counting of charged particles in the Cluster in a time coincidence window of 150 ns. The temporal extension of the window corresponds to the maximum time difference that can be expected if particles belonging to a physical shower struck the Cluster area. In the same fashion the Cluster output is stretched

[2]Actually if more than 1 particle hit the same strip there is a certain loss of correspondence between strips and charged particles. However, the probability for this condition to take place is rather small, with the exception of very high multiplicity events.

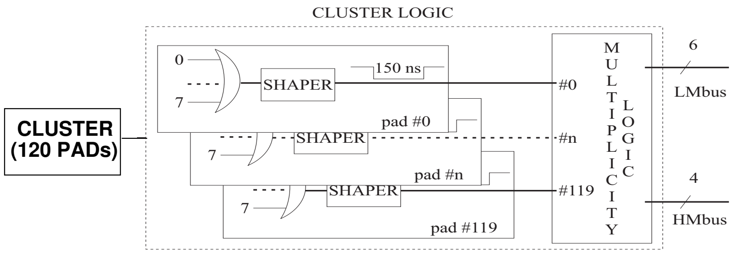

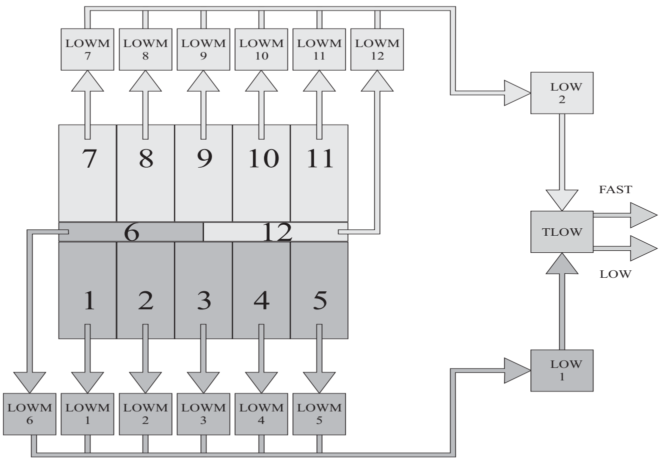

Figure 2.4: *The ARGO–YBJ trigger system. The upper scheme shows the first step: PAD signals are stretched to 150 ns and the Cluster Multiplicity logic outputs a multiplicity bus. Subsequent steps are summarized in the second scheme representing the whole ARGO–YBJ central carpet. Numbered rectangles are groups of 2×6 Clusters (except for number 6 and 12). Different grey scales distinguish the two groups of 65 Clusters (see text).*

to $\sim$ 243 ns and in this coincidence window the multiplicity over a group of 2×6 adjacent Clusters is computed . The same logic is applied to progressively increasing areas and time intervals (65 Clusters in 360 ns, 130 Cluster -the whole central carpet- in 400 ns) (see [41]).

This multilevel logic guarantees that the final sum is over hits meeting specific space-time requirements that characterizes the front of an air shower. The event is retained if this sum is higher than a programmed threshold

M_{trig}.

Note, however, that independently of the trigger multiplicity, all the hits falling into a 2 μs time window are recorded. Therefore the event multiplicity can be higher than the trigger one.

2.1.5 Status of the experiment.

During 1998 a full coverage test carpet of about 50 m^2 was operated at YBJ with the purpose to study the high altitude performance of RPCs and to check the detector capability of imaging a small portion of an air shower with high granularity [42] [43].
Results obtained with the test carpet show that RPCs can operate with high efficiency ($\sim$ 95%) and with the already mentioned 1 ns time resolution. Moreover the trigger rates and distributions of events agree with the expected behaviour as obtained by dedicated Monte Carlo simulations making us confident about the reliability of the simulations. In particular the expected effect of the lead converter is confirmed as summarized by the two plots shown in Fig.2.5. The event rates taken with and without the converter are shown in the left plot. The direction of recorded events was reconstructed by means of a simple planar fit and the "chess-board" method

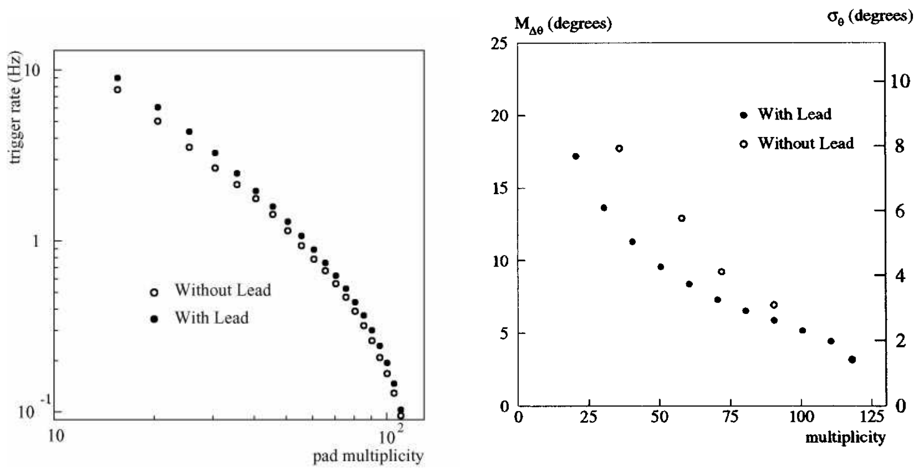

Figure 2.5: *Results of the measurements of the 1998 test experiment with a* $\sim 50\,m^2$ *carpet. Left plot shows the integral rate as a function of the event multiplicity as measured with and without a 0.5 cm lead converter. On the left the median value* $M_{\Delta\theta}$ *of the distribution of odd-even angle difference is plotted versus multiplicity.*

allowed to estimate the angular resolution which has been found to improve with the use of the converter (right plot). Another relevant measurement of the test was the counting rate per PAD on which the noise estimate (presently used in the detector response simulation) is based.

To date 36 Clusters ($\sim 1600\ m^2$) have been installed and partially put in operation for calibration runs [44] and for the tests of the integrated operation of RPCs, DAQ, trigger, etc.

Fig.2.6 shows an example of a real event detected with 4×4 Clusters in which the shower front can be easily recognized. This space time image can be considered as a small scale version of the events that the full carpet will be able to detect.

The operation of 80 Clusters is scheduled for 2004. As a first step, stable data taking will be performed with 36 Clusters, i.e. an area large enough for studying Solar Flares and for GRBs detection with the method of single PADs rate.

The other physical purposes, in particular the study of γ-ray sources, require a much larger area. They will become viable in 2005 when the detector will

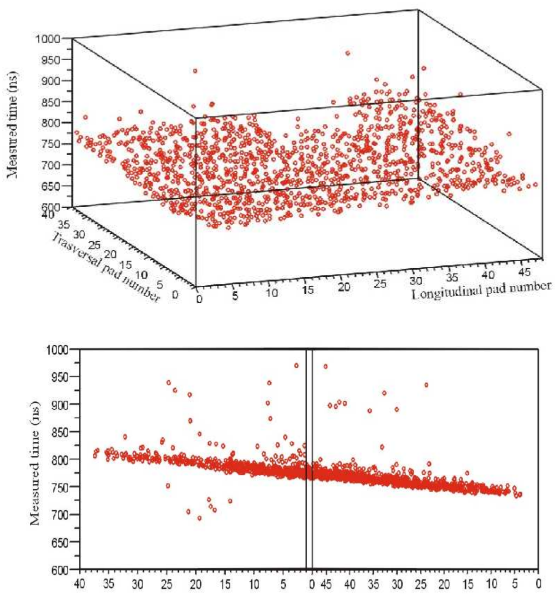

Figure 2.6: *Space-time image of an air shower front as detected by a small portion (16 Clusters) of the ARGO–YBJ detector. In the second figure, the plot has been rotated to make the front visible.*

be completed and fully operating.

2.2 Data analysis.

The ARGO–YBJ experiment uses a detection technique that makes it similar for many aspects to the traditional EAS arrays. However important differences hold.
Firstly, the lower energy threshold implies that ARGO–YBJ has to deal with showers with smaller size, and, in turn, with a higher level of intrinsic fluctuations (see for example Fig.2.7). Furthermore, the expected trigger rate is of the order of some ten kHz (27 kHz for a trigger with $M_{trig} = 10$ [45]) because of the combined effect of the wide aperture and of the falling power law spectrum of the background, whose integral dramatically increases when moving to lower energies. On the other hand, having a high space–time granularity, ARGO–YBJ will allow for an unprecedented image analysis of the shower front. The examples of Fig.2.7 and Fig.2.8 show in particular that relevant differences can be observed between the images of signal γ events and the more numerous hadronically initiated EAS. The former are compact and symmetric around the core position whereas protons exhibit a less regular image. This simple observation opens new perspectives in the possibility of rejecting background, an ability that has been primarily responsible for the success experienced by IACTs.

Because of these distinctive features it is far from being obvious that the traditionally used reconstruction techniques are the optimal choice for the ARGO–YBJ data analysis.

New reconstruction algorithms should be studied in order to fully use the detector capabilities. The ideal reconstruction algorithms for the ARGO–YBJ data analysis have to be:

- fast
- capable to efficiently recover shower to shower fluctuations
- able to extract the whole physical information provided by the shower front imaging

Problems of huge rates and fluctuations could be faced by setting a very high multiplicity threshold in the trigger logic. Such a choice, however, is equivalent to use ARGO–YBJ as a traditional EAS array with and high energy threshold and with a subsequent loss of the advantages related to its peculiar design.

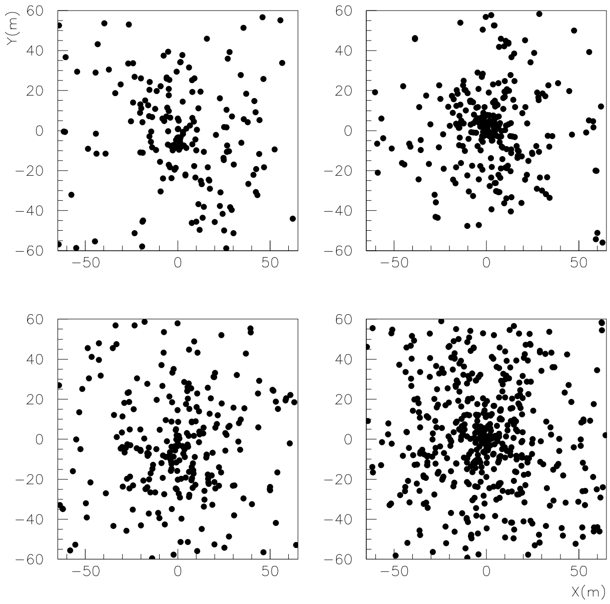

Figure 2.7: *Distribution of the detectable particles produced by 1 TeV γ at the YBJ altitude (MC simulations). The origin of the coordinate system is the shower core.*

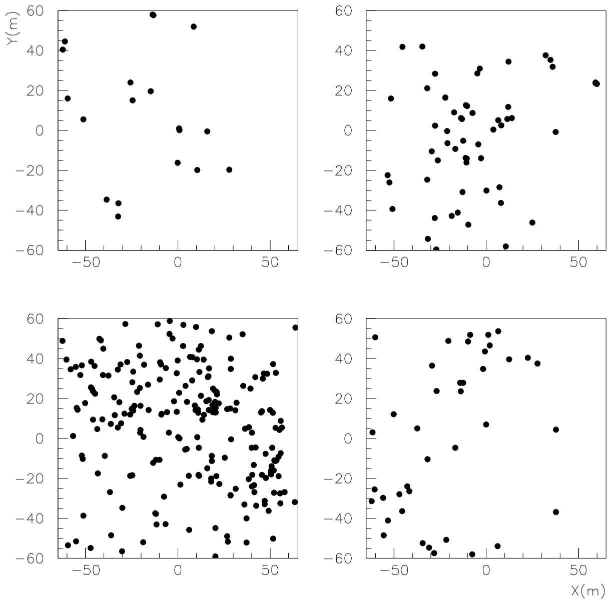

Figure 2.8: *Four examples of particle distribution for 1 TeV proton–induced showers.*

2.2.1 Event Reconstruction: Medea++

The ARGO–YBJ Collaboration has been developing a dedicated C++ code for the data analysis and reconstruction, called Medea++ [46].
Medea++ can be used to process both Monte Carlo simulations and DAQ data and can produce as output ROOT [47] or PAW [48] ntuples of reconstructed events to be used in subsequent higher level analysis (e.g. on-line monitoring, sky maps).
From a pure technical point of view the ARGO–YBJ data flow and data volume naturally lead to an Object Oriented framework as the environment for the physics analysis. C++ has been chosen for its flexibility and other advantages (polymorphism, inheritance, etc.) that greatly simplify the storage and management of huge amount of data and the maintenance of software codes and libraries composed by many source lines.

The event reconstruction implemented so far (Medea++ v.3.0) consists schematically of the following steps:

1. Software noise filter
2. Core reconstruction
3. Direction reconstruction

The noise filter simply selects within the 2μs event window a subwindow (default 400 ns) whose multiplicity is maximal. This allows to further reject noise hits.

A number of different algorithms have been implemented for the core and direction reconstruction. They will be discussed in Ch.4 and Ch.5, while no energy reconstruction has been yet implemented.

In addition to the listed reconstruction items, background rejection techniques based on image analysis and on the use of neural networks are under development, together with studies about the applicability of a more traditional approach based on the use of muon detectors to be added to the experimental apparatus. Both the methods look very promising, but will not be considered here. Preliminary results can be found in [49].

From the physical point of view the major question about the event reconstruction is how to compare the algorithms and how to choose the best one. The obvious answer is that a choice has to be ultimately made on the basis of the physics goals that can be met. Therefore, the effects of event reconstruction on the experimental sensitivity for the detection of γ–ray sources have to be studied.

2.2.2 Sensitivity to point–like sources.

In Ch.1 a very broad definition of the sensitivity S has been given for ground–based detectors as the ratio of the signal to the background fluctuations. In order to write S in a more explicit form, the detection efficiency for a single shower and the method used to search for a source have to be specified.

Effective area

The detector collection efficiency is conventionally represented through the effective area A_{eff} defined as the area of an ideal detector (equivalent to the real one), normal to the incident direction of the primary particle, having efficiency 1 if the shower core falls within its area and 0 outside.
The effective area can be determined by simulating N_{gen} showers with their core position distributed over a very large area A_{gen}. If N_{rec} events survive the trigger condition and the reconstruction cuts:

$$A_{eff} = \frac{N_{rec}}{N_{gen}} \times A_{gen} \tag{2.1}$$

A_{eff} treats as a whole the detector and the atmosphere including also the effects of atmospheric absorption.
The effective area in the case of ARGO–YBJ is a function of the type, energy, and incident direction (zenith angle θ) of the primary particle.
Moreover, since ARGO–YBJ lies on a horizontal plane the effective area have to be multiplied by a factor $\cos\theta$ to reflect the reduction of area normal to the incident direction.

Binned analysis

Consider the case of a point source F with equatorial coordinates δ (declination) and α (right ascension).
While all the events detected from the source come from (δ, α) their reconstructed directions are distributed around the true source position because of the finite angular resolution of the detector. As in the analysis of other ground–based observatories, an angular bin $\Delta\Omega$ is opened, centred on the source position. Its optimal size must be determined to retain as little of the background as possible while keeping the largest fraction $\xi(\Delta\Omega)$ of signal events associated with the source. In the case of a round bin: $\Delta\Omega = 2\pi(1 - \cos\psi_b)$ where ψ_b is the optimal half-opening of the bin and depends on the angular resolution.

Field of view and exposure of a source.

Due to the degradation of the detector performances with increasing zenith angle, the field of view (FOV) of EAS arrays is artificially reduced by retaining only the events reconstructed with $\theta < \theta_{FOV}$, where θ_{FOV} is generally set to $\sim 40° - 45°$.
A source F follows a daily path Γ_F in the local sky. In particular its local zenith varies with time according to a function $\theta(t)$ that depends on the source declination. Therefore, events from the source can be detected when $\theta(t) < \theta_{FOV}$ only, i.e. in a time window $T(\delta)$ during a day of data taking. Moreover the observational conditions vary during the day depending on the source position in the local sky.

Sensitivity

From an observational point of view showers can be directly classified on the basis of their multiplicity only, so that as a first step any result, including the sensitivity, should be expressed as a function of the number of fired PADs.

Using the notation introduced before, the detection significance in a multiplicity range ΔN_{hit} can be written as:

$$S(\Delta N_{hit}) = \frac{t \int_{T(\delta)} dt' \int_{\Delta E_\gamma} dE\, A^{\gamma}_{eff}(E, \theta(t')) \cos\theta(t') \cdot \Phi_F(E) \cdot \xi(\Delta\Omega)}{\sqrt{t \sum_k \int_{T(\delta)} dt' \int_{\Delta E_k} dE\, A^{k}_{eff}(E, \theta(t')) \cos\theta(t') \cdot \Phi_k(E) \cdot \Delta\Omega}} Q \tag{2.2}$$

where Φ_F is he differential flux of the source, Φ_k is the differential flux per steradian of the k-th type of background particle (proton, Helium nucleus, etc.), A_{eff} is the effective area for the particle indicated by the superscript, t is the effective time of data taking expressed in days, Q is a quality factor for γ/hadron separation that here will be considered fixed at 1 (no background rejection). Even if not explicitly written, the effective areas and the opening bin depend on ΔN_{hit}.
The energy integrals are computed over the whole energy range that give contribution in the multiplicity range of interest[3].

[3]The energy range depends on the type of the primary particle. In particular since a significant part of the energy of a primary hadron goes in muons, the induced shower has a smaller size with respect to that produced by a γ-ray of the same energy. Therefore,

Neglecting Q, the reconstruction dependent quantities are the effective areas and the angular bin. Eq.2.2 shows that they cannot be isolated from the source dependent factors (flux and position). In other words, it is not possible to find a reconstruction strategy that is optimal for every kind of source.

Nevertheless, a criterion is needed to compare the event reconstruction algorithms, therefore the optimal analysis will be defined here as the reconstruction chain that maximises the sensitivity to the Crab Nebula.

The choice of Crab Nebula relies on the following reasons:

- this source is the standard candle of VHE sky and its detection will be the first goal of the ARGO–YBJ experiment
- its spectral index has an intermediate value among the known sources
- at the YBJ site it culminates at $\theta = 8^\circ$ being at an intermediate position in the ARGO–YBJ visible sky

The latter two points should guarantee that the reconstruction strategy optimized for the Crab detection is a reasonable choice (even if not the optimal) for a generic source that can be observed by ARGO–YBJ. In particular it can be applied to map the overhead sky when searching for unknown sources.

In the following chapters the estimate of the ARGO–YBJ sensitivity to the Crab Nebula will be the guideline.
To perform this estimate a large amount of Monte Carlo simulated showers have been generated as explained in Ch.3.

---

for a fixed multiplicity range the background contribution come from higher energies than the signal ones.

Chapter 3

Monte Carlo simulations.

In order to obtain a reasonable estimate of the detector performances, a large number of Monte Carlo (MC) simulations is needed. They must reproduce the actual distribution of triggering showers with enough statistics.

The image of a shower as detected by the ARGO–YBJ detector depends on a number of parameters: the energy E of the primary particle, the local zenith (θ) and azimuth (ϕ) angles and the position of the shower core on the detector plane ($A = (x, y)$). Even for a given set of parameters, enough statistics is needed to take into account shower to shower fluctuations.

This chapter describes in full details how the MC showers have been generated. A system of weights has been used to get the rate of triggering events both from a gamma source and from the isotropic cosmic-ray background.

These simulations will be used in the next chapters to test reconstruction algorithms and to compute the detector sensitivity to point like sources.

3.1 Extensive air showers and detector simulation.

Simulating the ARGO–YBJ response is a two step process. First the EAS development is simulated by using the software package CORSIKA [50]. In the second stage all the secondary particles reaching the ground at the altitude of ARGO–YBJ are propagated through a detector simulation called ARGOG (based on the GEANT package).

3.1.1 CORSIKA simulations

CORSIKA (COsmic Ray SImulations for KAscade) is a MC simulation program designed to study the development of EAS in the Earth's atmosphere induced by primary particles with energies up to 10^{20} eV. Versions 6.004 and 6.014 [51] have been used.

The simulation of an EAS starts with the first interaction of the primary particle in the upper atmosphere, then tracks the subsequent interactions of secondary particles, eventually propagating the resulting EAS up to the observation level (i.e. the ARGO–YBJ altitude: 4300 m).

Within CORSIKA, electromagnetic interactions are simulated using EGS4 code [52]. QGSJET [53] is used to treat hadron-nucleus and nucleus-nucleus interactions at energies > 80GeV, whereas GEISHA [54] is used in the low energy range. Other settings are shown in Tab.3.1

Magnetic field	Threshold Energies
$B_X = 34.5\ \mu$T	$E_h = 0.05$ GeV
$B_Z = 35.0\ \mu$T	$E_\mu = 0.05$ GeV
	$E_{\gamma/e^\pm} = 0.001$ GeV

Table 3.1: *Magnetic field at the ARGO–YBJ site (with respect to the CORSIKA coordinate system) and threshold energies used in CORSIKA simulations.*

Showers initiated by gamma, protons and He nuclei were generated in the zenith ranges $0° - 15°$ and $15° - 30°$ *"in a manner which represent equal particle fluxes from all solid angle elements of the sky and a registration by a horizontal detector arrangement"* [51]. This means that the distribution of generated showers is uniform in the azimuth angle while the dependence on the zenith θ is $\propto \cos\theta \cdot \sin\theta$. The $\cos\theta$ factor reflects the fact that the area actually seen by the shower is the projection of the horizontal area onto a plane orthogonal to the shower axis.

The maximum angle set to 30° is a choice: in the computation of sensitivity it is assumed that the source is followed only when it is above this maximum θ.

Since the differential power law energy spectra fall down rapidly both for gamma sources and CR background, a single generation over the whole energy range leads to poor statistics in the higher energy region. Therefore, the showers have been generated over energy sub-ranges $\sim$ equally spaced in $log_{10}(E)$ as shown in Tab.3.2. This choice actually moves the problem to a smaller scale; the obvious solution is to randomly extract energies from

Energy range (TeV)	γ	p	He
0.01-0.03	$\times$		
0.03-0.1	$\times$	$\times$	
0.1-0.3	$\times$	$\times$	$\top$
0.3-1	$\times$	$\times$	$\top$
1-3	$\times$	$\times$	$\times$
3-10	$\times$	$\times$	$\times$
10-30	$\times$	$\times$	$\times$
30-100		$\times$	$\times$

Table 3.2: *Energy ranges used in MC simulations for different primary particles. $\times$ = energy ranges actually used in the following chapters, $\top$ = ranges used only for tests (see Sec.3.4)*

a uniform distribution. To save computing time, an intermediate solution with a spectral index $\beta_g = 1$ has been used.

Note that for gamma-ray primaries the maximum generation energy is 30 TeV. This conservative choice should take into account a possible energy cut-off for gamma sources. In any case, if there is no cut-off, the number of signal showers and the actual sensitivity will be greater than estimated.

3.1.2 ARGOG: a simulation of the ARGO–YBJ detector.

The secondary particle reaching the ARGO–YBJ surface are propagated through the detector by ARGOG[1], a Monte Carlo program developed to fully simulate the ARGO–YBJ detector [56]. It is based on the GEANT3 (v3.21) CERN package [55]

ARGOG simulates the complete geometry of the detector including inter-chambers separation gaps, building columns, etc. The detector stratigraphy shown in Fig.2.2 is implemented and the detector is covered by a 0.5 cm thick layer of lead in order to convert a fraction of secondary gamma rays in charged particles and to reduce the time spread of the observed shower front.

The detector simulation applies a 1 ns smearing to the actual arrival time of a particle (given by CORSIKA). This simulates the time resolutions

[1]Last version used v1.3.4 Authors: D. Martello, A. Surdo, P. Bernardini, L. Perrone, C. Pino

of the RPCs.

ARGOG randomly distributes the core position of the CORSIKA showers on rectangular areas or rectangular frames whose dimensions can be selected by the user.

A simulation of random noise (400 Hz per PAD, as measured by the test carpet) is included, as well as a simulation of the trigger logic (see 2.1.4). The selected trigger multiplicity on the central carpet is $M_{trig} = 20$. The simulation of noise is performed only in coincidence with CORSIKA showers. Therefore, the pure noise events (i.e. random noise triggering events with no physical hit in coincidence) should be added. An upper limit to the expected rate of these events has been estimated by simulating 10^6 pure noise events in $2\mu s$ time windows: none of them satisfies the trigger conditions. Since the maximum number of 2μs windows that can be opened in 1 s is 5×10^5, the expected rate is ≤ 0.5 Hz. This simple test shows that pure noise events can be completely neglected if compared with the CR background rates; therefore they will be no longer considered in this thesis.

3.2 Cosmic rays spectra.

The trigger rates for γ-rays will be evaluated by using the Crab Nebula spectrum as derived by Hillas et al. [12] with a power-law fit of the Whipple telescope data:

$$\frac{dn}{dE} = 3.2\,10^{-7}\,E^{-2.49} \qquad (\gamma\,m^{-2}\,s^{-1}\,TeV^{-1}) \tag{3.1}$$

For CR background the spectra given in [57] will be used. The authors fitted the measured differential flux of protons and helium nuclei with the function:

$$\frac{dn}{d\mathcal{E}_k} = K \times \left(\mathcal{E}_k + b\,e^{-c\sqrt{\mathcal{E}_k}}\right)^{-\beta} \tag{3.2}$$

where $\mathcal{E}_k$ is the kinetic energy per nucleon (in GeV).

They use the BESS98 [58] and AMS [59] data sets[2] for protons. For helium BESS98, RICH [60], Sokol [61] and JACEE [62] data are used[3] Values of the fit parameters are given in Tab.3.3.

[2]These data refer to measurements in the energy region below 100 GeV. The extrapolation of fitted Eq.3.2 is in good agreement with other higher energy data.

[3]The fit to these data is called "high" fit. Another fit ("low") - obtained with BESS98 and AMS data - is steeper and affected by a 10% difference between the data sets.

Primary nucleus	β	K	b	c
Hydrogen	2.74$\pm$ 0.01	14900$\pm$600	2.15	0.21
Helium	2.64$\pm$ 0.03	600$\pm$30	1.25	0.14

Table 3.3: *Fit parameters for Eq.3.2*

The energy region that is relevant for the ARGO–YBJ experiment is above some 10 GeV. This allows to neglect both the particle mass and the second term in Eq.3.2. Therefore, the flux reduces to a simpler form $k\,E^{-\beta}$. Expressing the energies in TeV units and converting the energy per nucleon in energy per nucleus ($E = 4\mathcal{E}_k$ for helium nuclei), gives:

$$\begin{aligned} p: \quad & \frac{dn}{dE} = 8.98\,10^{-2}\,E^{-2.74} \qquad (p\,m^{-2}\,sr^{-1}\,s^{-1}\,TeV^{-1}) \\ He: \quad & \frac{dn}{dE} = 7.01\,10^{-2}\,E^{-2.64} \qquad (He\,m^{-2}\,sr^{-1}\,s^{-1}\,TeV^{-1}) \end{aligned} \tag{3.3}$$

Heavier nuclei ($Z > 2$) are expected to contribute less than 5% to the background flux and have been neglected.

Uncertainties in the values of the flux parameters will not be taken into account in this chapter and in the discussion of reconstruction algorithms. It is assumed that small variations in the spectral indices do not affect the comparison of different reconstruction techniques. Where not specified, only statistical errors will be shown. Flux uncertainties will be discussed again only in Ch.6 when the actual value of the expected sensitivity will be computed.

3.3 Weighting the simulated events.

After generating events over different energy and zenith angle and with an energy spectrum flatter than the actual one, a system of weights is needed to get the triggering rates.

The problem can be stated in a completely general way as follows.
Suppose that we have a set of points randomly generated from a distribution function $f(x_1, x_2, ..., x_D)$ and that we need to estimate the integral of a different function of the same variables $h(x_1, x_2, .., x_D)$ over a subset $X^D \subset \mathbb{R}^D$. The differential number of generated events is distributed as :

$$dn_g = f\,dx_1 dx_2 ... dx_n \tag{3.4}$$

while we need to integrate:

$$dn = h\, dx_1 dx_2 ... dx_n \tag{3.5}$$

Multiplying each generated event by the weight

$$w(x_1, x_2, ... x_D) = \frac{h}{f} \tag{3.6}$$

gives $dn_g \cdot w = dn$.

The total number N of generated events in X^D gives the MC estimate of $\int_{X^D} f d^D x$, whereas the sum of weights is the estimate of the desired integral $\int_{X^D} h d^D x$. The statistical error is $\sqrt{\sum_{i=1}^{N}\ w_i}$.

Returning to the atmospheric showers, suppose now that we have n_g events generated over a continuous range $\phi \in [0, 2\pi]$, $\theta \in \Delta\theta = [\theta_1, \theta_2]$ and $E \in \Delta E = [E_1, E_2]$ (slope $\beta_g = 1$) and with the core position uniformly distributed over an area A_g. The distribution of generated showers is, in this case:

$$dn_g = \lambda \cdot E^{-1} \sin\theta\ \cos\theta\, dE\, d\theta\, d\phi\, dA \tag{3.7}$$

whereas the expected distribution of real showers from a diffuse flux (uniform in the solid angle) is:

$$dn = k \cdot E^{-\beta}\ \sin\theta \cos\theta\, dE\, d\theta\, d\phi\, dA \tag{3.8}$$

What we are actually interested in is the number of observed events dn^{obs} rather than dn, where:

$$dn^{obs} = P_{det}(E, \theta, \phi, A) \cdot dn \tag{3.9}$$

and $P_{det}(E, \theta, \phi, A)$ is the trigger probability for a shower initiated by a primary particle of energy E, zenith θ, azimuth ϕ and core landing coordinates $A = (x, y)$ (of course, P_{det} depends also on the nature of the primary particle).

The number of generated showers that survives the trigger conditions is $dn_g^{obs} = P_{det}(E, \theta, \phi, A) \cdot dn_g$. Therefore, the expected number n^{obs} of triggering events can be estimated as the weighted sum of generated triggering events with weights:

$$w_R = \frac{k}{\lambda} E^{1-\beta} \tag{3.10}$$

The constant λ can be easily computed by integrating both members of Eq.3.7

$$\begin{aligned} n_g = \int dn_g &= \lambda \int_{\Delta E} E^{-1} \int_{A_g} dA \int_{2\pi} d\phi \int_{\Delta\theta} \sin\theta \, \cos\theta \, d\theta \\ &= \lambda \cdot ln\left(\frac{E_2}{E_1}\right) \cdot A_g \frac{\pi}{2}(\cos 2\theta_1 \, - \, \cos 2\theta_2) \end{aligned}$$

this implies that

$$\frac{1}{\lambda} = \left(\frac{A_g}{n_g}\right) ln\left(\frac{E_2}{E_1}\right) \frac{\pi}{2}(\cos 2\theta_1 \, - \, \cos 2\theta_2) \tag{3.11}$$

Substituting in in Eq.3.10 gives the explicit expression for w_R.

In this notation the effective area is:

$$A_{eff}(E,\theta,\phi) = \int_{\infty} P_{det}(E,\theta,\phi,A)\, dA \tag{3.12}$$

3.3.1 An example application: rate of internal protons

As an example, the method of weighting events has been used to get the rate of internal protons (i.e. with the core position (x,y) within the boundaries of the ARGO-YBJ central carpet). Results are shown in Fig. 3.1 (points) together with the corresponding flux of protons on the top of the atmosphere (dotted lines). The ratio between the number of triggering events and the incident flux is the trigger efficiency integrated over the corresponding solid angle. At energies of some TeV the efficiency is $\simeq$ 1.

3.4 Choice of generation areas and relevant energy ranges.

Because air showers may have lateral extent of 300 m or more, they may trigger the detector even if their core position is very far from the detector. That is why the effective area can be much larger than the geometrical area of the detector and why an integration over an infinite area is needed in Eq.3.12. Of course, the trigger probability P_{det} decreases with the distance of the core position from the detector centre with a rate that depends mainly on the nature and energy of the primary particles. This suggests that for each energy and zenith angle range a generation area A_g can be found such that:

$$\int_{A_g} P_{det}(A)dA \simeq \int_{\infty} P_{det}(A)dA = A_{eff} \tag{3.13}$$

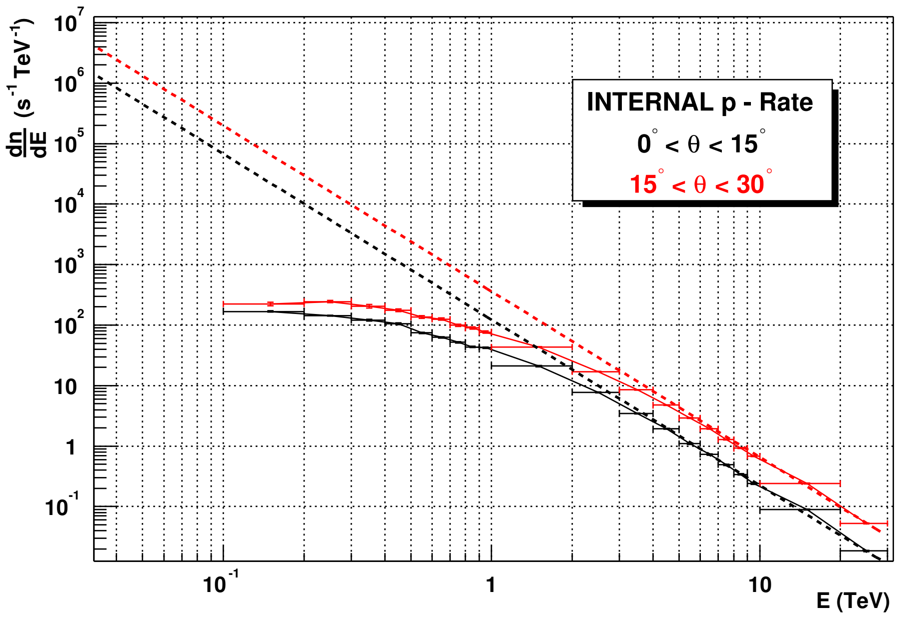

Figure 3.1: *Differential flux of internal protons in two wide ranges of solid angle. Points refer to the expected rate of triggering events (MC simulations). Dotted lines represent the corresponding flux of events on the top of the atmosphere.*

where A_{eff} and P_{det} denote the average values over $\Delta\theta$, ΔE and $\Delta\phi = 2\pi$. Generating showers on larger areas is a waste of time since they do not contribute to the trigger rate. On the other side, generating over an area not sufficiently large leads to underestimations of the effective area and, in turn, of the expected rates. In order to evaluate the minimum generation area that allows to reliably estimate A_{eff}, a preliminary study has been done.

Showers induced by γ-rays, protons and helium have been generated with the core position distributed along the detector x axis (on the thin grey rectangle in Fig.3.2) up to very large distances. It has been assumed that at each point on the sides of a square, centred at the detector centre, (black square in Fig.) $P_{det}(x, y)$ is exactly the same as at the intersection point to the x axis $B(x) = (x, 0)$ (i.e. $P_{det}(x, y) \simeq P_{det}(x, 0)$). With this

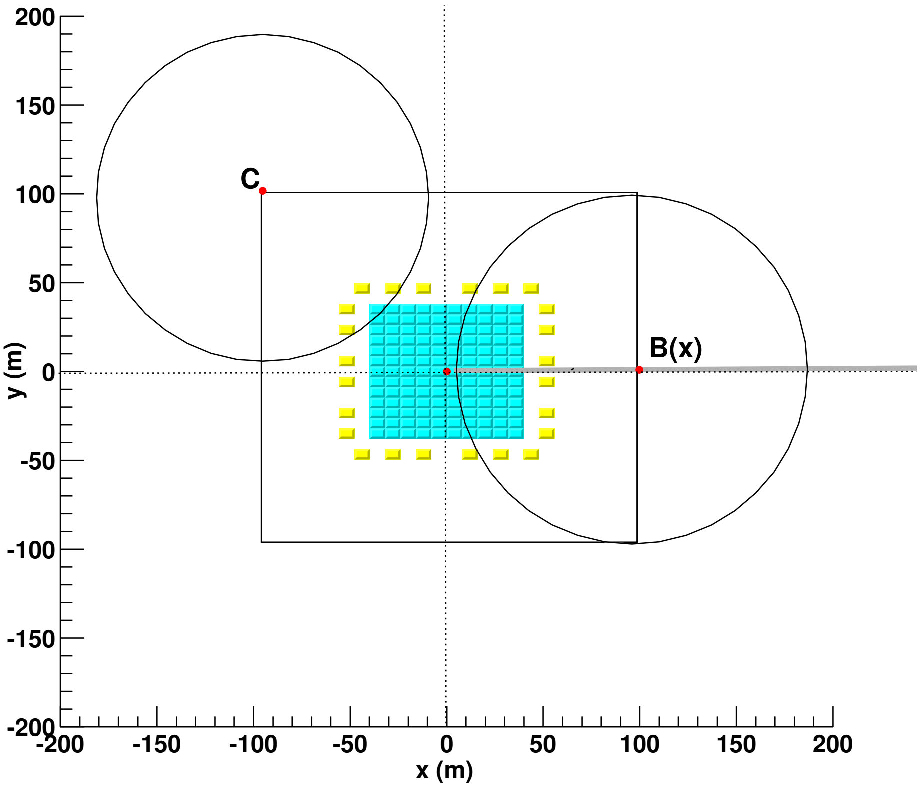

Figure 3.2: *Showers for the tests described in this section have been generated with their core position uniformly distributed over the thin grey rectangle along the positive x axis. In order to estimate the expected rates it has been assumed that at each point on the side of the black square (side = $2x$) the trigger probability is the same as in B(x).*

assumption the integral of P_{det} over $A_g = 2d \cdot 2d$ can be estimated as:

$$\int_{-d}^{d}\int_{-d}^{d} P_{det}(x,y)dx\,dy \;\simeq\; \int_{0}^{d} P_{det}(x,0)\cdot 8x\,dx \qquad (3.14)$$

This integral is expected to increase with d up to an asymptotic value that is the desired effective area.

The equal probability assumption actually overestimates the minimum area. In fact, Fig.3.2 shows that if a shower is roughly described as a disk centred at its core position, its intersection with the detector active area is smaller when its core is in the corner C rather than in the middle of the square side (point B). Since our main problem is not to underestimate the generation area, the approximation that has been used is good.

Another problem is to have an idea of the relative contributions of different energies to the trigger rate. To do this, rather than computing the integral in Eq.3.14, the quantity $P_{det}(x,0)\cdot\cos\theta\cdot k\,E^{-\beta}$ has been integrated (i.e. P_{det} has been multiplied by the source flux and the geometrical factor $\cos\theta$, then integrated in the variables E, θ and x). This does not alter the behaviour of the integral as a function of d and gives as asymptotic value a rough estimate of the trigger rates.

In Fig.3.3 results obtained for the uniform flux of protons and helium in the zenith range $0° < \theta < 15°$ are shown. As expected, an asymptotic value is approached at a distance that is larger for higher energy primaries[4]. This reflects the fact that the average lateral extent of an air shower increases with energy.
Since the total background rate in $0° < \theta < 15°$ is ∼600 Hz, the contribution of helium with $E < 1$ TeV is negligible and will not be added to the simulations.

An analogous plot for γ-rays is shown in Fig. 3.4. A fictitious diffuse flux with a number of γ in the unit solid angle equal to the Crab Nebula flux has been used. Note that the plateau is reached at distances much smaller than in the hadronic shower case.

[4]It is interesting to notice an anomalous behaviour of protons in the lower energy range 30 GeV - 100 GeV (red points); it has been checked that the images of triggering showers on the detector central carpet look like those of low energy internal γ-rays even if their core position is more than 100 m far from the detector centre and that it is not due to the magnetic field. This class of background events will be very confusing for the reconstruction algorithms A dedicated study should be performed to trace the physical source of this behaviour.

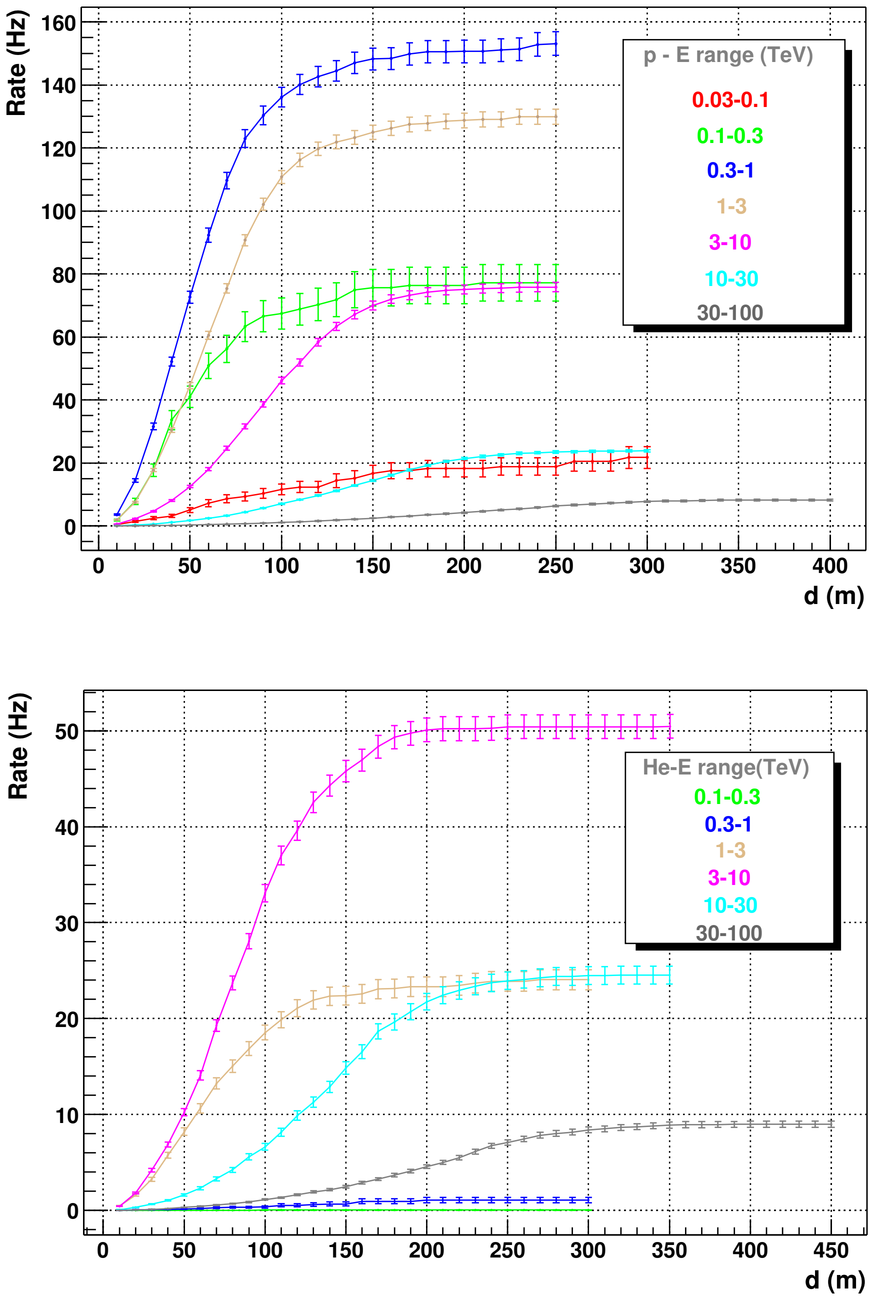

Figure 3.3: *Estimated protons and helium rates for* $0° < \theta < 15°$ *as a function of the maximum distance from the detector centre. Each point represents the estimated rate obtained when generating showers with their core position uniformly distributed over an area* $A_g = 4 \cdot d^2$.

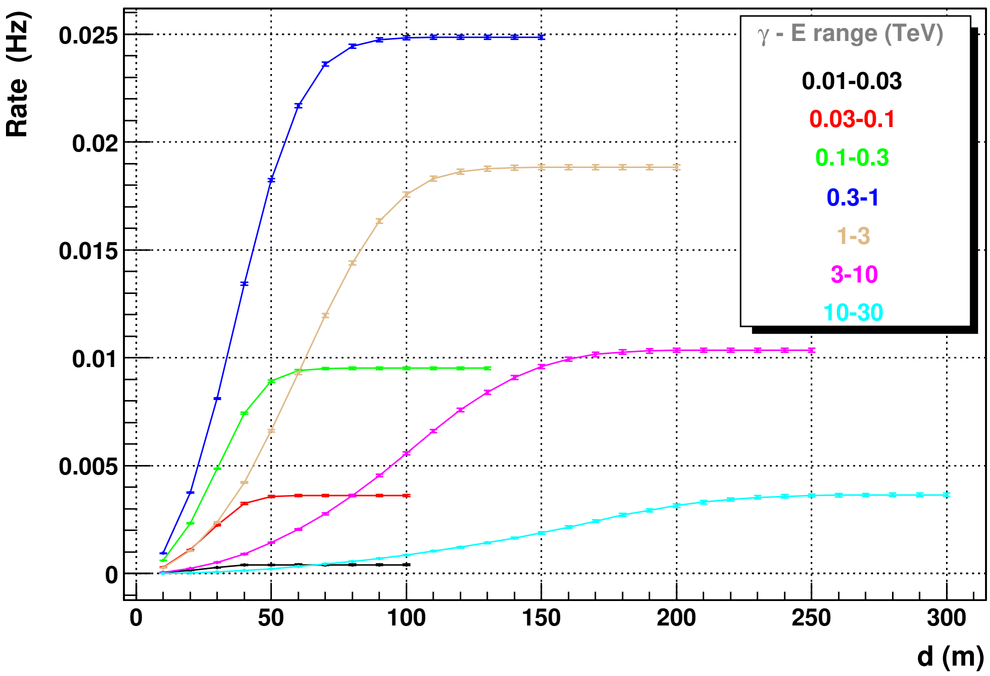

Figure 3.4: *Estimated rates for* $0° < \theta < 15°$ *from a Crab-like diffuse flux of* γ*-rays. As in Fig.3.3, points represent the rates corresponding to a generation area* $A_g = 4 \cdot d^2$.

The three plots allow to compare the rate of internal showers (whose estimate is given by the points at d=40 m) with the total rate. It can be seen that the ARGO-YBJ trigger rate will be in the majority from external showers, both for photons and hadrons.

The criterion for choosing generation areas for the simulations used in the sensitivity calculation is to set a value of d such that the corresponding rate differs less than 5% from the plateau one. The selected generation area is a square whose side is $L_{max}(\Delta E) = 2d$. The values of L_{max} are listed in App. A.

For a fixed energy of the primary particle and a given core position, the trigger probability decreases with the zenith angle because of the thicker layer of atmosphere traversed. This suggests that the asymptotic value of the rate is reached at slightly smaller distances. Therefore if relation 3.13 holds for a given value of θ, it will hold for higher zenith angles; the same areas selected in the zenith range $0° < \theta < 15°$ have been used also for $15° < \theta < 30°$.

The reconstruction capabilities of the detector are expected to depend on the radial distance of the core from the detector centre rather than on its actual position, therefore a sufficient number of showers has to be generated

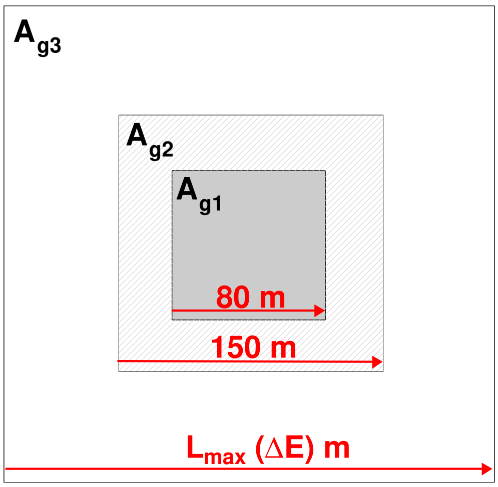

Figure 3.5: *The generation area has been divided in three subareas. In each subarea the core position has been uniformly thrown. The generation density gradually decreases from* A_{g1} *to* A_{g3}

at each distance. This goal cannot be achieved with a uniform generation of cores over $A_g = L^2_{max}$. In order to have suitable statistics for internal showers, the generation area has been divided in three subareas as shown in Fig.3.5. The internal square A_{g1} roughly corresponds to the area of the full-coverage carpet, A_{g2} is a frame around the sampling ring, A_{g3} is the remaining part of L^2_{max} . The same number of showers has been simulated in each area (i.e. $n_g(A_{g1}) = n_g(A_{g2}) = n_g(A_{g3}) = n_g$). This choice implies that the density of simulated showers is higher in the internal areas as desired.

A total of more than 70 million showers has been simulated. The complete tables of generated showers can be found in App.A.

3.5 Trigger rates.

The first result that can be obtained by using the MC simulated showers is the evaluation of the expected trigger rates up to 30° zenith angle.

Fig.3.6 shows the rate of triggering background events as a function of the energy of the primary particle. Contributions from protons and helium are plotted separately. Once again it can be seen that external showers give the main contribution to the trigger rate.

Since the signal from γ-rays is orders of magnitude smaller than the background, the rate of events to be analysed is given by the number of observed background showers. The expected rates up to $\theta = 30°$ are listed in Tab.3.4

Primary nucleus	expected rate (Hz)
p	1126 ± 8
He	339 ± 4
Total (p+He)	1465 ± 9

Table 3.4: *Rate of triggering events from the uniform CR background up to 30° with statistical errors.*

For γ-rays the rate expected from the Crab Nebula has been computed by averaging the source position (θ, ϕ) over the whole solid angle (Fig. 3.7). It is expressed in TeV^{-1} sr^{-1} because it has been obtained from the rate of a fictitious diffuse flux divided by the solid angle. This rough estimate does not take into account the actual motion of the source. Nevertheless, it gives the order of magnitude of expected signal rate that is $\simeq 10^{-2}$ Hz on the average when the source is above 30°.

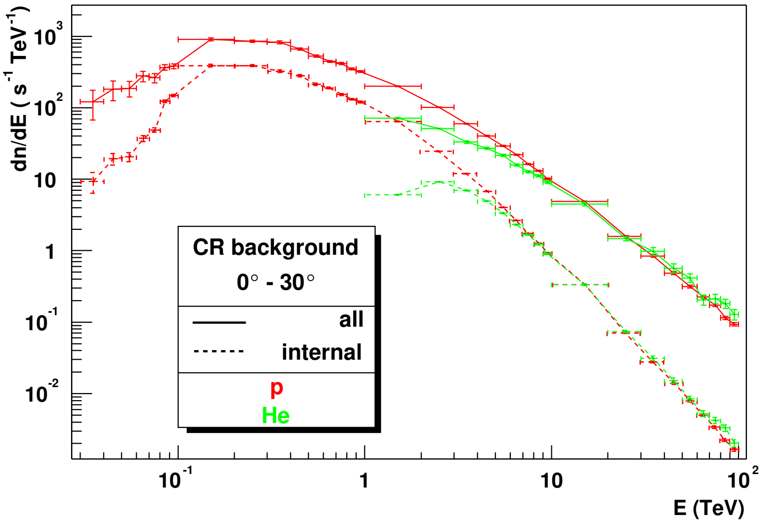

Figure 3.6: *Rate of triggering events from the uniform CR background as a function of the energy of the primary particle (protons in red, helium in green). Points with dashed error bars refer to internal showers, continuous lines to the total (internal+external).*

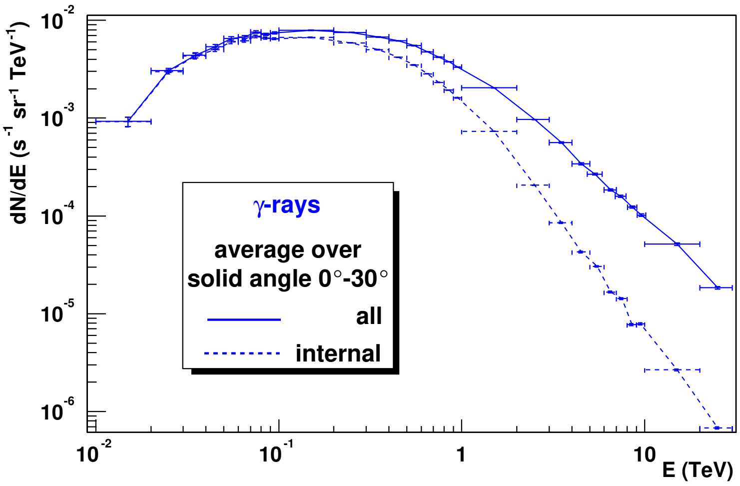

Figure 3.7: *Rate of triggering events from a Crab-like diffuse flux of γ-rays as a function of the energy. The dashed line refer to internal showers, the continuous one to the total (internal+external). This is the equivalent of the Crab flux averaged on the source position (θ, ϕ) over the whole solid angle with a uniform weight (instead of considering its actual motion).*

The contribution of external showers to the signal rate increases with energy up to more than 90%.

The distributions of triggering events in θ and ϕ are shown in Fig.3.8. As expected, no dependence on the azimuth angle can be seen. Therefore, the dependence of A_{eff}, P_{det}, etc. on ϕ will be disregarded in the following and substituted with an average over 2π.

The observed lowering of rates with increasing θ is due both to a reduction of effective area and to the geometrical factor $\cos\theta$.

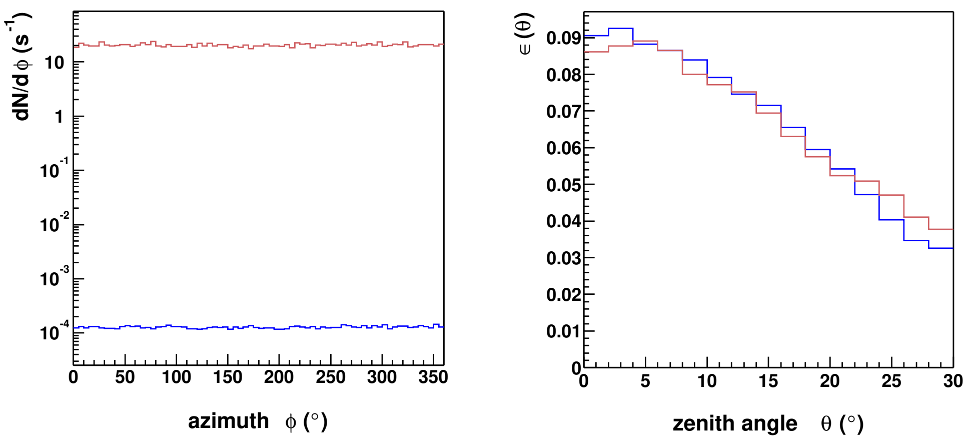

Figure 3.8: *Distributions in zenith and azimuth of the triggering showers from a diffuse flux for background p+He (red) and γ-rays (blue). The distributions in zenith (on the right) have been normalized to 1.*

3.6 Motion of the source.

The last step that is needed to reproduce the source rate is to consider its motion in the detector local coordinates.

Consider a point-like source S whose equatorial coordinates are (δ, α) (declination and right ascension). In Fig. 3.9 the source position is represented by the fixed vector $\mathbf{s}$. In the equatorial frame[5] the vector $\mathbf{a}$,

[5]In Fig. 3.9 the x axis does not point to the Vernal Equinox, it is rotated by an angle equal to the source right ascension. This choice does not affect, of course, the source zenith angle. Also the origin of time scale is shifted in such way that $t = 0$ when θ assumes its minimum value.

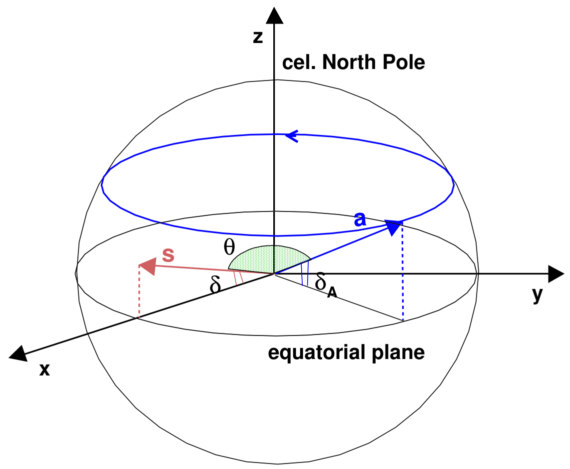

Figure 3.9: *In equatorial coordinates the source has a fixed position* **s**, *whereas the vector* **a** *(pointing to the zenith at the detector site) rotates with angular speed* $\omega = 15°/h$ *around the* z *axis due to the Earth's rotation. The zenith angle of the source is the angle* θ *between the two vectors,* δ *is the source declination,* δ_A *is the latitude of the detector site.*

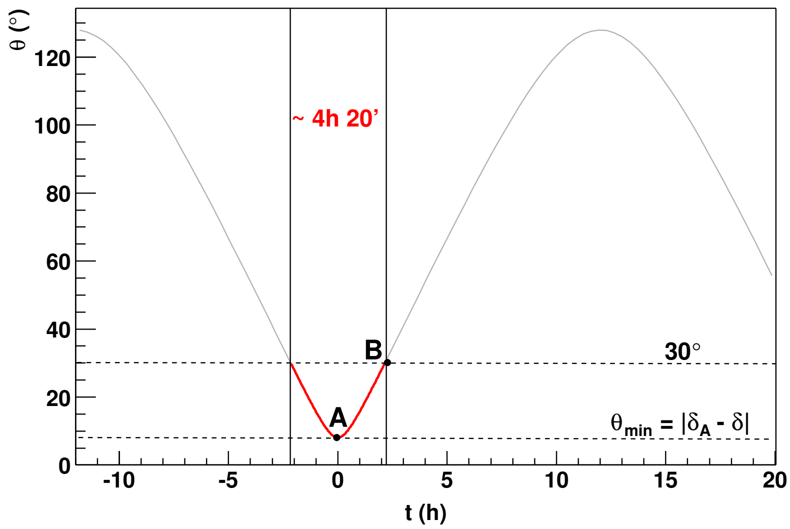

Figure 3.10: *Daily motion of the Crab Nebula. The local zenith at the Yang-Baijing site is plotted as a function of time. The red part of the curve corresponds to the observable motion (* $\theta < 30°$*).*

pointing to the zenith at the ARGO-YBJ site, forms a constant angle $\delta_A = 30^\circ\ 06'\ 38''$ (i.e. the YangBaijing latitude) with the equatorial plane and rotates around the z axis with the angular speed of Earth rotation $\omega \simeq 15^\circ/h$. Since it has been checked that the azimuth angle does not affect the detection probability, only $\theta(t)$ will be computed. The zenith angle of the source is given, at the time t, by:

$$\theta(t) = \arccos[\sin\delta_A\ \sin\delta\ + \cos\delta_A\ \sin\delta\ \cos(\omega t)] \tag{3.15}$$

The minimum zenith angle is $\theta_{min} = \theta(t=0) = |\delta_A - \delta|$. As an example Fig. 3.10 shows the motion of the Crab Nebula ($\delta = 22^\circ\ 00'\ 52''$).

Taking into account the source motion, the distribution of events to be reproduced is:

$$dn = k \cdot E^{-\beta}\ \cos\theta(t) dE\, dt \tag{3.16}$$

Note that considering only half of the daily motion of the source, the function $\theta(t)$ can be inverted (see for example in Fig. 3.10 the portion of the curve between the points A and B):

$$t(\theta) = C_1\ \arccos(C_2\ \cos\theta - C_3) \tag{3.17}$$

where $C_1 = 1/\omega$, $C_2 = 1/(\cos\delta_A\ \cos\delta)$ and $C_3 = tg\,\delta_A\, tg\,\delta$.

Therefore dt can be rewritten as:

$$dt = \frac{dt}{d\theta} d\theta \tag{3.18}$$

where:

$$\frac{dt}{d\theta} = \begin{cases} \frac{C_1\, C_2\ \sin\theta}{\sqrt{1-(C_2\ \cos\theta - C_3)^2}} & \text{if } \theta > \theta_{min}(\delta) \\ 0 & \text{if } \theta < \theta_{min}(\delta) \end{cases} \tag{3.19}$$

Comparing with the distribution of generated events (Eq.3.7), the proper weight can be easily obtained:

$$w_s = 2\,\frac{k}{\lambda}\,E^{1-\beta}\,\frac{1}{2\pi}\,\frac{1}{\sin\theta}\,\frac{dt}{d\theta} \tag{3.20}$$

where the factor 2 reflects the fact that $dt/d\theta$ has been computed only for half of the motion and that the motion is symmetric around $\theta = \theta_{min}$; $1/2\pi$ is needed to average over ϕ when summing the weigthed events. The physical meaning of w_s is that each θ contributes to the rate proportionally to the time spent by the source at that zenith angle.

The weighted sum of all the generated events gives the number of triggering events expected from the source in 1 day observation. It automatically takes into account the time during which the source is observable at $\theta < 30°$ (see, for example, Fig.3.11).

It should be noted that the distribution of simulated events is completely independent of the particular source. All the information about the source declination δ and its flux $k\,E^{-\beta}$ are contained in the weight w_s. This allows to reuse the same simulations to study a different source by only recomputing the weights.

When pointing to a source, the background is due to the CR showers reconstructed within the opening angle around the source position. Since the bin opened around the source is very small (an opening angle of 1° corresponds to $\simeq 10^{-3} sr$), it can be assumed that at each time t the density of background events is constant and equal to the value at the source position $\theta(t)$ (i.e. at the centre of the bin). Therefore, the source motion has to be considered also in the background estimate. This can be accomplished by weighting also the protons and helium showers with a weight similar to w_s in which the source spectrum is substituted by the background one and δ is again the source declination. This kind of background estimate will be used through the next chapters.

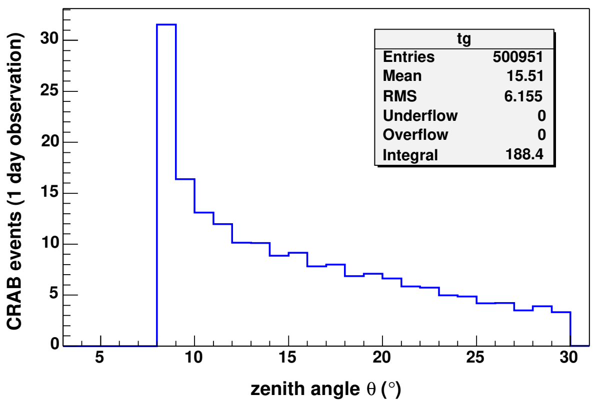

Figure 3.11: *Distribution of events expected from the Crab Nebula versus θ. The minimum zenith angle is $\theta_{min} \simeq 8°$.*

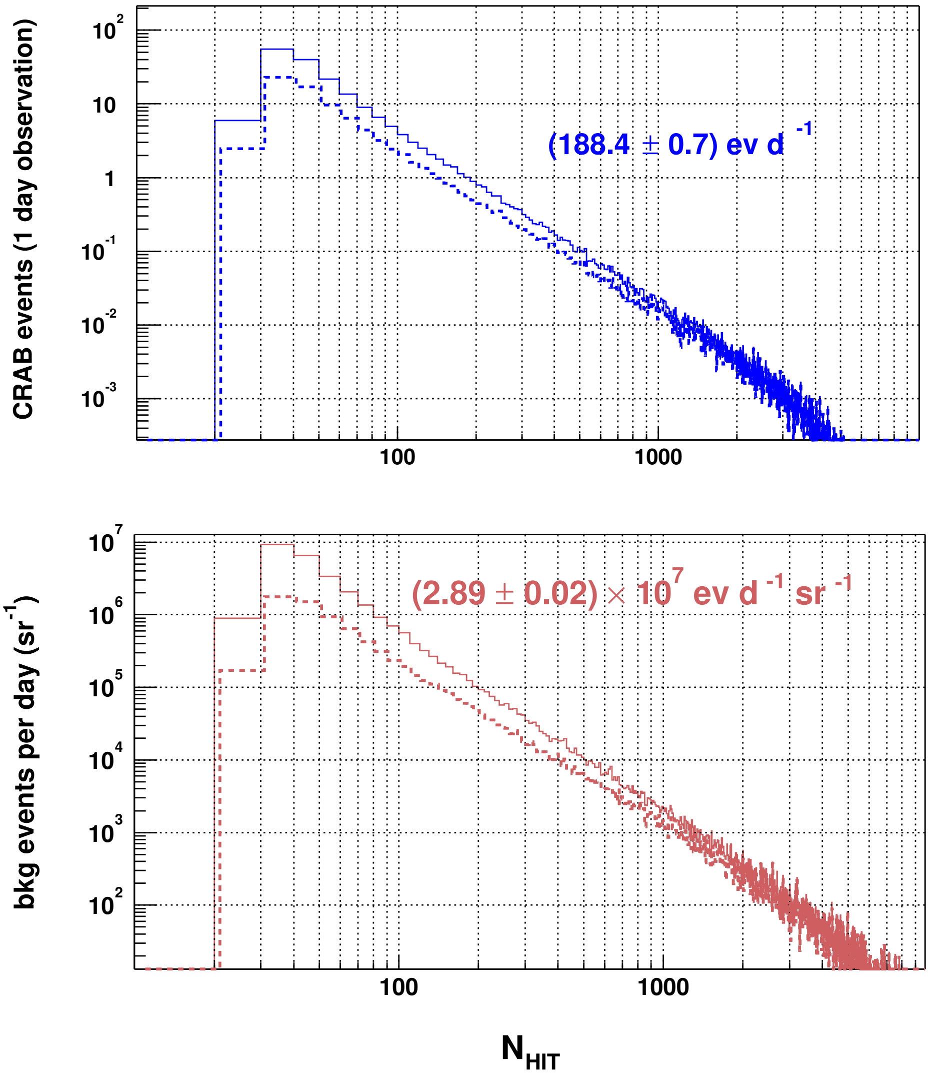

Figure 3.12: *Distributions of events as a function of the number of fired PADs. Continuous line refers to the total trigger rate (whose integrals are given with statistical errors), whereas results for internal showers are represented by the dashed histograms. The upper plot refers to the events from the Crab Nebula in 1 day observation time. The lower histograms shows the background per steradian expected in coincidence with the Crab motion.*

3.6.1 Crab Nebula.

The system of weighting events to consider the source spectrum and motion has been applied to the Crab Nebula.

In Fig.3.11 the distribution in zenith of the expected events surviving the trigger condition during 1 day data taking is shown.

Fig.3.12 shows the distribution of events as a function of the number of fired PADs (N_{hit}) on the ARGO-YBJ central carpet. The event multiplicity N_{hit} can be directly observed and does not depend at all on the analysis. For these reasons it will be used in the following chapters to classify events.

Multiplicity spectra clearly show that the external showers contribute mainly to the low multiplicity range (compare the difference between the continuous and dashed histograms).

The behaviour in the first bins is due to the trigger. As previously discussed, the trigger logic requires a minimum of 20 fired PADs satisfying precise space-time conditions. This is more stringent than a simple multiplicity cut (i.e. $N_{hit} > 20$) and reduces the population of multiplicity regions that are slightly above the trigger multiplicity threshold.

When discussing reconstruction algorithms, if not otherwise specified, the weighted events (with weight w_s) obtained for the Crab motion will be used and only statistical errors will be shown.

Chapter 4

Shower core reconstruction.

The first step in reconstructing an event is to determine where the shower core is located. Although the core position is not directly related to physical properties of the primary particle, it is used both in gamma/hadron separation and in the direction reconstruction algorithms.

The neural-network based methods for gamma/hadron separation will not be discussed in this thesis. Nevertheless, I would like to stress that they basically evaluate whether a shower image is radially symmetrical or not with respect to the shower axis, thus requiring an average error of about 3-5 meters in the reconstructed core position [49].

The accuracy in locating the EAS core will affect the angular resolution of ARGO-YBJ since the reconstructed core position is used as fixed vertex when fitting the shower front to a conical shape (see Ch. 5).

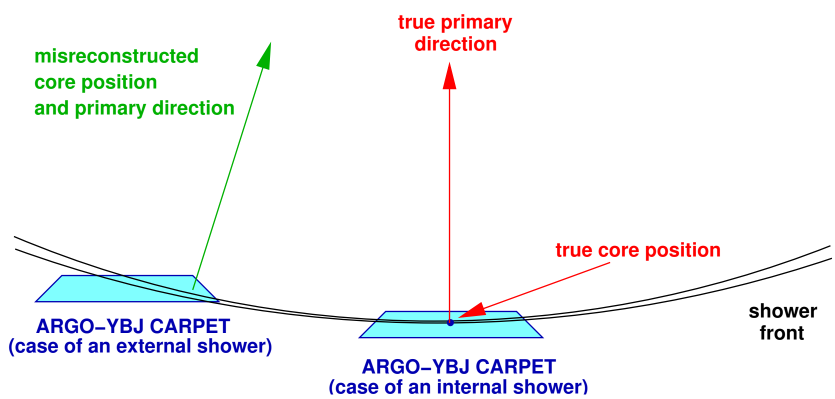

Figure 4.1: *In the case of external showers a degradation in both the core reconstruction and angular resolution is expected.*

Furthermore, since the recorded shower image is the intersection between the shower front and the detector active area, the ability to reconstruct an event depends on the true core position on the detector plane. In particular a degradation of the angular resolution has to be expected when dealing with showers whose core is off the ARGO–YBJ central carpet (external showers), as shown in Fig.4.1.
Moreover, simulations indicate that most of the triggering showers are external (~54% for γ primaries and ~73% for the isotropic cosmic-ray background), as discussed in Ch. 3. Therefore, another goal related to core reconstruction is to classify and eventually reject external showers in order to improve angular resolution.

Before describing the reconstruction algorithms, it is necessary to spend some words about the main limitations and problems that have to be faced when dealing with a single event:

- The problem is very involved when the dominance of fluctuations make the actual shower image very different from the expected average one. This is in particular the case of low multiplicity showers (i.e. showers with a low number of total fired PADs) and hadronic showers.

- In the case of external showers the overwhelming problem is that the recorded image is a relatively small portion of the shower that does not include the true core location. This intrinsic limitation adds to the problem of fluctuations. Without any knowledge about the energy of the primary particle it is quite difficult to distinguish a low energy internal shower from the long tail of an higher energy event with its true core position far from the detector central carpet (see for example Fig.4.2).

It can be noted that the reconstruction of background events does not affect the detector sensitivity. Results on hadronic showers could be of interest only in relation with external showers rejection (because it could help in reducing the amount of background). Therefore, the priority is to obtain a good core reconstruction for γ-induced showers.

As regards external showers, a good core reconstruction is unlikely to be achieved. The best result that can be expected is the reconstruction of their core position near the border of the detector active area. On the other hand, it can be guessed that an algorithm with poor performances for internal showers will be even worse for external ones.

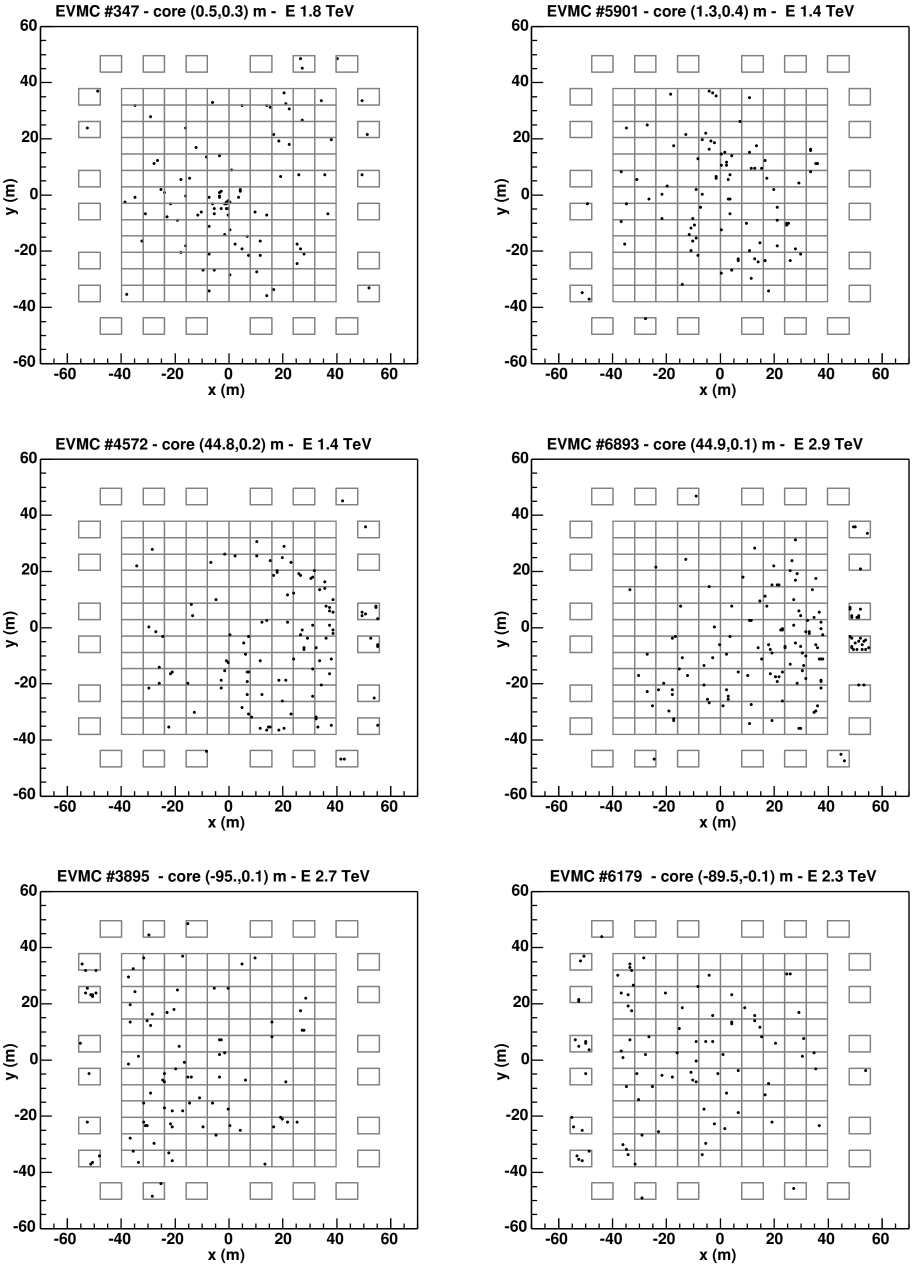

Figure 4.2: *MC simulated images of γ-induced showers on the ARGO–YBJ active area. Events with a multiplicity $N_{hit} \simeq 100$ have been selected. Their core is at the centre of the carpet (upper plots), outside the central carpet but within the ring (in the middle), more than 40 m far from the carpet (bottom).*

The previous simple considerations establish a logical order of priority that will be followed through the chapter. The first step (up to section 4.5) is to study the behaviour of the reconstruction algorithms on internal γ-induced showers. Results obtained for external showers and for background events will be shown as a second step.

4.1 Notation.

The following symbols will be used through the chapter:

$N \equiv$ pad multiplicity of a given event

Note that N differs from N_{hit}. The actual number of PADs used in reconstruction is N[1].

For the i-th fired PAD ($i = 1, \cdots, N$):

$x_i, y_i \equiv$ PAD centre coordinates on the detector plane

$t_i \equiv$ PAD time

$\mathbf{r_i}^{(\mathbf{2})} \equiv (x_i, y_i)$

$\mathbf{r_i}^{(\mathbf{3})} \equiv (x_i, y_i, z_i)$ (with $z_i = t_i \cdot c_{light}$)

$n_i \equiv$ number of fired strips

Symbols $x, y, \mathbf{r}^{(\mathbf{2})}$ without subscripts refer to a generic point on the detector surface, not necessarily coincident with the centre of a fired PAD. The subscript **rec** denotes the reconstructed core coordinates.

4.2 `Centre`: "centre of mass"

The simplest method to reconstruct the core position consists in calculating the average of the fired PADs coordinates weighted with the number of fired strips:

$$\mathbf{r_{rec}} = \frac{\sum_{i=1}^{N} \mathbf{r_i}^{(\mathbf{2})} n_i}{\sum_{i=1}^{N} n_i} \tag{4.1}$$

Fig.4.4 shows that `Centre` reconstructs the core position with an average error on internal showers that is larger than 8 m even for very high multiplic-

[1] As explained in Ch. 3, N_{hit} is the number of fired PADs on the central carpet within a 2 μs coincidence window and is used to classify the showers because of its complete independence on the event reconstruction. N includes also the PADs on the partially instrumented ring and is the sum over all the fired PADs that survive the software noise filter.

ities. This simple algorithm turns out to be inadequate to perform a good core reconstruction. More refined techniques are needed. However, since `Centre` is the most intuitive algorithm that can be thought to reconstruct the core position, it will be used in the following sections as a common term of comparison for the other methods that have been developed.

4.3 Tree algorithms.

Given a set of points $\{\mathbf{r_i}\}$, each one with an associated weight n_i, we call **r-tree** the set of lines joining a generic point $\mathbf{r}$ with each of the $\mathbf{r_i}$ (see Fig. 4.3). The centre of the tree ($\mathbf{r}$) can be either a point of the set itself or not. The definition can be easily extended to the three-dimensional case.
Now we can define the **r-tree length l(r)** as follows:

$$\mathbf{l}(\mathbf{r}) = \sum_{i=1}^{N} d(\mathbf{r}, \mathbf{r_i})\, n_i \tag{4.2}$$

where $\mathrm{d}(r, r_i)$ is the distance between $\mathbf{r}$ and $\mathbf{r_i}$.

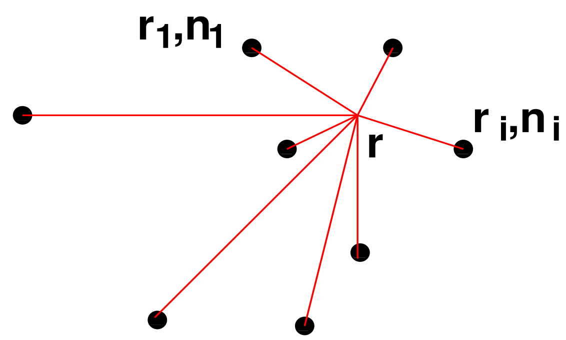

Figure 4.3: *An example of a 2-dimensional* $\mathbf{r}$*-tree.*

The image of the shower front as recorded by the ARGO–YBJ detector is a set of points (the space-time coordinates of the hits) with an associated weight (the number of fired strips). Therefore, the definition of tree given above can be directly applied.

The tree algorithms described in the following subsections are based on the construction of 3-dimensional[2] $\mathbf{r_i}$-trees (i.e. only points belonging to the given set of fired PADs have been considered as tree centres).

[2] A preliminary check has shown that including the time information (or third coordi-

When searching for the core position with the tree algorithms, the common underlying idea is that a point at the centre of a cluster has a smaller tree lenght with respect to an isolated point of the distribution.

4.3.1 `MTree`: searching for the minimal tree.

This algorithm calculates for each $\mathbf{r_i}$ the 3-dimensional tree length, then it finds the minimum value in the set $\{l(\mathbf{r_i})\}_{i=1,\dots,N}$. The reconstructed core position is given by the x and y coordinates of the hit $\mathbf{r_i}$ whose tree length is minimal.
The choice of using only the centre coordinates of fired PADs reduces the search to the computation of N tree lengths.

4.3.2 `Tree` and `DTree`: tree length based weighted average.

While `MTree` is, in some sense, a pure tree algorithm, `Tree` and `DTree` try to correct `Centre` by substituting the weight n_i with a tree length dependent weight $w_i(l_i)$:

$$\mathbf{r_{rec}} = \frac{\sum_{i=1}^{N} \mathbf{r_i}^{(\mathbf{2})}\, w_i(l_i)}{\sum_{i=1}^{N} w_i(l_i)} \tag{4.3}$$

where $l_i = l(\mathbf{r_i})$.
According to what has been said about the tree length interpretation, the weight must decrease when the tree length increases.
The difference between `Tree` and `DTree` is in the choice of the functional dependence of the weights on the tree length.
In the case of `Tree` the number of fired strip is divided by the corresponding tree length:

$$w_i = \frac{n_i}{l_i}. \tag{4.4}$$

`DTree` uses the following weight definition:

$$w_i = (1 - \frac{n_i\, l_i}{p_M}).$$

where $p_M = max\{n_i \cdot l(\mathbf{r_i})\}_{i=1,\dots,N}$.

nate z_i) improves the core reconstruction capability with respect to a simple 2-dimensional treatment.

4.3.3 Results.

Fig. 4.4 shows the average errors obtained when applying tree algorithms to γ showers with their cores internal to the central carpet. `DTree` algorithm performs a better reconstruction than `Centre` only in the multiplicity range $N_{hit} < 700$. In the case of the other two tree algorithms the error in core reconstruction is significantly smaller and with similar decrease with increasing PAD multiplicity. Only `MTree` will be discussed in the following sections since it gives better performances at every multiplicity.

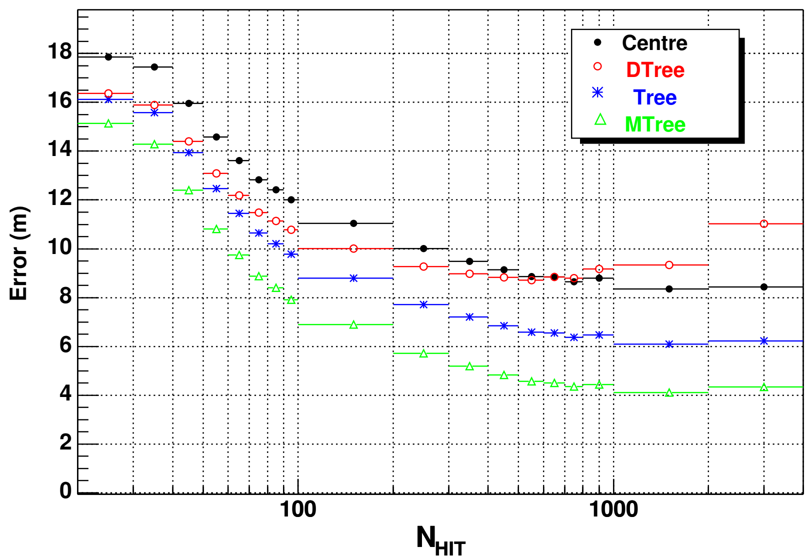

Figure 4.4: *Average distance between the reconstructed and the true core position versus multiplicity. Results obtained with the tree algorithms are shown in comparison with* `Centre`. *Only internal γ-induced showers have been analysed.*

4.4 Smoothing algorithms.

A simple idea to reduce local fluctuations in the hit distribution consists in deriving a smoothed distribution f, which is the convolution of the experimental 2-dimensional density with a properly chosen smoothing function g. The two methods described below calculate $f(\mathbf{r}')$ for each PAD centre $\mathbf{r}'$, whether the PAD is fired or not, then they find the absolute maximum of

f: the corresponding value $\mathbf{r}'$ is the reconstructed core position.

A subscript will be used to distinguish between the two algorithms: f_W for `Wavelets` and f_C for `Circle`.

4.4.1 `Wavelets`: searching for the maximum of the wavelet transform.

The function f_W calculated by this algorithm is the wavelet transform of the density distribution.
Given a generic function $\rho(\mathbf{r})$ with $\mathbf{r} = (x_1, x_2, \dots, x_D) \in \mathbb{R}^D$ its wavelet transform is defined as follows:

$$\tilde{\rho}(\mathbf{r}') = \int \rho(\mathbf{r}) \cdot g^{a,\mathbf{r}'}(\mathbf{r})\, d^3r \tag{4.5}$$

where $g^{a,\mathbf{r}'}(\mathbf{r}) = g(|\mathbf{r} - \mathbf{r}'|/a)$ and g is called mother wavelet.
Wavelets are widely used to analyse images and electronic signals by recognizing particular substructures whose shape depends on g while the scale can be selected by varying the parameter a.
A standard choice for the mother wavelet is the so called *mexican hat function*:

$$g(t) = (D - t^2)\, e^{-t^2/2}$$

where $t = \sqrt{\sum_{i=1}^{D} (x_i/a)^2}$ is the euclidean distance (in a units) from the origin.

The mexican hat is one of the simplest functions satisfying the requirement (imposed by general wavelet transform theory) of giving a vanishing value when integrated over a D-dimensional infinite area. Since we work in 2 dimensions (D=2) the shape of g in the whole x-y plane can be obtained by rotating the plot shown in Fig. 4.5 around the vertical axis.
Since we have to deal with a discrete and finite distribution instead of a continuous function (i.e. $\rho(\mathbf{r}) \to \{n_i\}_{i=1,\dots N}$) the calculated f is:

$$f(\mathbf{r}') = \sum_{i=1}^{N} n_i\, g^{a,\mathbf{r}'}(\mathbf{r_i}) \tag{4.6}$$

Such a function selects (in the sense of assuming higher values at the centre of) circular structures whose radius is related to the value of a.

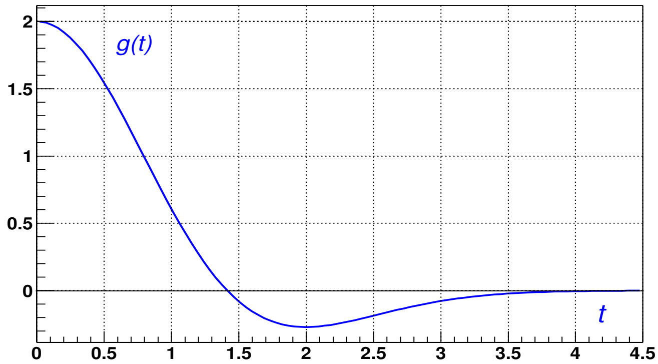

Figure 4.5: *Plot of the mexican hat function $g(t)$ for $D = 2$.*

4.4.2 `Circle`: maximal density over circular areas.

This method can be considered a simplified version of the previous one. The expressions for f_C and f_W are the same except for g. In this case the mexican hat is replaced by a step function:

$$g(t) = \theta(b - t) \tag{4.7}$$

In other words, $f_C(\mathbf{r}')$ is a sum of all the fired strips contained in a circle centred in $\mathbf{r}'$ and having a radius b.

4.4.3 Dependence on the parameters.

Both the smoothing algorithms depend on a radius parameter (a for `Wavelets`, b for `Circle`).
The behaviour of `Wavelets` has been investigated by using different values of the parameter a = 5, 8, 10, 15, 20 m

In Fig.4.6 the average error as a function of multiplicity has been plotted for three values of the parameter a (the two extreme ones and an intermediate value). It can be seen that large values of a improve the reconstruction of low multiplicity showers since a wider smoothing function is expected to be more effective in recovering the large point to point fluctuations that characterise these showers. In this sense a is the typical scale on which the radial symmetry of the density distribution can be recognised: the larger the fluctuations, the larger is the scale that has to be considered.

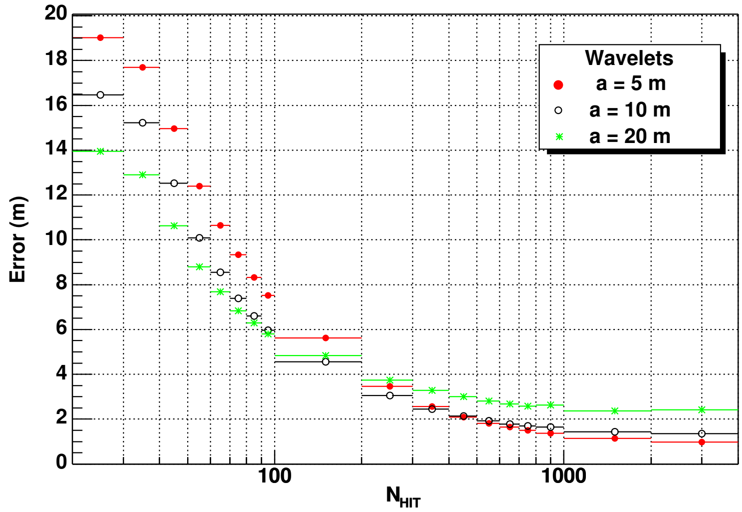

Figure 4.6: *Dependence of the* `Wavelets` *reconstruction performances on the scale parameter a. The average error is plotted as a function of event multiplicity.*

On the other hand, for high multiplicity showers the error increases when a moves to larger values. This effect is due to the finite size of the detector: the lack of information outside the active area implies that our actual integration area is a rectangle (plus the sparse areas of the sampling ring) instead of the infinite plane. This corresponds to substituting the mexican hat with zero outside the detector area. When considering points whose distance from the detector borders is $\leq a$, the abrupt change to non active area becomes evident because at $r \leq a$ the mexican hat function significantly differs from zero. Therefore, a systematic dependence on the core position has to be expected in a border region of width $\sim\ a$. The smoothing out of fluctuations largely compensates this effect at low multiplicities, while for high multiplicity events the result is an overall degradation of the reconstruction. Different values of the scale parameter a should be selected for the various multiplicity range. Nevertheless, to simplify the discussion a single intermediate value $a = 10\ m$ has been selected and will be used in the following.
`Centre` shows an analogous dependence on the parameter b. Of course the explanation is the same, thus results are not shown. The chosen default value for b is 3 m.

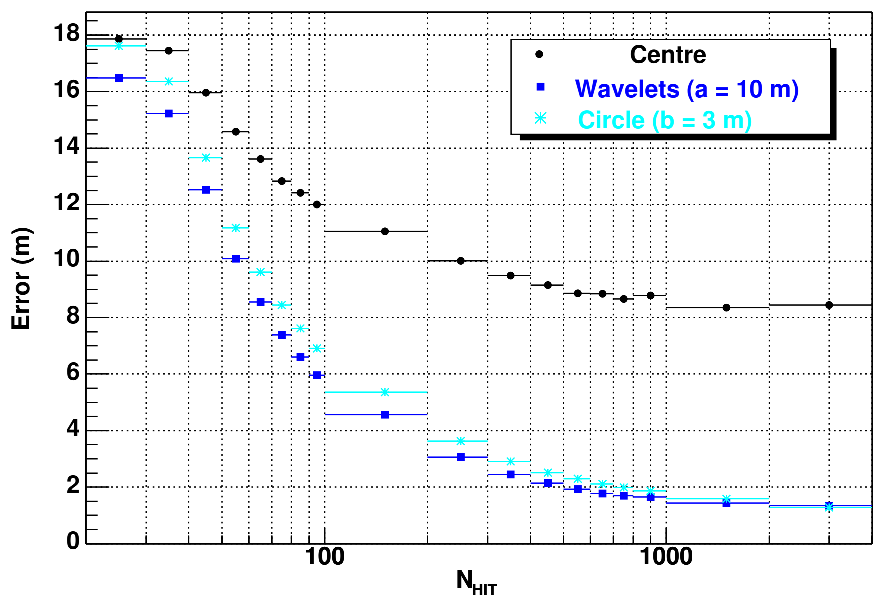

Figure 4.7: *Average error in core reconstruction for the smoothing algorithms. Results obtained for internal γ showers are shown as a function of the event multiplicity.*

4.4.4 Results.

Results obtained with the application of `Wavelets` and `Circle` are shown in Fig. 4.7. Both the algorithms give an average error <4 m for multiplicity higher than 200. This is a significant improvement with respect not only to `Centre` but also to tree algorithms (compare with Fig. 4.4 plotted in the same scale). It can be noted that the two algorithms become almost indistinguishable for $N_{hit} \geq 600$. This result suggests that `Circle` can be used to replace `Wavelets` in the very high multiplicity range. Since `Circle` is simpler and faster than `Wavelets` the replacement reduces computing time.

Since `Wavelets` reconstructs the core position with a lower average error than `Circle` at every multiplicity, in the following sections only `Wavelets` will be considered.

4.5 Likelihood algorithms.

The algorithms described in the previous sections make use of very loose hypotheses about the lateral distribution of charged particles. Actually they are simply based on the observation that the particle density is radially symmetric with respect to the shower axis and that it decreases with distance.

An alternative method to reconstruct the core position is to use the theoretical information about the shape of charged particles distribution. The widely used Nishima–Kamata–Greisen (NKG) function is the approximate analytical solution of the cascade equations [63] and provides a prediction about the expected density distribution. Here, however, the MC information is used: a reparameterization of the NKG functional dependence is needed to describe the observed distribution of MC showers taking into account the detector effects [64]. The density at a distance R form the shower axis can be described as:

$$\rho(R) = f\left(\frac{R}{R'_M}\right) \cdot \frac{\eta}{(R'_M)^2} \tag{4.8}$$

where η is the shower size, R'_M is the modified Moliere radius ($R'_M = R_M/D$ where $R_M = 133$ m is the Moliere radius at the YBJ site and D is a correction parameter to be determined) and

$$f\left(\frac{R}{R'_M}\right) = C \cdot R^{A-2} \cdot \left(1 + \frac{R}{R'_M}\right)^{-B} \tag{4.9}$$

A single set of parameters $\{A, B, C, D\}$ has been adopted to describe the lateral distribution of showers regardless of their energy. In other words it has been assumed a fixed lateral shape that depends on the primary particle properties only through a multiplicative factor η (the shower size). This common (average) shape has been determined by fitting the lateral profile of MC γ-induced showers. The values that have been used are listed in Tab. 4.1.

Parameter	value
A	1.81
B	2.93
C	0.65
D	4.17

Table 4.1: *Values of parameters used in Eq. 4.8 and Eq. 4.9*

Eq. 4.8, like the NKG function, describes only the expected average behaviour of density. Shower fluctuations have been taken into account by assuming that the local density of particles follows a Poisson distribution with a mean value given by Eq. 4.8. The probability of having m particles at a point $\mathbf{r}$ whose distance to shower core is $R = |\mathbf{r} - \mathbf{r_c}|$ can be written as:

$$p(m) = \frac{\mu^m}{m!}\, e^{-\mu} \tag{4.10}$$

where $\mu = \rho(R)$.

In the case of the ARGO–YBJ detector the use of area elements rather than points seems to be more appropriate to reflect the granularity of the detector. The detector area (including the ring) has been divided in a grid of N_S equal area elements. The obvious choice is to use the PAD area or multiple values of this logical "pixel". Four configurations have been studied (see Tab. 4.2).

Since the sum of Poisson distribution is a Poisson distribution with a mean value equal to the sum of their mean values, Eq. 4.10 holds also for the area elements. In this case, for the k-th area $\mu_k = \int_S \rho(R)dR$. This expression has been substituted with $\mu_k \simeq S \cdot \rho(R_k)$ where $R_k = |\mathbf{r_k} - \mathbf{r_c}|$ is the distance of the area centre $\mathbf{r_k}$ to the shower core $\mathbf{r_c}$.

Area Element	N_S	Area S ($PAD_x \times PAD_y$)	Area S (m^2)
PAD	18480	1×1	~ 0.4
RPC	1848	2×5	~ 3.9
Module	616	6×5	~ 11.6
Cluster	154	12×10	~ 46.4

Table 4.2: *Four possible choices for the area element. The total number of elements N_S is listed as well as the area of a single element (in unit of PADs and in m^2). See also Fig.2.3.*

With these starting hypotheses, it is possible to write down a likelihood function

$$LF(X|\eta, \mathbf{r_c}) \tag{4.11}$$

where $X = \{(\mathbf{r_i}, n_i)\}_{1=1,\dots,N}$ is the recorded pattern of the event. The shower size η and the shower core coordinates $\mathbf{r_c} = (x_c, y_c)$ are the unknown parameters.

The core reconstruction method, often used in the reconstruction of EAS arrays data, consists in finding the maximum likelihood estimators of $\mathbf{r_c}$. The explicit expression of LF depends on additional hypotheses that differentiate the two algorithms described below.

4.5.1 `LLF1`: ON/OFF area elements.

This first version of the maximum likelihood method for the ARGO–YBJ experiment was proposed in [64] and is mainly addressed to the reconstruction of low multiplicity events. For each area element the probability of being ON (at least one fired strip) or OFF is computed from Eq.4.10:

- $p_k(OFF) \;\equiv\; p_k(0) \;=\; e^{-\mu_k}$
- $p_k(ON) \;\equiv\; p_k(>0) \;=\; 1 - e^{-\mu_k}$

Assuming $\mu_k = S \cdot \rho(R_k) \ll 1$ (as expected for low multiplicities), the latter expression becomes $p_k(ON) \simeq \mu_k$.
The likelihood function is, in this case:

$$LF1 = \prod_{i=1}^{N_S^{OFF}} p_i(OFF) \prod_{j=1}^{N_S^{ON}} p_j(ON) \tag{4.12}$$

where the index i runs on the not fired elements, j refers to the fired ones, N_S^{ON} (N_S^{OFF}) is the total number of fired (not fired) area elements.
Because of the product structure of $LF1$, it is easier to work with its natural logarithm. Substituting $\mu_i = S\rho_i$ and using the short notation ρ_i for $\rho(R_i)$ (and analogous for j):

$$LLF1 = ln(LF1) = -S\sum_i \rho_i \;-\; \sum_j ln(\rho_j) \;+\; N_S^{ON} \cdot ln\,S \tag{4.13}$$

(the full expression requires a further substitution of the explicit form for ρ)

The function $-LLF1$ has been minimized by using the CERN MINUIT library [65] interfaced by the TMinuit class provided by ROOT [47].
The starting points for the three parameters are the total number of fired strip for η and the `Centre` reconstructed coordinates for the core position. A two steps minimization is used[3]. Firstly the likelihood estimator for η is found while keeping the core position fixed. Then the final value for the reconstructed core position is determined by a second minimization where

[3]This further approximation is needed to achieve convergence (G. Di Sciascio, private communication)

the previously computed value η is assumed as a fixed parameter.
The search for the core position is bounded[4] over a square centred at the detector centre and with a side of $120\,m$.

`LLF1` dependence on the area element.

Fig. 4.8 shows the average error obtained by using the `LLF1` reconstruction algorithm with different choices of the area elements. A better reconstruction is obtained when using smaller elements. A clear saturation effect can be seen at multiplicities $\simeq N_S$. In fact, considering only ON/OFF elements causes a loss of the information recorded by the detector (the number of fired strips in each element). In particular when a large fraction of the elements is ON, the algorithm deals with an almost uniform pattern.
On the other hand, the use of PADs cannot be afforded in terms of computing time because the computation of $LLF1$ requires, in this case, a sum of $N_S = 18480$ terms independently of the event multiplicity.
A compromise choice is to use RPCs: N_S is reduced by a factor 10 with a relatively small increase of the average error. In the following, when referring to `LLF1` the default choice of RPCs as area elements will be used.

4.5.2 `LLF2`: counting the fired strips.

This algorithm removes the approximations used in `LLF1` in order to fully use the recorded shower pattern. For each area element the probability of observing m_k particles is used instead of the simple ON/OFF probability:

$$LF2 = \prod_{k=1}^{N_S} p_k(m_k) \tag{4.14}$$

The corresponding log-likelihood function is, therefore:

$$LLF2 = lnS \cdot \sum_{k=1}^{N_S} m_k \; + \sum_{k=1}^{N_S} m_k \cdot ln\,\rho_k \; - \; S\sum_{k=1}^{N_S} \rho_k \; - \sum_{k=1}^{N_S} ln(m_k!) \tag{4.15}$$

where the sum appearing in the first term is the total number of fired strips (N_{strip}).

[4]It has been checked that an unbounded search does not improve the reconstruction neither for internal nor for external showers.

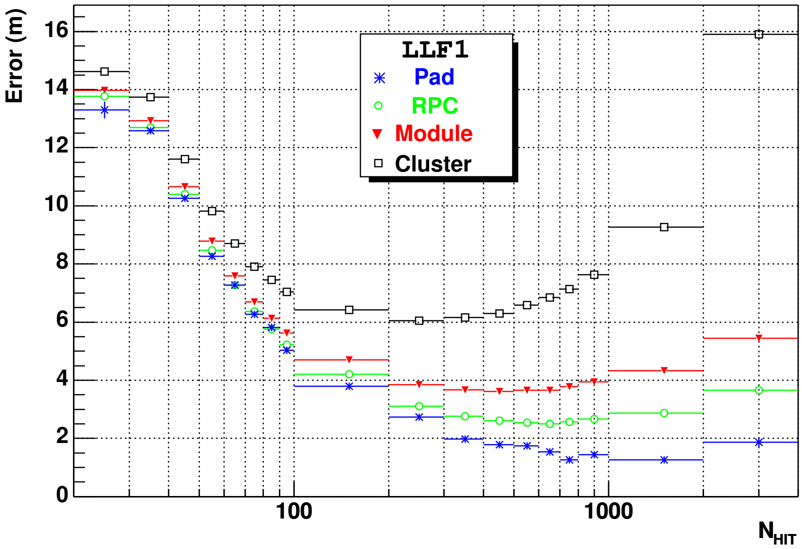

Figure 4.8: *Average error in* LLF1 *core reconstruction for different choices of the area element. Results refer to internal* γ *showers.*

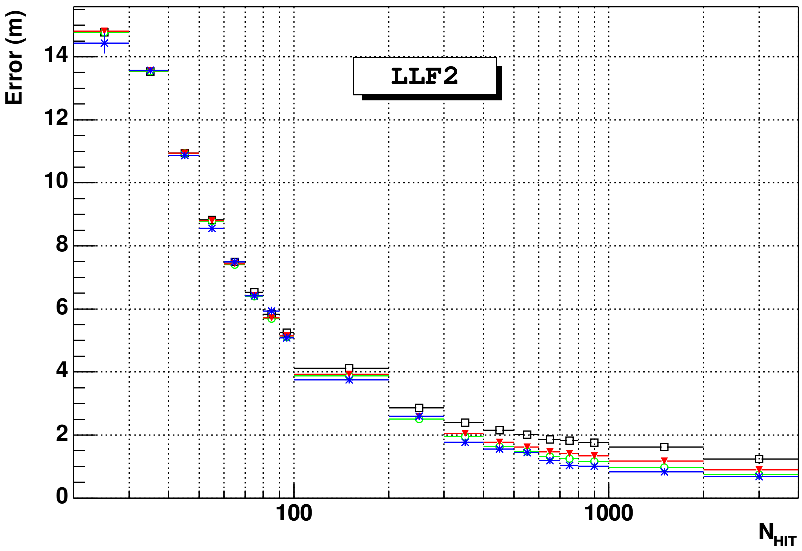

Figure 4.9: *Average error obtained when applying* LLF2 *with different area elements. The same symbols of Fig. 4.8 have been used.*

An interesting feature of this function is that the component of its gradient in the direction of the variable η is such that:

$$\frac{\partial\,(LLF2)}{\partial\eta} = 0 \Leftrightarrow \eta = \frac{N_{strip}}{S \cdot \sum_{k=1}^{N_S} \rho_k} \tag{4.16}$$

One of the variable parameters (η) can be expressed as a function of the other two (through the dependence of ρ on the core position). The problem reduces to the minimization of a two variable (x_c, y_c) function thus removing also the need of the two steps minimization approximation. A single (bounded) numerical minimization has been used.

`LLF2` dependence on the area element.

In Fig. 4.9 the dependence of `LLF2` performances on the chosen area is shown. It can be seen that the saturation effects completely disappear, as expected. Moreover, the dependence of the error on the area element becomes very small. In this case Modules can be used instead of RPCs. This choice reduces N_S of a factor 3 (a factor 30 if compared with the choice of PADs) with a proportional reduction of the required computing time.

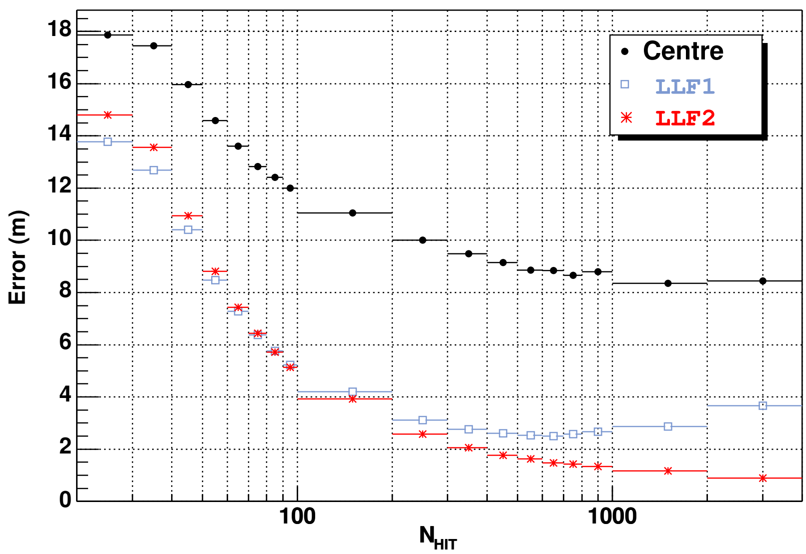

Figure 4.10: *Average error in the core reconstruction of internal γ showers.* `LLF1` *and* `LLF2` *are compared with* `Centre`.

4.5.3 Results.

The average error obtained by using the `LLF1` (RPCs) and `LLF2` (Modules) algorithms is shown in Fig. 4.10 together with `Centre` results.
For $N_{hit} \geq 100$ the error is less than $4\,m$ with an improvement of $\simeq 7\,m$ with respect to `Centre`. In particular `LLF2` reconstructs the core position within $\sim 2\,m$ (on the average) for $N_{hit} \geq 300$.
In the multiplicity range $N_{hit} \leq 70$ `LLF1` reconstructs the core position with a mean error $\simeq 10\%$ lower than `LLF2`. It has been checked that this effect is due to a very small fraction of showers that are completely misreconstructed by `LLF2`. Fixing the size in a preliminary step of minimization with the core position reconstructed by `Centre` (hence internal to the detector area by definition) prevents `LLF1` to move the core position too far from the starting point. This is no longer true for `LLF2` that in particular configurations of low multiplicity showers badly misplaces the core as if the detected event were the long tail of a high size external shower. When the external showers are taken into account, it turns into an advantage over `LLF1` which is biased toward the inner area. For internal showers the very large error, even if limited to a quite small fraction of events, produces the observed increase of the average error; indeed if the median value is compared, the difference reduces to $\simeq 2\%$. Therefore in the next sections only `LLF2` will be considered.

4.6 A comprehensive comparison of the core reconstruction of internal showers.

The first results given in the previous sections have been mainly used to prune the algorithms to be studied (only the best of each group will be considered) and to fix parameters (if any).
An overall comparison of the reconstruction performances as a function of multiplicity if given in Fig. 4.11 for internal γ showers. Note that here the median error is given instead of the average one. The error bars correspond to a 5% variation of the fraction (in other words the lower and upper limits refer respectively to the distances from the true core within which 45% and 55% of the showers are reconstructed). This gives a measurement of the local spread and asymmetry of the error distribution.
The analogue plot for background showers is shown in Fig.4.12.
In both cases the error strongly depends on the event multiplicity, roughly following a falling power law. As expected, the core of background showers is reconstructed with a higher error with respect to γ showers. In particular

up to $N_{HIT} \simeq 200$ the median error is larger than $10\,m$ independently of the reconstruction algorithm.

Another relevant feature of the core reconstruction is its dependence on the true core position on the detector carpet. Results are shown in Fig.4.13 for $N_{hit} \geq 100$. Each point represents the median error for showers with their core falling into a square frame whose internal and external half-sides are given by the lower and upper limit of the corresponding bin. `Centre` tends to move the reconstructed core towards the detector centre by definition, thus showing increasing systematic effects while approaching the border region. Minor but clear systematic effects can be seen also in the case of `MTree`, while `LLF2` and `Wavelets` seem to be independent of the core position, except for a border effect exhibited by `Wavelets` that has been already discussed.

As a final comparison the error dependence on the zenith angle is shown in the multiplicity range $N_{hit} \geq 100$. In order to span the whole zenith range up to 30° the Crab motion has been neglected. Fig.4.14 shows results obtained for a Crab-like flux uniform in the solid angle. The increase of the median error with θ seems to be very slow. It is interesting to notice that although `MTree` is the only algorithm that makes use of the time information, no evidence of a smaller dependence on the angle can be seen.

4.7 Taking into account external showers.

So far the analysis has been restricted to internal showers to gain an insight into the problem. However, the actual effects of core reconstruction on the experiment capability of detecting γ sources have to be studied on the whole set of triggering showers. Considering only results on internal showers has little sense since in principle we do not know if an event is to be classified as internal or not.

Taking into account also external triggering showers produces a degradation of the core reconstruction with respect to the case of internal events. As shown in Fig.4.15 (compare with Fig.4.11) the effect is more evident in the low range ($N_{hit} \leq 100$) and gradually decreases with N_{hit}. This reflects the distribution in multiplicity of external showers whose percentage contribution to the trigger rate falls down with N_{hit} (see Ch.3).

Since the contamination of external showers produces a worsening of the

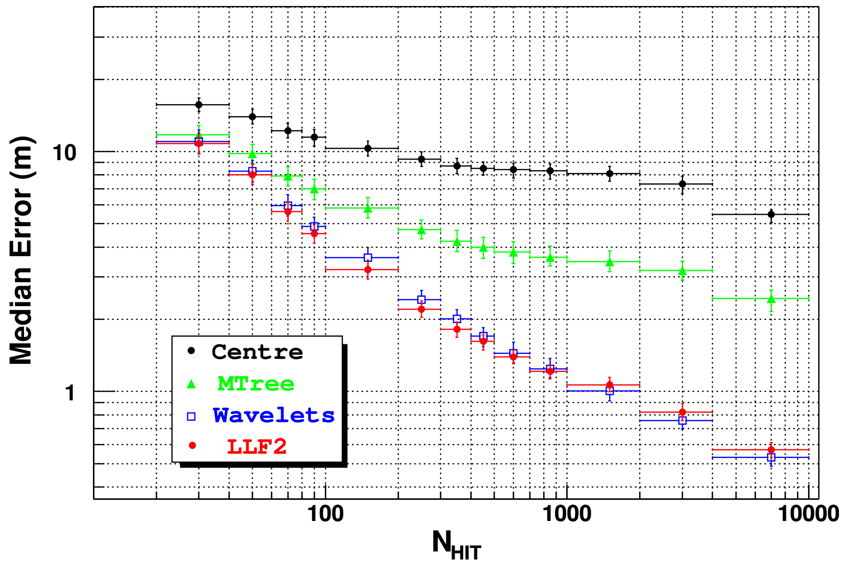

Figure 4.11: *Median error in the core reconstruction of internal γ showers.*

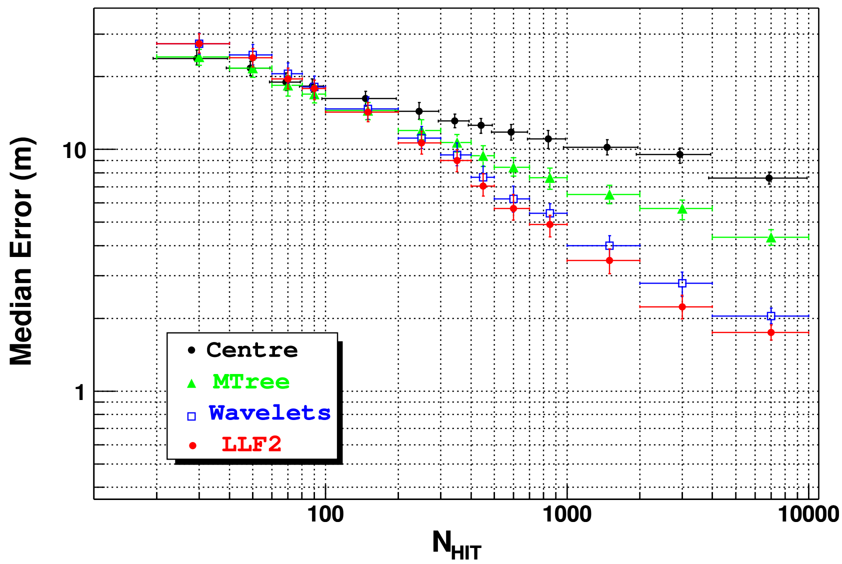

Figure 4.12: *Results obtained when the developed algorithms are applied to internal background showers. As in Fig.4.11, the median error is plotted versus the event multiplicity.*

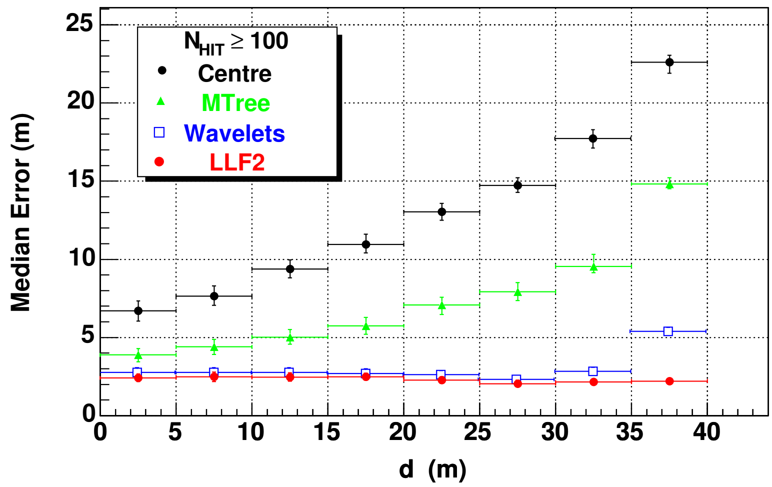

Figure 4.13: *Dependence of the median error on the true core distance to the detector geometrical centre. Results refer to γ internal showers with multiplicity ≥ 100* `Centre` *and* `MTree` *exhibit strong systematic effects.*

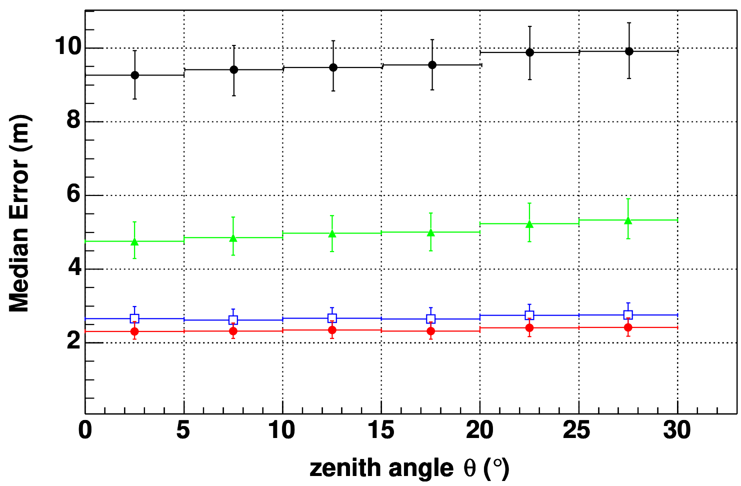

Figure 4.14: *Median error versus zenith angle for internal γ-rays with multiplicity ≥ 100. The same symbols of Fig.4.13 have been used. The Crab motion has not been considered: MC events are weighted to reproduce a Crab-like distribution uniform in the solid angle.*

angular resolution, it is desirable to reduce it. To do this the core reconstruction can be very useful: if a core reconstruction algorithm works properly we expect that in the case of external showers the core is more likely reconstructed outside the central carpet or in its border region. Fig.4.16 shows that this is the case of `LLF2` and of `Wavelets` (to a significantly lower extent), while `Centre` and `MTree` are clearly affected by the bias toward the detector centre already seen in the case of internal showers.

Retaining only the showers whose core has been reconstructed within a fiducial area A_{cut} seems to be a viable method to reduce the amount of external events.

4.8 Rejection of external showers.

In this section the effects of the application of an area cut will be studied. Four different choices for the area have been considered. Their values are listed in Tab.4.3.In particular A_2 corresponds to the area of the central carpet, A_4 to the total area of the detector (including the sampling ring). Showers are classified as internal/external with respect to the central carpet (A_2) rather then to the varying fiducial area.

Results depend on the core reconstruction algorithm, on the choice of the

Notation	Dimension ($CLU_x \times CLU_y$)	Area (m^2)
A_1	8×11	$\sim 63.7 \times 64.2$
A_2	10×13	$\sim 79.6 \times 75.8$
A_3	12×15	$\sim 95.5 \times 87.5$
A_4	14×17	$\sim 111.4 \times 99.2$

Table 4.3: *Fiducial areas that have been considered for the application of the cut on the reconstructed core position. Their dimensions are given in unit of Clusters as well as in m^2.*

area and on event multiplicity. In order to simplify the treatment, only the case of `LLF2` will be fully discussed here.

Fig.4.17 shows the residual contamination of external showers (i.e. the percentage contribution of external events to the sample that survives the area cut) as a function of multiplicity. A reduction of the contamination that increases when keeping smaller areas can be seen both for γ and background showers. However the rejection of external events is more effective in the case of signal while the percentage of external protons and helium nuclei

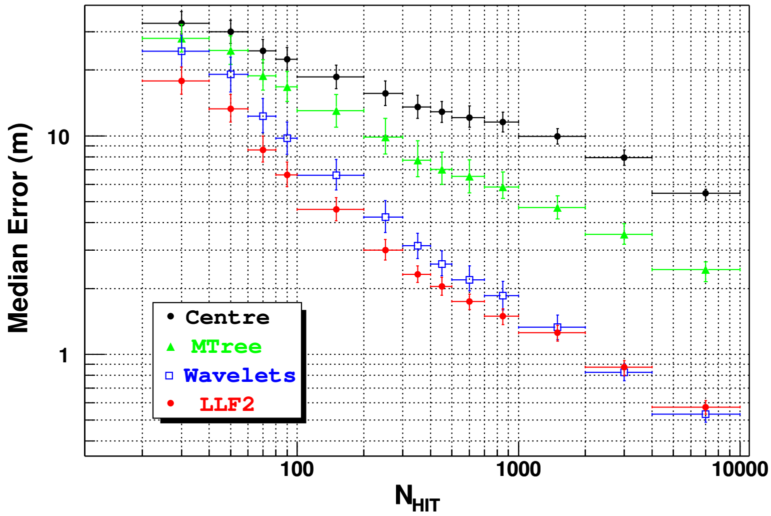

Figure 4.15: *Median error in core reconstruction versus the number of fired PADs. Results refer to the whole set of triggering showers (internal and external).*

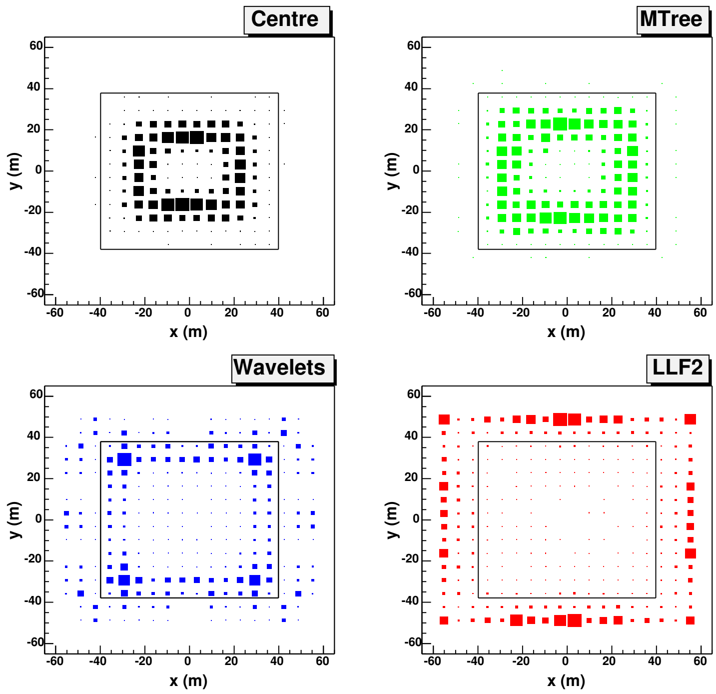

Figure 4.16: *Distributions of the reconstructed core positions for external γ-induced showers with a multiplicity* $\geq$ 100. *The dimension of the ARGO–YBJ central carpet is represented by the inner rectangle.*

remains well above the 50% level in the low multiplicity range. A similar behaviour (with a lower rejection power) is found when applying other algorithms.

In order to apply the "optimized sensitivity" criterion stated at the end of Ch.2, S can be rewritten in the simplified form:

$$S(\Delta N_{hit}) \;=\; \underbrace{\frac{N_\gamma}{\sqrt{N_B}}}_{F}\;\underbrace{\frac{\xi(\psi)}{\sqrt{2\pi(1-cos\psi)}}}_{G}\;\sqrt{t} \qquad (4.17)$$

where $N_\gamma(N_B)$ is the number of signal (background) events observed in one day (per steradian in the case of background) and retained after the analysis cut, t is the observation time expressed in days, the other symbols are the same as in Eq.2.2. The quantities (except for t) depend on ΔN_{hit}.
The analysis dependent part of S has been factorized into a term: G, containing all the information about the angular resolution, and a term F, representing the ratio of the signal to the background fluctuations.
Note that the effect of the area cut on G relies only on the reduction of

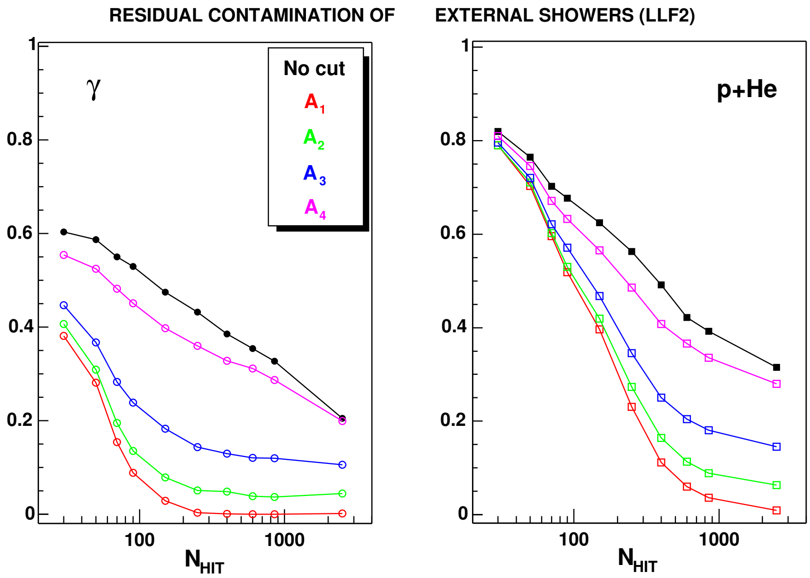

Figure 4.17: *Ratio of external showers to the total when keeping events with core reconstructed (*`LLF2`*) within a fiducial area A_{cut} The case of no cut is shown for comparison.*

the external showers contamination for γ rays. The rejection of external background events does not affect this term.
On the other hand the variation of F depends on the percentage of retained events regardless of their classification as internal/external. If we use as reference point the number of triggering events (denoted with a superscript 0), the application of an area cut reduces both the signal and the background:

$$\begin{array}{rcl} N_\gamma^0 & \longrightarrow & N_\gamma = \epsilon_\gamma \, N_\gamma^0 \\ N_B^0 & \longrightarrow & N_B = \epsilon_B \, N_B^0 \\ F^0 = \frac{N_\gamma^0}{\sqrt{N_B^0}} & \longrightarrow & F = \epsilon_F \, F^0 = \frac{\epsilon_\gamma}{\sqrt{\epsilon_B}} \, F^0 \end{array}$$

An increase of the factor F can be obtained only if $\epsilon_B < \epsilon_\gamma^2$. Unfortunately, this condition is never met. Since, as previously shown, the rejection retains a larger fraction of background than signal events the overall effect is a reduction of F ($\epsilon_F \leq 1$), as shown in Fig.4.18.

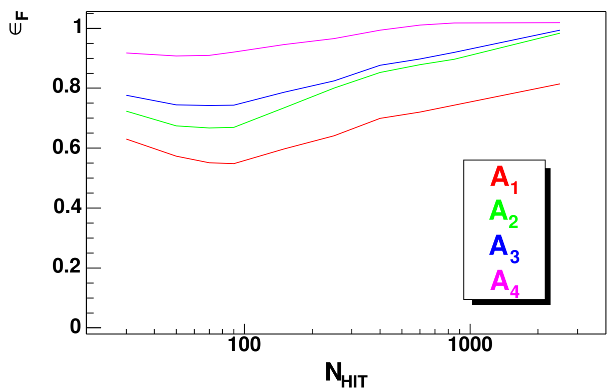

Figure 4.18: *Variation in the ratio of the signal to the background fluctuations ϵ_F (see text) when different area cuts are used.*

On the other hand, the factor G is expected to increase (with respect to the case of no cut). At this step the variation of G cannot be quantified. From a merely qualitative point of view, we can say that the application of a cut is the "right" choice only if the increase of G compensates for the loss in the signal-to-noise ratio.

A relevant result of this first analysis is that external showers can play an important role for the ARGO–YBJ sensitivity. In fact, external γ events, although if less reliably reconstructed, contribute to the signal being the larger part of the triggering showers at low multiplicities. They should be rejected (and in this case the result is a loss of signal) if and only if a significant improvement in the detector angular resolution can be obtained in turn. The optimal choice will be at some equilibrium point between the two opposite effects.

A conclusive comparison can be performed only by studying simultaneously the effects of the reconstruction chain (core reconstruction algorithm + area cut + direction reconstruction algorithm) on F and G. Therefore, it is postponed to Ch.6 after the description of the direction reconstruction methods given in Ch.5.

Chapter 5

Angular resolution.

The most important issue within the ARGO–YBJ data analysis is the reconstruction of the primary particle direction. A good angular resolution not only allows for a precise source localization, but is also an essential requirement to achieve higher sensitivity since it determines the size of the angular bin opened around the source (or the binning in the sky map in the case of blind search) and, in turn, the amount of background.

This chapter is devoted to the description of the methods implemented in the ARGO–YBJ data analysis code for the direction reconstruction. The effects of the core reconstruction on the angular resolution will be studied as well.

5.1 The shape of the shower front.

So far the shower front has been described in very broad terms as a flat disk orthogonal to the direction of the primary particle. A closer look at a typical shower (Fig.5.1) shows that particles are distributed with an average time delay and a temporal spread increasing with their distance from the shower axis. Both these effects depend on the multiple Coulomb scattering that is also responsible for the lateral spread of air showers.

Scattered particles travel a longer path length and have a higher probability of energy losses with respect to particles propagating along the axis. The resulting typical curvature can be clearly seen (red line) when the most energetic particles of the shower (i.e. the fastest ones) are considered. Fig.5.2 shows the mean value and root mean square (RMS) of the arrival time of charged particles as a function of the distance from the shower core. The RMS gives only a rough idea of the temporal spread. Actually, at a given

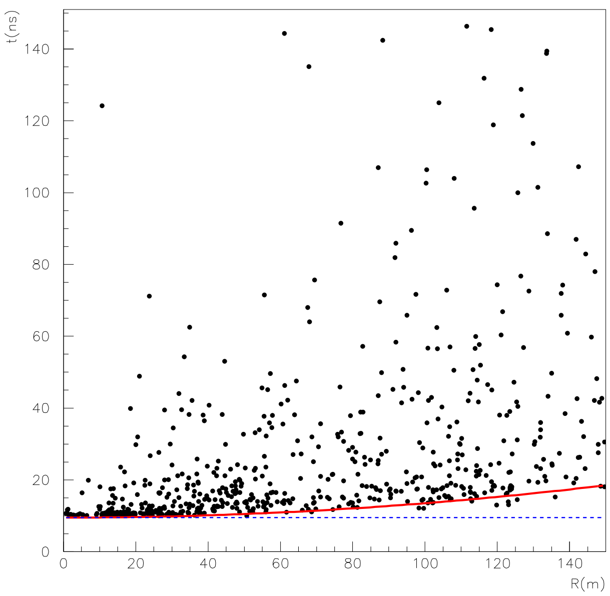

Figure 5.1: *Arrival time of charged particles in a typical vertical shower initiated by a 1 TeV γ-ray as a function of the distance from the core position.*

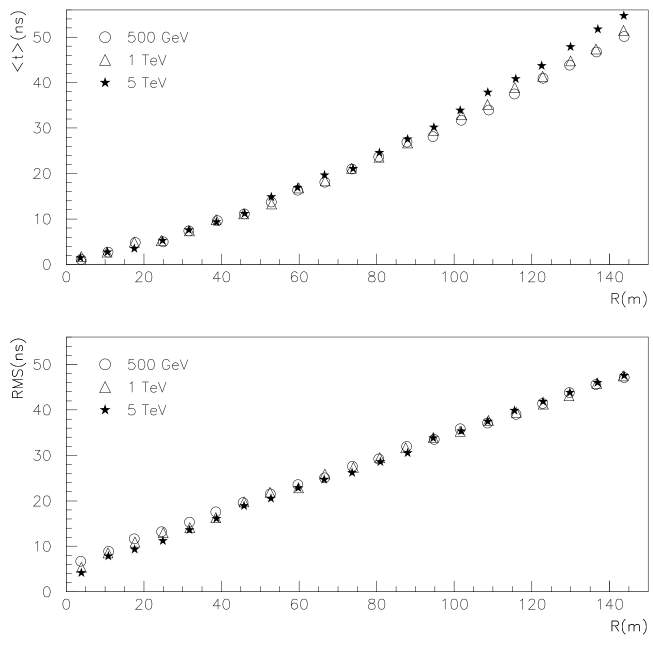

Figure 5.2: *Mean value and RMS of the particles arrival time versus the distance from the core position. Results refer to vertical showers induced by photons with fixed energy (represented by the different symbols) at the ARGO–YBJ altitude.*

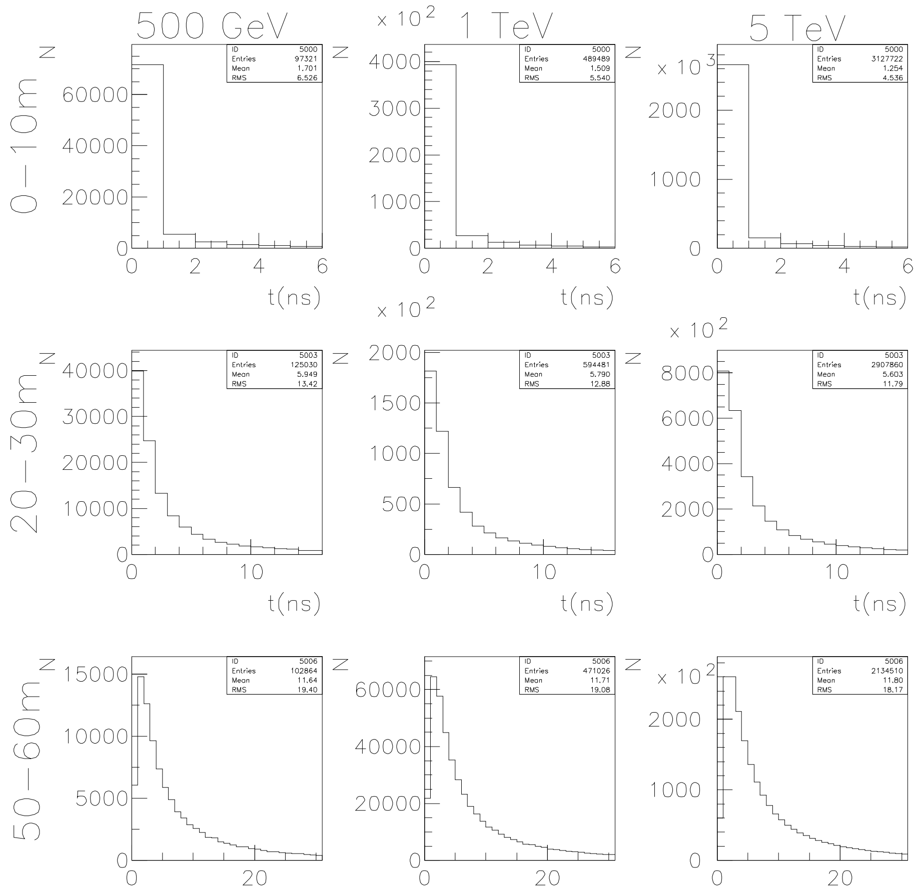

Figure 5.3: *Distribution of particles arrival time in three ranges of distances from the shower core. Results are shown in the case of γ showers with fixed energy. .*

distance from the shower axis, the arrival time distribution is characterised by a long tail of particles with large delays (see Fig.5.3).

The first plot of Fig.5.2 shows that the time structure has a parabolic shape with an average temporal deviation from the planar shape of about 30 ns at a distance of 100 m.
Up to a distance of 40-50 m the shower front can be described as a cone [66]. Given the dimensions of the ARGO–YBJ central carpet, a conical shape can be used to describe the arrival time of the shower. Higher order corrections can be important for external showers, however in this case any potential improvement from a better description of the front is eliminated because the shower core position cannot be well determined, as discussed in Ch.4.

5.2 Algorithms for the direction reconstruction.

The algorithms described below are based on a common strategy for the direction reconstruction. An iterative procedure of χ^2 minimization is used. It should be said that given the non–gaussian time distribution of particles the use of a least squares fit is not appropriate in principle. However it will be shown that minimizing χ^2 has a great advantage of being a problem with an analytical solution. And, on the other hand, it is quite difficult to model the time fluctuations in order to accomplish a better description of the shower front. The iterative procedure allows for a progressive symmetrization of the distribution by removing, at each step, hits giving large contribution to the χ^2

Given an assumption on the shape (plane or cone) of the shower front, in each iteration the direction cosines[1] of the shower axis $\{L_1, L_2, L_3\}$ (and other parameters if any) are determined by minimizing the appropriate χ^2 function. After the first iteration the hits whose time distance (residual) from the fitted shower front is $> n_T$ (expressed in ns) are rejected. In the k–th ($k \neq 1$) iteration a similar selection is applied by computing the root mean square σ_{res} of the residuals. An hit is retained (hence used in the $(k+1)$–th iteration) only if its residual is less than $n_\sigma \, \sigma_{res}$. A minimum number of 5 survived hits is required at each step to perform the χ^2 minimization.

n_T, n_σ are tuneable parameters. The dependence of the reconstruction on these parameters has been extensively discussed in [67]. Here the values of tuneable parameters as well as the criterion to stop the iteration procedure, are assumed optimized as given by [68] for the Planar and Conical fit and by [69] for the Conical fit with fixed α.

5.2.1 Planar fit

Using the notation of Ch.4, when assuming a planar shape of the shower front the χ^2 function is:

$$\chi^2 = \sum_i n_i(c \cdot (t_i - T_0) - x_i \cdot L_1 - y_i \cdot L_2)^2 \tag{5.1}$$

[1] Actually only two of them have to be determined since they satisfy the condition $L_1^2 + L_2^2 + L_3^2 = 1$.

where the sum is over N terms at the first step, and over the surviving hits in the following ones; (L_1, L_2, L_3) are the direction cosines of the shower axis (perpendicular to the plane). T_0 is an absolute time offset common to all the fired PADs in a given event. The fit parameters are, therefore, the arrival time T_0 of the shower plane and two directional cosines L_1 and L_2. $\nabla\chi^2 = 0$ results in a system of linear equations that can be analytically solved.

In this case $n_T = 100$ ns, $n_\sigma = 2.5$. The iterative procedure stops when the angle between the directions reconstructed at the current step and the direction of the previous step is less than $0.1°$ or if a maximum of 30 iteration is reached without meeting this requirement.

Results of the planar fit are shown in Fig.5.4 for internal and all γ–induced showers. The quantity ψ whose median value ($\pm 5\%$) is plotted versus multiplicity, is the angle between the reconstructed and the true direction (the latter given by the simulation code).

At low multiplicity fluctuations dominate: as the multiplicity increases, fluctuations decrease allowing for a more precise determination of the direction. Around 200-300 hits, the effect of the conicity can be seen since the probability of detecting particles at large distance from the core increases with the shower size. The reconstruction worsens due to the non appropriate description of the shower front. Finally at extremely high multiplicity the error goes down again: this is due to the fact that showers with such a high number of hits are not only internal but have the shower core near to the detector centre (see also Fig.5.5). In this particular configuration the deviations from the plane are almost symmetrical. Therefore, the planar fit, averaging over deviations approaches the true direction.
This effect, together with the difference between the results obtained for internal events and for all showers, demonstrates that the angular resolution depends on the core position as explained at the beginning of Ch.4.
In any case the median ψ is always $\geq 1°$. This is an unsatisfactory result particularly in the highest multiplicity range.

5.2.2 Conical fit

This algorithm is not a pure conical fit: it starts when the planar fit has converged and makes use of the previous cuts and reconstructed direction. Therefore, it should be properly called "conical correction fit".

When using a conical model of the shower front two more quantities have to be introduced: the conical correction α (i.e. the deviation, expressed in ns

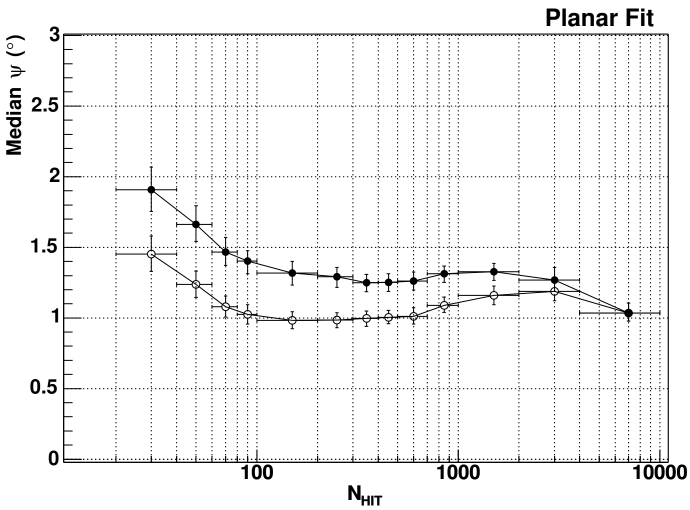

Figure 5.4: *Median value of the angle between the true and the planar fit reconstructed direction of the primary particle as a function of the shower multiplicity. Filled circles refer to all the γ-induced showers,empty circles to internal γ showers.*

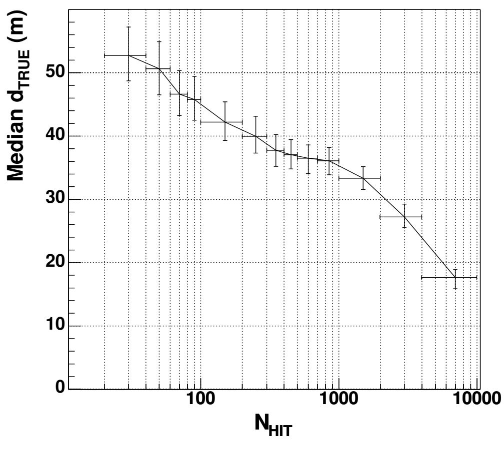

Figure 5.5: *Median distance of all γ-induced showers from the detector geometrical centre versus event multiplicity.*

m^{-1}, of the cone surface with respect to the plane perpendicular to its axis) and the distance R_i of the i–th hit from the cone axis. The least squares fit requires the minimization of:

$$\chi^2 = \sum_i n_i (c \cdot (t_i - T_0) - x_i \cdot L_1 - y_i \cdot L_2 - c \cdot (\alpha R_i))^2 \qquad (5.2)$$

Since R_i depends on the axis direction and on the cone vertex position, the minimization results in a system of non-linear equations. In order to obtain an analytically solvable system, this dependence has been neglected. Starting with the results of the planar fit, at each step R_i has been substituted with the distance from the axis as determined by the previous iteration (by the planar fit at the first step), while the cone vertex has been taken fixed at the reconstructed core position. Therefore a single parameter (α) has to be determined in addition.

The values of the tuneable parameters and the iteration stopping criterion are the same as in the planar fit. The conical fit depends on the algorithm used for the core reconstruction. This fact introduces a further dependence on the core coordinates with respect to the planar fit. For simplicity only `LLF2` will be considered in this chapter. Results as a function of the number

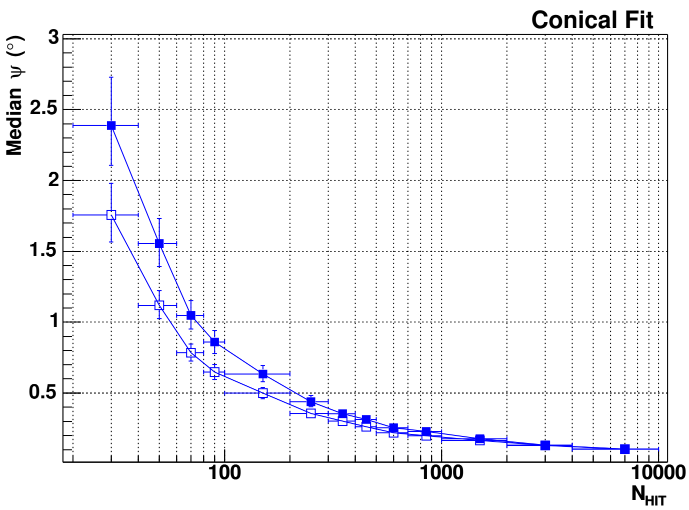

Figure 5.6: *Median space-angle difference between the direction reconstructed with a conical fit and the true one. Filled symbols represent the results obtained when all the γ showers are reconstructed, empty squares refer to internal showers only.*

of fired hits are shown in Fig.5.6. For $N_{hit} \geq 80$ the median value of ψ is better than 1° even for external showers. Moreover its value decreases up to $\sim 0.1^\circ - 0.2^\circ$ in the last bins. On the contrary, at low multiplicity the reconstruction is unsatisfactory and seems more dependent on the core position, being much better for internal showers.

5.2.3 Conical fit with fixed α (Conical2)

Given the poor performances of the conical fit at low multiplicity, an alternative approach has been studied.
A deeper analysis of the conical fit shows that sometimes non-physical negative values of α result from the fit. Moreover, the distribution of reconstructed α has a sharp peak around a value of 0.03 ns m^{-1} as can be seen in Fig.5.7 in a particular configuration[2]. For these reasons a conical fit with a fixed α has been developed. The χ^2 function is identical to the χ^2 of the previously discussed conical fit, with the only difference that a parameter has been eliminated, making this fit equivalent to the planar one.
In [67] the variation in the angular resolution has been studied as a function of the fixed value of α. Results shown in Fig.5.8 indicate that the best choice is α=0.03 ns m^{-1}.
In this case 3 iterations of planar fit are used with a cut at $n_T = 50\,\mathrm{ns}$ after the first step. The value for n_σ used after the second and third step is 1.5. Then, a single step of conical correction gives the final reconstructed direction.

Fig.5.9 shows that the dependence on the core position has been reduced: a relatively small degradation of the median ψ can be seen when taking into account also external showers.

In the following this algorithm will be referred to as “Conical2”.

[2]It has been shown in Fig.5.2 that the all particles arrival time has an average deviation from the plane of 3 ns m^{-1}. The iterative fit selects the most energetic particles whose deviations are about ten time smaller.

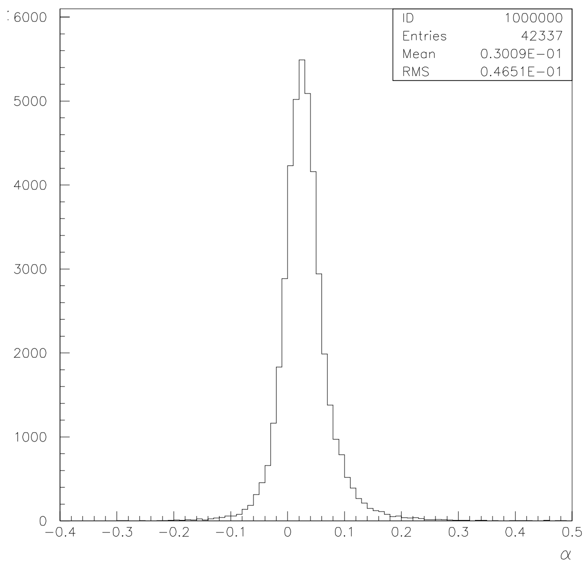

Figure 5.7: *Distribution of the conical parameter α after 1 conical fit for showers induced by 1 TeV γ with $\theta = 20°$* [67]

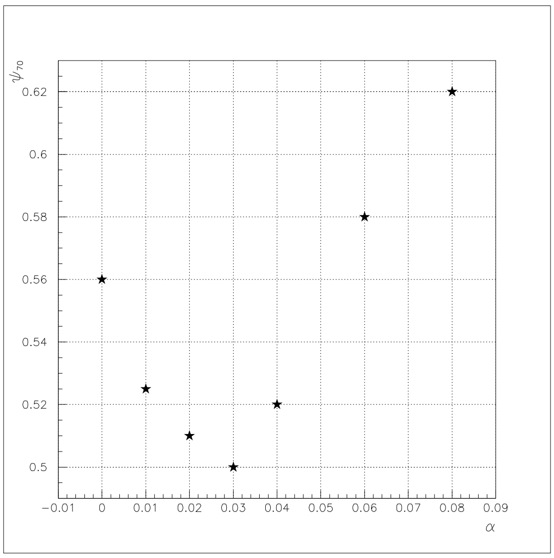

Figure 5.8: ψ_{70} *(i.e. the value of ψ within which 70% of the showers are reconstructed) as a function of the fixed value of the conical parameter. Showers with multiplicity 200-250 and core at the center of the carpet have been selected* [67]

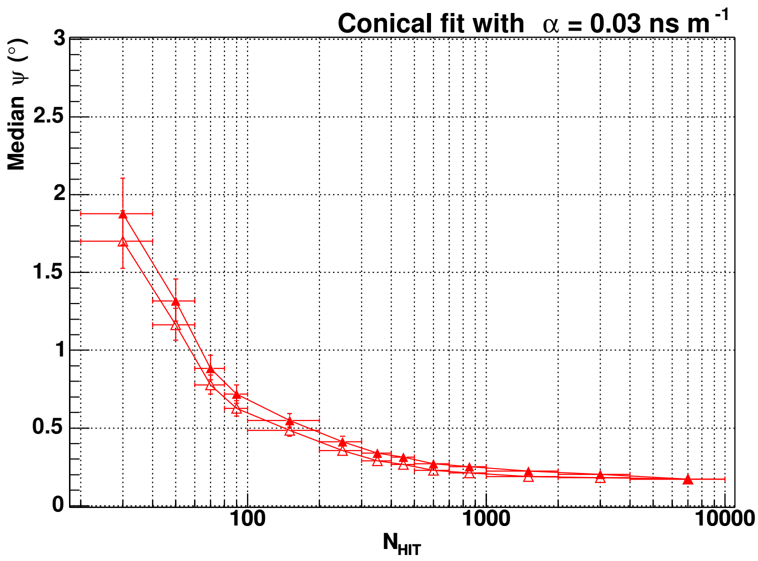

Figure 5.9: *Median ψ versus multiplicity in the case of internal (empty symbols) and all γ events (filled triangles) whose direction has been reconstructed by a conical fit with a fixed value of the conicity parameter α.*

5.3 Comparison of the direction reconstruction algorithms.

Fig.5.10 summarises the results obtained up to now. The first general result is that the angular reconstruction significantly depends on event multiplicity (as the core position reconstruction).

By comparing the different methods, it can be seen that both the conical fits improve the reconstruction, with respect to the simple planar fit, in the whole multiplicity range $N_{hit} \geq 60$. For showers with a lower number of fired PADs the planar fit seems to be the best performing algorithm if internal showers are selected. Therefore, a conclusive comparison has to take into account the rejection of internal showers. The two conical fits, up to $N_{hit} \simeq$ 600–800, are almost equivalent in the reconstruction of internal events, while including external showers degrades the performances of the conical fit with variable α more than those of Conical2. For $N_{hit} \geq$ 600–800, on the other hand, the use of an additional variable parameter improves the reconstruction.

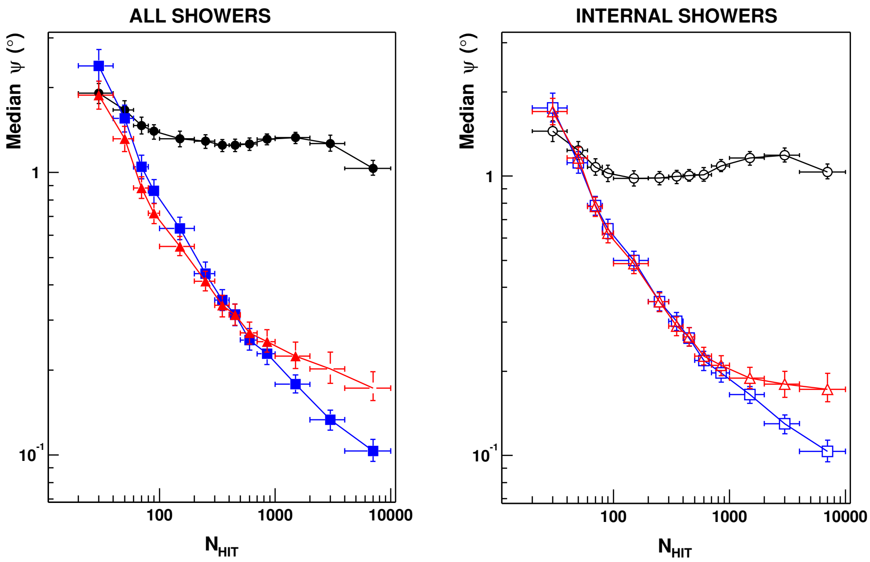

Figure 5.10: *Median value of the space angle difference between the reconstructed and the true shower directions. Results obtained for all γ–induced shower (left plot) and for internal only (right) are shown versus multiplicity. Symbols are the same used in the previous section: circles for Planar, squares for Conical, triangles for Conical2*

Fig.5.11 shows the dependence of the reconstruction on the true core distance from the detector centre. Median errors in the multiplicity range $N_{hit} \geq 100$ are shown. In the case of a planar fit, the median space-angle difference increases almost linearly with the distance. As inferred by other results, Conical exhibits a dependence on the core position much larger than Conical2. Fig.5.12 helps to understand if this dependence is intrinsic or dependent on a core misreconstruction. Given that Planar does not depend on the goodness of core reconstruction, the black line shows that angular and core resolutions are correlated. The explicit use of the core position in the two conical fits is expected to increase this correlation. The red line refers to Conical2 and is roughly parallel to the black one; this means that the degradation due to a misreconstructed core position is small, at least for an error in the core location $< 40m$. On the contrary, the median ψ given by Conical is more rapidly increasing, showing that a significant part of its dependence on the core position is actually due to the inaccuracy in core reconstruction.

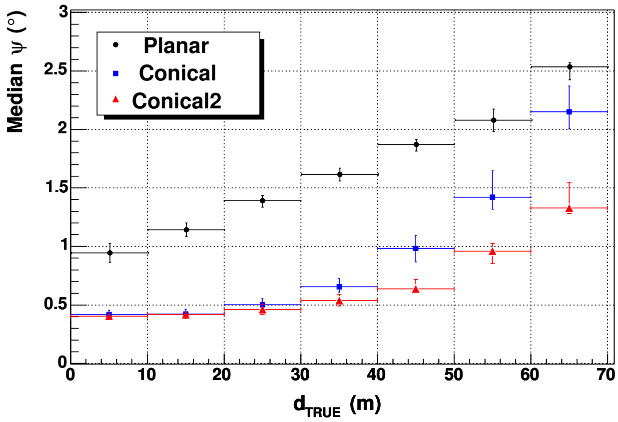

Figure 5.11: *Angular resolution dependence on the true core position for* $N_{hit} \geq 100$. *Median* ψ *is plotted as a function of the distance between the true core and the detector centre.*

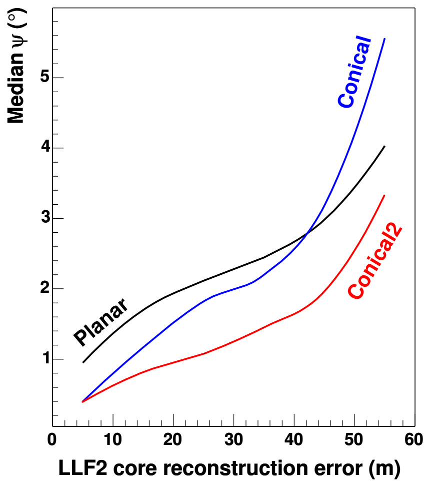

Figure 5.12: *Angular resolution versus* `LLF2` *error in core reconstruction. Continuous line joining the computed points have been plotted. Events with multiplicity* ≥ 100 *have been considered.*

Finally, the dependence of the angular reconstruction on the zenith angle is shown in Fig.5.13. As observed for the core reconstruction, also in this case the dependence is very small.

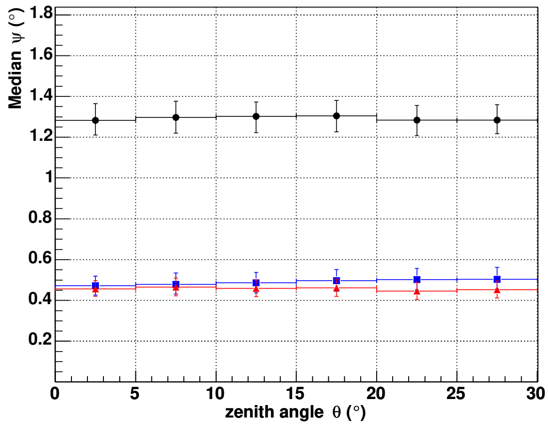

Figure 5.13: *Median value of the space angle difference between the reconstructed and the true shower directions as a function of the zenith angle. Results obtained for showers with* $N_{hit} \geq 100$ *are shown (circles=Planar, squares=Conical, triangles = Conical2).*

5.4 Choice of the opening angle.

So far, the median ψ value has been used to have a quantitative measurement of the angular resolution. However the angle ψ_b relevant for real data analysis and sensitivity calculation is the half-opening of the circular bin centred at the source position.

As previously discussed, the angular resolution appears in the expression of the sensitivity through the factor:

$$G(\psi) = \frac{\xi(\psi)}{\sqrt{2\pi(1 - cos\psi)}} \tag{5.3}$$

where $\xi(\psi)$ is the fraction of signal events reconstructed within ψ degrees from the true source position.
The opening angle ψ_b is chosen as the value of ψ such that $G(\psi_b)$ corresponds to the maximum value of G.

Defining the point spread function (PSF) as the spatial distribution of the reconstructed direction around the true source direction, it can be demonstrated [70] that, if PSF is a two–dimensional gaussian with a standard deviation σ, then

$$\psi_b = 1.58\,\sigma \tag{5.4}$$

In this hypothesis, $\xi(\psi_b) \simeq 0.715$. For this reason it is often called ψ_{70}.
In this case the numerator of G has a fixed value; therefore, a smaller ψ_{70} implies a larger value of G. Since the median value of ψ corresponds to $\sim 1.18\ \sigma = 0.74\ \psi_{70}$, the comparison of median ψ suffices to get the better G.

In Fig.5.14 four examples of events distributions versus ψ are shown, together with the corresponding $G(\psi)$. The angle ψ_b (continuous line in the plots on the right) is the angle corresponding to the maximum of G, while ψ_{70} has been determined as the angle within which 70% of the showers have been reconstructed. What emerges is not only that ψ_b differs from ψ_{70} but also that ψ_b can be either larger or smaller than ψ_{70} depending on the reconstruction and on the multiplicity.
This effect can be understood considering that showers with different core positions contribute to the same multiplicity range. Assuming that for a fixed core position the PSF is a gaussian, the resulting PSF over a multiplicity range is a sum of gaussians with different σ weighted with the percentage contribution of each core distance. A description of such a distribution is complicated by systematic dependence of the direction reconstruction on the core position. Moreover, if area cuts are used, the PSF changes since the contribution of different core positions is altered.
This means that the distribution of reconstructed events, even if sharply peaked, is non-gaussian (therefore Eq.5.4 does not apply) and that its shape cannot be described with a generic form that can be applied in each possible configuration. The better approach in such a situation is to make no hypotheses about the distribution: ψ_b will be determined in each particular case by finding the maximum of $G(\psi)$ as obtained from the simulations, thus making use of its definition only.
Of course, what has been said for the Gauss distribution does no longer apply. Since $\xi(\psi_b)$ is variable, the comparison of ψ_b has little sense. In this case the relevant quantity is $G(\psi_b)$.

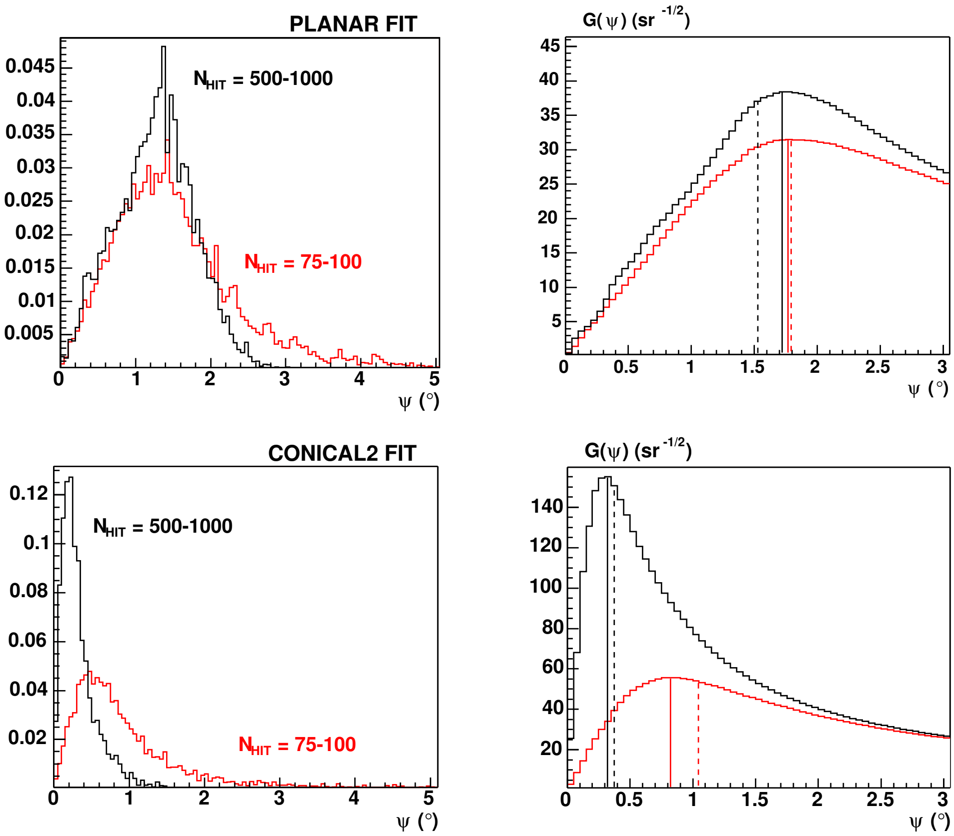

Figure 5.14: *Plots on the left show the normalized distributions of events as a function of ψ in two selected multiplicity ranges and for two different reconstruction algorithms. On the right the corresponding $G(\psi)$ is shown. Vertical lines represent the value of ψ_b (continuous) and ψ_{70} (dashed).*

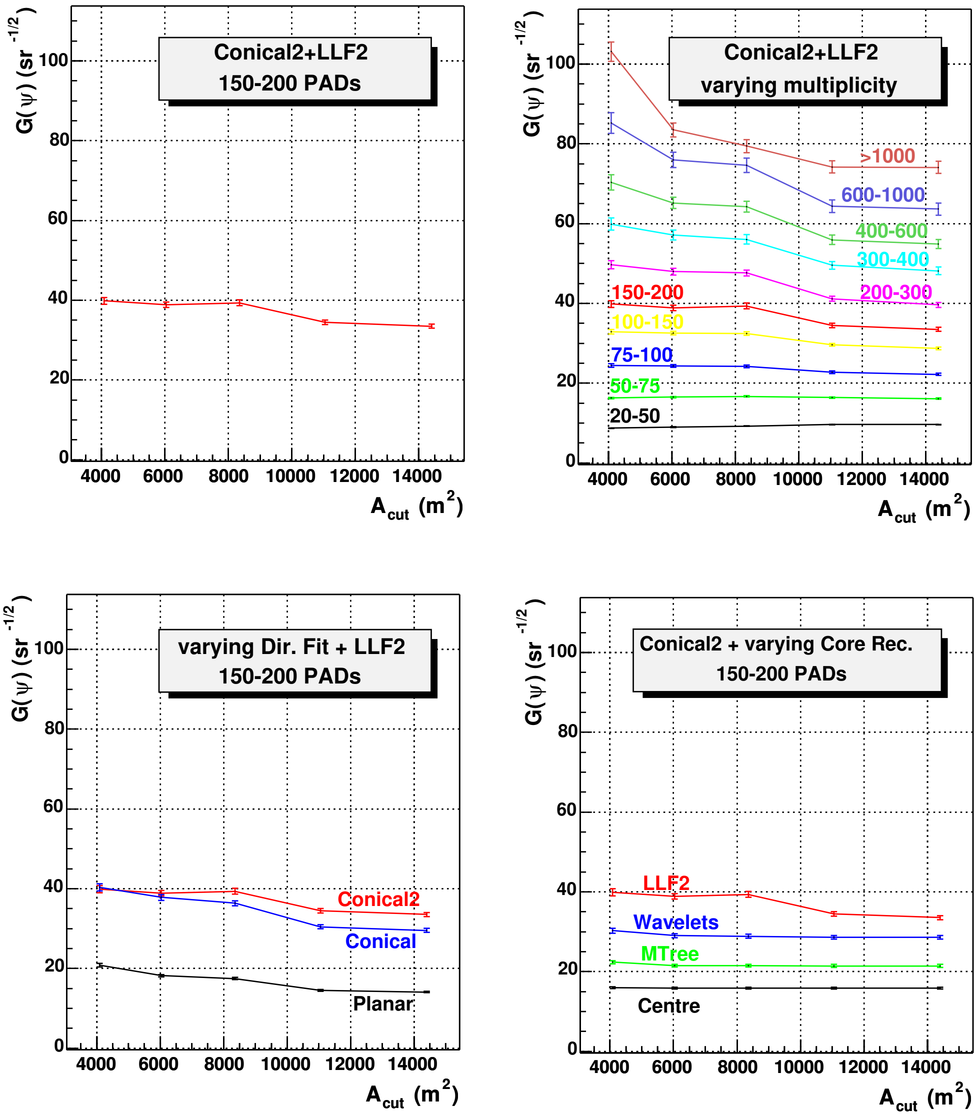

Figure 5.15: *Values of $G(\psi)$ as a function of the area cut (the last point corresponds to no area cut). A selected multiplicity range, core reconstruction and direction reconstruction has been fixed and is shown in the upper left plot. The other plots show how the dependence varies with varying multiplicity (upper right), direction reconstruction algorithm (lower left), and core reconstruction (lower right).*

5.5 Effects of an area cut

It has been shown in Ch.4 that the contamination of external showers can be reduced by retaining only the showers whose reconstructed core falls within a selected area.
Now the improvement in the direction reconstruction can be quantified by computing the variation of $G(\psi)$. The upper right plot in Fig.5.15 shows that this variation for a fixed multiplicity range (100-150 PADs), and a particular choice of the core reconstruction and direction reconstruction algorithms (`LLF2` and Conical2) is of about the 14%. Other plots show what changes when one of the parameters (multiplicity, core and direction algorithms) varies. An improvement in the angular resolution can be in general seen when a smaller area is chosen, anyway the quantitative effect depends on the setting of parameters. Therefore, the expected improvement is confirmed but an ultimate comparison has to be carried out as a function of the full event reconstruction chain. Moreover, results on $G(\psi)$ have to be studied together with the reduction in the signal rate due to the applied cuts. This will be done in the following chapter.

Chapter 6

Sensitivity to point-like sources.

This chapter is devoted to the estimate and the discussion of the ARGO–YBJ sensitivity for the detection of γ–ray point sources. The first goal of this chapter is to fully compare all the possible reconstruction chains by combining the core reconstruction, direction reconstruction methods and area cuts described in previous chapters in order to determine an optimal event reconstruction strategy. Effects of the uncertainties in the knowledge of the source and background fluxes will be discussed in the case of the sensitivity to the Crab Nebula.
Then, the sensitivity for a generic source will be studied as a function of its integral flux, spectral index and declination.

6.1 Choice of the optimal event reconstruction

The high–level analysis for ARGO–YBJ is similar to that of other ground –based observatories, consisting in looking for a relatively small excess of events above a uniform background. However, before expressing any result, one must decide how to reconstruct events, what cuts to apply and how to treat the reconstructed data.

In order to apply the criterion of maximizing the sensitivity for the detection of the Crab Nebula it should be noted that:

1. the reconstruction depends mainly on the event multiplicity
2. the first goal of data-analysis is to detect a source with the highest

possible statistical significance

Point (2) implies that the interesting quantity is the integral sensitivity $S(> N_{min})$, i.e. the sensitivity obtained when all the events with $N_{hit} > N_{min}$ are considered. From the physical point of view different multiplicity thresholds correspond to different energies and, due to point (1), to different levels of significance for the source detection.

Given the expected dependence of the results on the multiplicity, data can be treated in two alternative ways.
The first approach (method A) establishes a correspondence between the event multiplicity and the reconstruction chain to be used for its analysis. The optimal analysis is fixed, in this case, independently of the minimum multiplicity used for the computation of integral sensitivity. On the contrary, the second approach (method B) sets a single optimal analysis to be used independently of the event multiplicity. In this case the selected analysis is a function of the minimum multiplicity.
The comparison of reconstruction chains will be carried out in both cases.

6.1.1 Method A

Statistics limit the actual possibility of studying the behaviour of reconstruction for a single multiplicity. Therefore, ten non overlapping bins have been selected to cover the whole multiplicity range of interest, from 20 to 15600 hits (the maximum multiplicity for an ARGO–YBJ event).
The following bins have been considered: $N_{hit} = 20$–50, 50–75, 75–100, 100–150, 150–200, 200–300, 300–400, 400–600, 600–1000, 1000–15600. Denoting the i-th range with $\Delta_i = [N^i_{min}, N^i_{max}]$, the sensitivity in Δ_i is:

$$S(\Delta_i) = \frac{N^i_\gamma \, \xi(\psi^i_b)}{\sqrt{N^i_B \, 2\pi(1 - \cos\psi^i_b)}} \tag{6.1}$$

where N^i_γ and N^i_B are the number of reconstructed γ an background events in the i-th multiplicity range and ψ^i_b is the half opening of the circular angular bin fixed for the analysis in the range Δ_i. Other symbols are the same as Eq.2.2 and ψ^i_b is chosen as explained in Ch.5.
$S(\Delta_i)$ has been computed for all the reconstruction chains by directly integrating equation 2.2 in the case of the Crab Nebula. The full results are plotted in App.B. Then the chain giving the maximum value for $S(\Delta_i)$ is taken as the optimal to analyse events with a multiplicity within Δ_i.

The optimal reconstruction, as determined with this procedure, is summarised in Tab.6.1. The `LLF2` algorithm has been found to give the best results at every multiplicity. As regards the angular reconstruction, results rule out the planar fit: the conical fit with fixed conical parameter is selected up to $N_{hit} = 400$, while at higher multiplicities Conical improves the sensitivity. The most interesting point is the best area cut: the equilibrium point between the reduction of effective area and the improvement in the reconstruction is reached at cut areas decreasing with multiplicity. In particular in the first three bins the best choice is to retain all the internal and external events.

ΔN_{hit}	Core Rec	Dir. Rec	A_{cut}	ψ_b (°)
20-50	`LLF2`	Conical2	no cut	1.54 ± 0.01
50-75				1.10 ± 0.01
75-100				0.83 ± 0.01
100-150			A_4	0.647 ± 0.008
150-200				0.611 ± 0.008
200-300			A_3	0.458 ± 0.009
300-400				0.373 ± 0.009
400-600		Conical		0.329 ± 0.007
600-1000				0.261 ± 0.006
>1000			A_2	0.196 ± 0.004

Table 6.1: *The optimal reconstruction chain as determined with method A. The optimal opening bin in each multiplicity interval is given with statistical errors.*

The integral sensitivity, with a threshold corresponding to the lower limit of each bin, is:

$$S_A(N^i_{min}) = \frac{\sum_{j\geq i} N^j_\gamma \, \xi(\psi^j_b)}{\sqrt{\sum_{j\geq i} N^j_B \, 2\pi(1-\cos\psi^j_b)}} \quad i = 1, ..., 10 \tag{6.2}$$

$S_A(N^i_{min})$ is different from the sum of the $S(\Delta_j)$. Therefore, having maximised the latter quantities does not guarantee that the maximum value for $S(N^i_{min})$ has been taken. On the other hand, this approach should help in reducing the dependence on the multiplicity spectrum of a source since, by definition, the fixed reconstruction is marginally affected by a change in the relative contribution of different multiplicity ranges. In principle this dependence can be further reduced by increasing statistics for MC simulations thus allowing for a choice of smaller multiplicity bins.

6.1.2 Method B

In this second case the calculus of sensitivity is formally the same as for method A, with the difference that for a fixed N_{min} a single bin ranging up to 15600 is opened. Selecting the same ten thresholds as in case A:

$$S_B(N^i_{min}) = \frac{N'^i_\gamma \, \xi(\psi'^i_b)}{\sqrt{N'^i_B \, 2\pi(1 - \cos\psi'^i_b)}} \quad i = 1, ..., 10 \tag{6.3}$$

where N'^i_γ,N'^i_B,ψ'^i_b refer to the whole range $[N_{min}, 15600]$. The main difference with respect to method A is that a single angular bin is used, regardless of multiplicity, and that all the events are analysed with the same algorithms and cuts.
The optimal reconstruction, defined as the chain that maximizes $S_B(N^i_{min})$, is selected as a function of N^i_{min}. The full comparison of reconstruction chains is given in App.B, while the final results are summarized in Tab.6.2.

ΔN_{hit}	Core Rec	Dir. Rec	A_{cut}	ψ_b (°)
>20			no cut	0.901 ± 0.005
>50		Conical2		0.674 ± 0.004
>75			A_4	0.559 ± 0.004
>100				0.519 ± 0.003
>150	LLF2			0.368 ± 0.004
>200				0.339 ± 0.004
>300		Conical	A_3	0.265 ± 0.003
>400				0.252 ± 0.003
>600				0.219 ± 0.003
>1000			A_2	0.196 ± 0.004

Table 6.2: *Optimal reconstruction chain obtained with the application of method B. The optimal opening bin is given at each multiplicity threshold with statistical errors.*

In this case the selection criterion maximises the integral sensitivity.
Another difference between the two methods is in the multiplicity of reconstructed events. Consider for example the signal showers selected at

$N_{hit} > 600$. Since $\psi_b'^9 < \psi_b^9$ (and the other elements of the reconstruction are the same), method B selects less events than method A in $\Delta_9 = [600, 1000]$. At the same time method B makes use of a larger area cut for $N_{hit} > 1000$ therefore a higher average multiplicity results at threshold > 600 with respect to method A. A similar effect occurs at every multiplicity.
Note that the selected algorithms and cuts look very similar to those determined previously[1]. Here, however, the changes from one to another occur at lower multiplicity due to the contribution of high multiplicities.

6.1.3 Results

Values obtained for the integral sensitivity to the Crab Nebula are shown with statistical errors in Fig.6.1 versus the multiplicity threshold. They refer to one year of data taking. The optimal analysis, as determined with method A (left plot, yellow) and method B (right blue), lead to a similar behaviour of the sensitivity: it increases as the reconstruction improves up to a maximum value at threshold 100, then decreases again due to the falling rates of signal events.
The difference in their absolute values is due to the fact that S_B is maximised by definition whereas S_A is not.

Results obtained by using non-optimised analysis chains are shown for comparison. The angular bin has been fixed in the same fashion as in the optimized case (as a function of the multiplicity bin on the left and as a single bin for the whole range $N_{hit} > N_{min}$ on the right) so that the three curves in each plot can be directly compared.
The case of planar fit with no cuts represents the minimal analysis chain that can be used and the fastest one since no core reconstruction is required. In this case the behaviour is completely dominated by the falling rates. Nevertheless, the sensitivity is above the level of 5 standard deviations (σ) per year up to $N_{hit} > 100$.
The red curve allows to quantify the increase of sensitivity achieved with a more appropriate description of the shower front, even if the less performing core reconstruction (`Centre`) is used.
Finally, the differences among optimized and non–optimized results give a quantitative evaluation of the remarkable improvement obtained with a

[1] In any case they cannot be directly compared since they refer to different multiplicity ranges

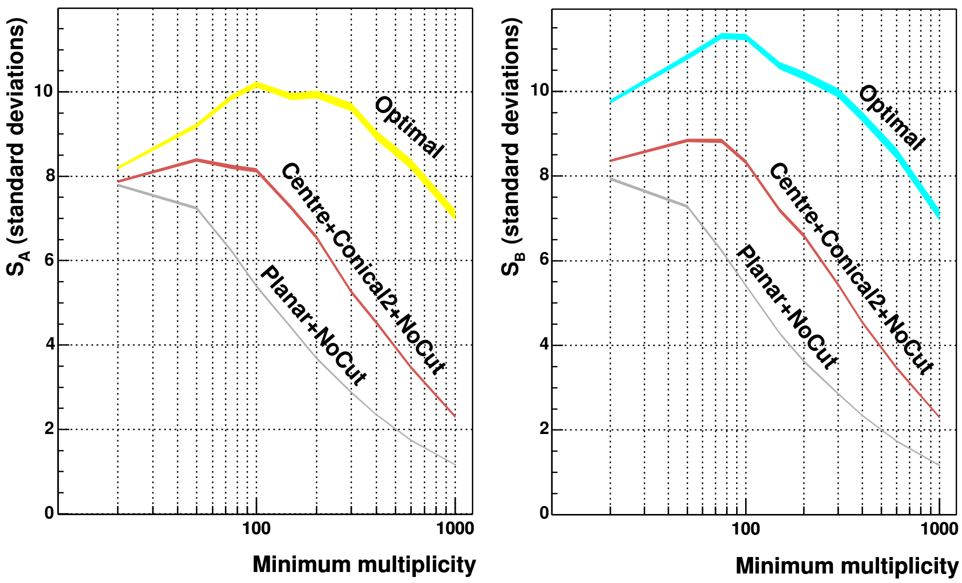

Figure 6.1: *Integral sensitivity per year to the Crab Nebula as a function of the multiplicity. Left and right plots show the result obtained by using the analysis optimized with method A and method B respectively, compared with two non-optimized analyses. Statistical errors are shown.*

proper choice of the event analysis, in particular at high values of N_{min}.

Results obtained by using the reconstruction chains and the angular bins optimized as described above, will be referred to as "method A" and "method B" in the following sections.

6.2 Sensitivity to the Crab Nebula

The information about the significance level expected for the Crab detection is incomplete from the point of view of physics. First of all uncertainties other than statistical have to be considered, secondly the multiplicity threshold has to be converted into a physically meaningful quantity.

In order to evaluate the maximum variation of the expected sensitivity, uncertainties in the knowledge of spectra ofr the source and of the CR background will be considered.

The Whipple measurement of the Crab differential flux [12], expressed in $\mathrm{m}^{-2}\ \mathrm{s}^{-1}\ \mathrm{TeV}^{-1}$, is

$$\frac{dn}{dE} = 3.20 \pm 0.17 \pm 0.6\ \times\ 10^{-7} \left(\frac{E}{1TeV}\right)^{-2.49 \pm 0.06 \pm 0.04} \tag{6.4}$$

where the the quoted uncertainties reflect, first, statistical errors and second, systematic uncertainties.
Systematic errors give a contribution of about 18% that will be reflected on sensitivity[2].

As regards the background the error quoted in [57] (already shown in Tab.3.3) will be considered.
In both cases uncertainties cannot be analytically propagated since a change of the source spectral slope affects the sensitivity indirectly through a change of the multiplicity spectrum. The same problem holds for background.
Therefore, errors have been evaluated by reintegrating the sensitivity formula at the upper and lower limit of each parameter (spectral slope and normalization). The maximum uncertainty has been evaluated as the sum of these variations.

Results are shown in Fig.6.2 in the case of method A and method B. Filled areas (yellow and light blue) represent the maximum error in the estimate. It can be seen that the background contribution is of the order of 5-8%. Statistical, shown by the central line, are related to the number of generated MC events and affect the estimate to a minor extent. The most important source of uncertainty is the source flux (dashed areas), whose contribution is mainly due to statistical errors in the flux normalization.
In the worst case the expected sensitivity is of about 7σ/year and 8σ/year respectively at multiplicities > 100.

With regard to the meaning of multiplicity threshold, it has to be converted into energy. The threshold energy for the detection of a source can be defined in several ways. Here, the median energy of the signal events retained after the analysis will be used to indicate the energy range over which the detector is sensitive.
Values of the median energy are given in Tab.6.3 as a function of minimum multiplicity for method A, method B and in the case of triggering events (for comparison). Errors are due to the uncertainty in the source spectral

[2] Given a source with a differential spectrum $kE^{-\beta}$, k appears as a multiplicative factor in the sensitivity.

slope only.

Median energy (TeV)			
N_{min}	Trigger	Method A	Method B
>20	0.93±0.14	0.80±0.06	1.50±0.14
>50	1.4±0.2	1.13±0.09	1.9±0.2
>75	1.9±0.2	1.46±0.08	2.3±0.2
>100	2.3±0.2	1.69±0.09	2.8±0.2
>150	3.1±0.3	2.2±0.1	3.6±0.2
>200	3.7±0.3	2.7±0.1	4.4±0.2
>300	4.8±0.3	3.6±0.2	5.6±0.2
>400	5.9±0.3	4.7±0.2	6.5±0.3
>600	7.7±0.3	6.6±0.3	8.0±0.3
>1000	10.7±0.3	10.0±0.4	10.0±0.4

Table 6.3: *Median energy of events from the Crab Nebula at different multiplicity thresholds. Results are listed in the case of no analysis (trigger), method A and method B.*

The value of the median energy (E_m) represents the most important difference between method A and method B. For a fixed N_{min}, the latter method gives higher sensitivity but the median energy of the detection moves upward with respect to method A. An interesting result is that method A lowers the trigger median energy. This is due to the rejection of external showers by means of the area cut.

The maximum values of the sensitivity to the Crab Nebula are, in summary:

- $S_A = 10.3 \pm 28\%$ σ/y at $E_m \simeq 1.7$ TeV (method A)
- $S_B = 11.3 \pm 29\%$ σ/y at $E_m \simeq 2.8$ TeV (method B)

The central values correspond to $\simeq 2.8$ months and $\simeq 2.3$ months of data taking required to achieve a 5σ significance level.
For comparison, the Milagro observation of the Crab Nebula was performed at a 6.4 σ level[3] in 917 days of running [38] corresponding to 4.0 σ/y.

[3]The Milagro detection makes use of a background rejection technique without which

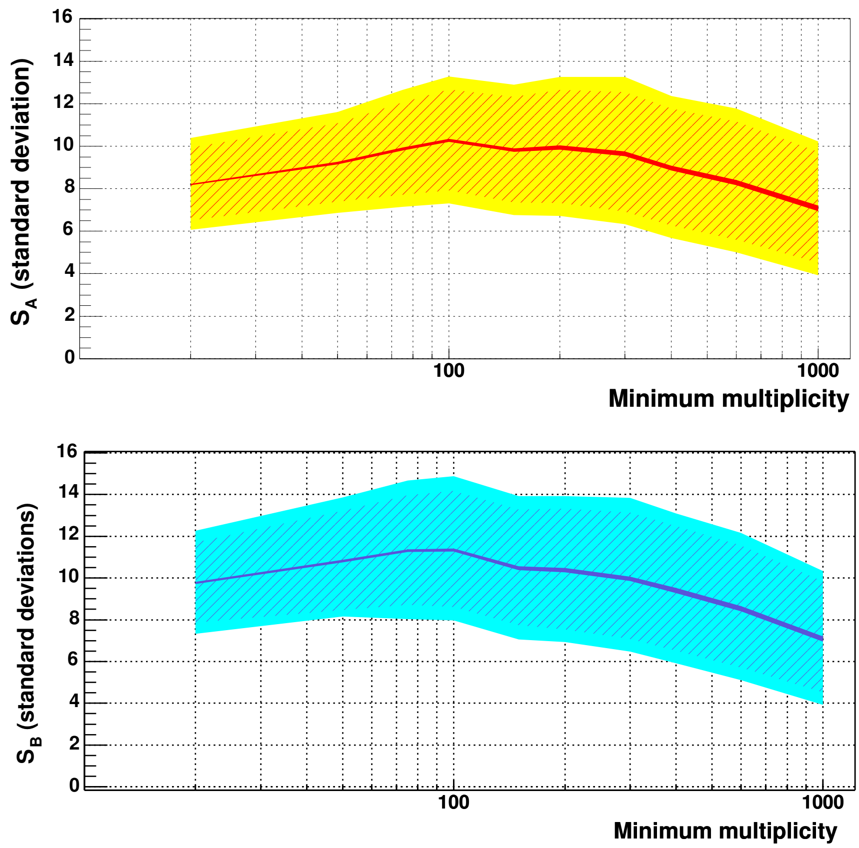

Figure 6.2: *Sensitivity to the Crab Nebula in 1 year computed with method A (upper plot) and method B (bottom). The central line of each plot (respectively red and dark blue) represent the statistical errors of the estimate. Dashed areas represent the contribution of the uncertainties on the Crab flux, while light filled areas show the total error due to statistics and to uncertainties in both source and background fluxes.*

If confirmed by real data analysis, the ARGO–YBJ sensitivity seems excellent. The present estimate is even more impressive since no background rejection has been yet used. The median energy of maximum sensitivity configurations is much lower than current operating EAS. Moreover, selecting method A at $N_{hit} > 20$ allows for a detection of the Crab Nebula with a sensitivity of at least 6 σ/y and a median energy of $\sim$800 GeV.

The reliability of these evaluations should be assured by the method used to simulate MC showers: no *a priori* hypothesis on reconstruction performances has been made, all the known effects of the detector have been taken into account and particular attention has been paid to avoid systematic errors.

6.3 Sensitivity to a generic point source.

The sensitivity to the Crab Nebula indicates that ARGO–YBJ is capable to achieve both a low energy threshold and a good sensitivity. However, since the reconstruction has been calibrated for the Crab detection, an important point is to understand how the sensitivity changes when other sources are observed.

6.3.1 Dependence on the integral flux and spectral index

Here a source characterised by a power law differential spectrum $kE^{-\beta}$ will be considered. The detection performances of the ARGO–YBJ experiment will be discussed varying k and β while keeping the source position fixed at the Crab celestial coordinates. It will be assumed that the spectrum of the source extends up to 30 TeV.

Six values of the spectral index β have been considered, ranging from 2.0 to 3.0. In order to simultaneously study the effects related to k, the minimum detectable flux (MDF) will be shown instead of sensitivity.
MDF is defined here as the minimum integral flux above the median energy

the sensitivity in 917 days was 1.9 σ (equivalent to 1.2 σ/y). The median energy for the Crab detection is not given in [38]: 4 TeV is the median energy estimated for vertical showers.

required to detect a source at a level of 5 σ/y. For each value of β the proper weight has been used to reproduce its energy distribution. Then the sensitivity S^0 (per year) has been computed in the case $k = 1$ (arbitrarily chosen), and the median energy has been determined (E_m is independent of k). Defining

$$\Phi(> E_m) = \int_{E_m}^{30TeV} E^{-\beta}\, dE \tag{6.5}$$

the MDF is given by

$$MDF = \frac{5}{S^0}\, \Phi(> E_m) \tag{6.6}$$

30 TeV is the maximum energy used to generate MC γ showers (see Ch.3). The MDF has been evaluated with method A (Fig.6.3) and with method B (Fig.6.4). In both cases each line refers to a fixed spectral index. The ten points at increasing energy correspond (in increasing order) to the minimum multiplicities N^i_{min} defined above. The integral Crab flux is plotted for comparison, assuming that it extends up to 30 TeV for consistency.
These plots allow to estimate the sensitivity to a source with an integral flux of 1 Crab Unit (CU). The ratio of MDF to the Crab flux at the same energy gives a measurement in Crab Units of the MDF, which has to be multiplied by 5 σ to get the sensitivity corresponding to a flux of 1 CU.

Fig.6.3 and Fig.6.4 also show that the median energy dramatically depends on the spectral index. Consider, for example, the first points of the 6 curves in Fig.6.3. Even if the event analysis is identical, the median energy gradually decreases from $\sim$ 1.3 TeV to less than 500 GeV. A similar effect can be seen at every multiplicity threshold.
The second result is that the ratio of MDF to the Crab flux lowers with increasing β. Therefore, ARGO–YBJ is more sensitive to sources with soft spectra and in this case the median energy can be very low[4].
A similar behaviour can be seen in Fig.6.4. Here, however, the median energies are always higher and the dependence of the sensitivity on the index is more relevant with respect to method A. These differences confirm what has been said in the case of the Crab Nebula.

[4]The dependence on source properties clearly shows that giving a sensitivity level or a median energy without specifying the source is meaningless.

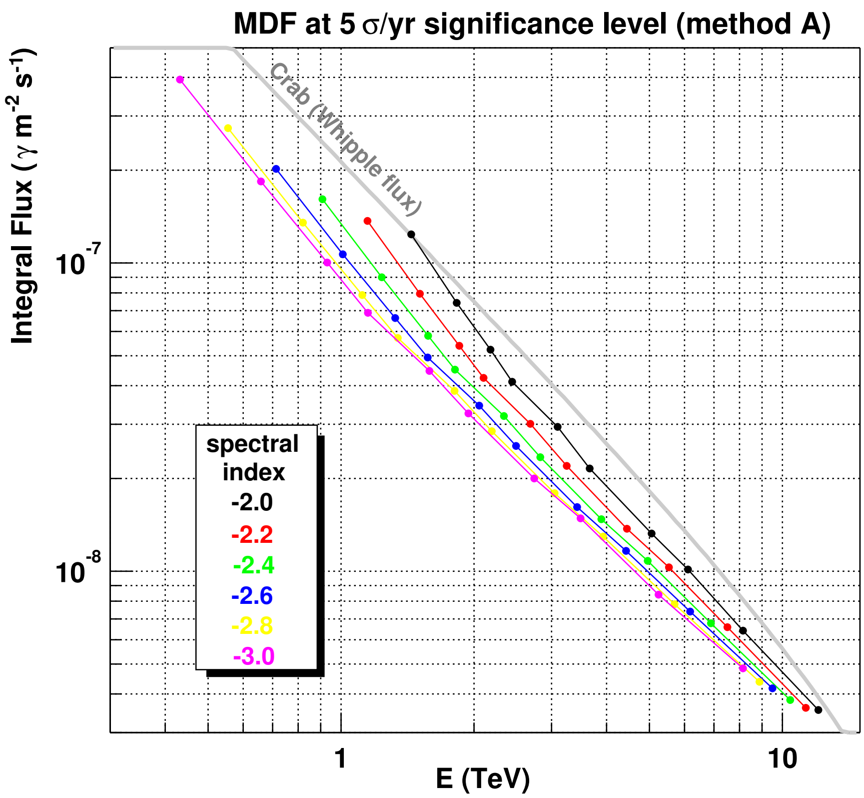

Figure 6.3: *Minimum detectable flux as a function of the median energy of the detection. Points correspond to the optimized analysis (method A) at the ten multiplicity thresholds considered here (see text). The Crab Nebula integral flux is plotted for comparison.*

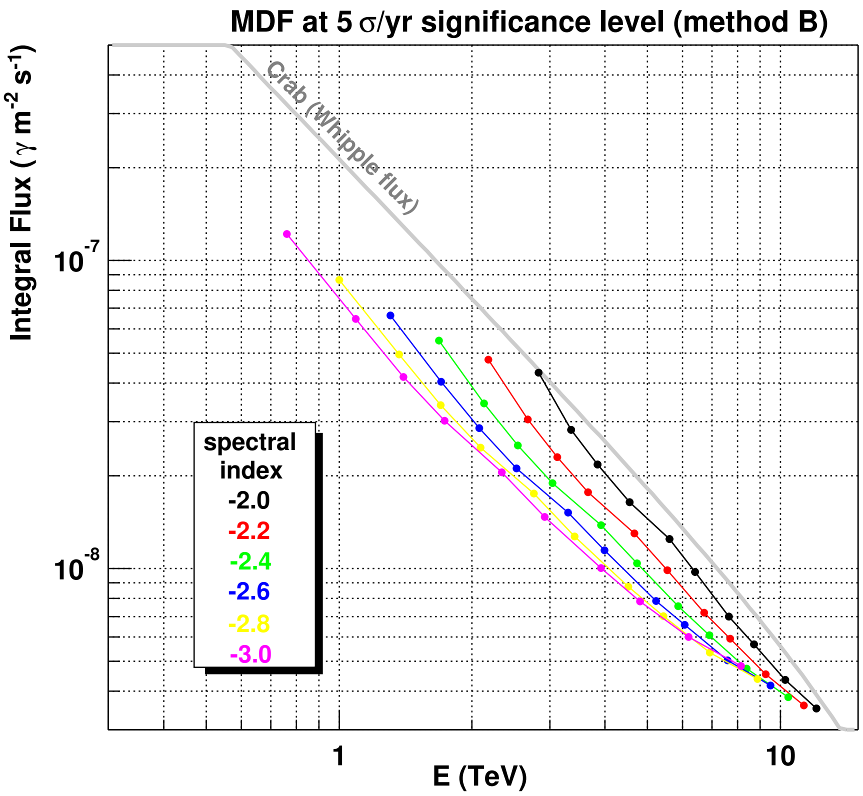

Figure 6.4: *Minimum detectable flux as a function of the median energy. This plot is the analogous of Fig.6.3 in the case of method B.*

6.3.2 Dependence on the source declination.

The other property of the source that explicitly appears in the expression of sensitivity is its motion in the YBJ local sky. As explained in Ch.2 and Ch.3, only the dependence on θ is relevant. Therefore, the sensitivity will be studied as a function of the source declination δ. A Crab–like flux is assumed.

The sensitivity has been computed here at 9 declinations ranging form $15°$ to $55°$ North approximately corresponding to the portion of the sky that is visible at YBJ above $\theta = 30°$ for at least 3 hours per day. The range is asymmetric with respect to the YBJ latitude. The point at $\delta = 30°$ is the nearest to the detector latitude and corresponds to a source that culminates at $\theta_{min} \sim 0.2°$.

The sensitivity is shown versus the source declination in Fig.6.5 (method A) and Fig.6.6 (method B).
The dashed lines have been computed by scaling the maximum value ($N_{hit} > 100$ at $\delta = 30°$) with the square root of the relative reduction of exposure time. It represents the dependence that should be observed if the sensitivity were dependent on declination through the exposure time only. The behaviour of the computed points is significantly different, with a steeper decrease. Indeed a higher average zenith angle implies smaller effective areas and a larger contribution of the $\cos\theta$ geometrical factor both for signal and background. Since the denominator of sensitivity is the square root of the background integral, the signal to noise ratio degrades as the source moves to large zenith.
A proper quantitative evaluation of sensitivity reduction has required again the integration of Eq.2.2.

The second effect of atmospheric absorption is an increase of the median energy with declination due to the thicker layer of atmosphere traversed by source events. Fig.6.7 shows that this effect is relatively limited.
The major effect of declination is a change in the detection significance level. As for the spectrum, also the declination has to be specified to allow for a reliable prediction of the detector capabilities.

Finally, the ARGO–YBJ maximum sensitivity map has been filled. A third degree polynomial has been used to fit points computed with Method B at $N_{min} > 100$.

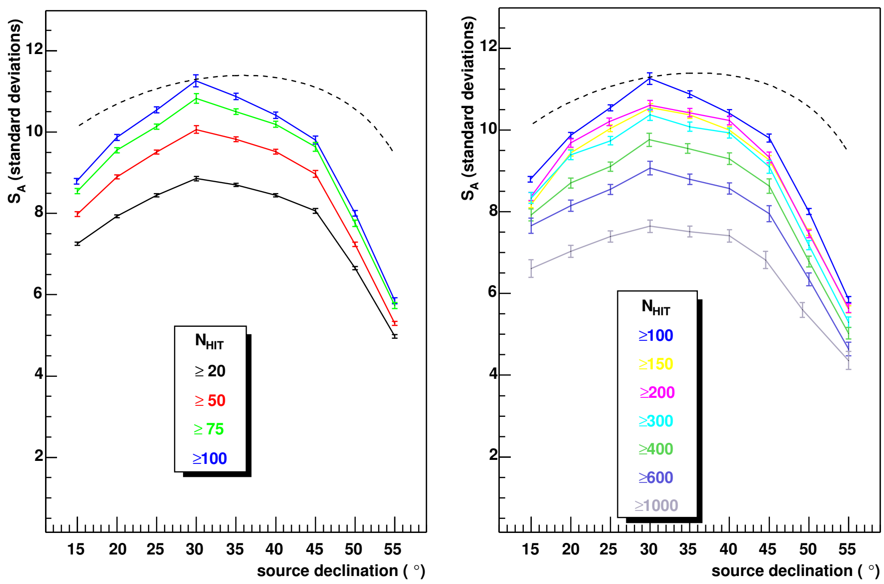

Figure 6.5: *Sensitivity to a Crab–like source computed with method A as a function of the source declination. Each set of points refer to a given minimum multiplicity. The dashed line shows the peack value scaled with the squared root of the time during wich the source is visible above* 30°

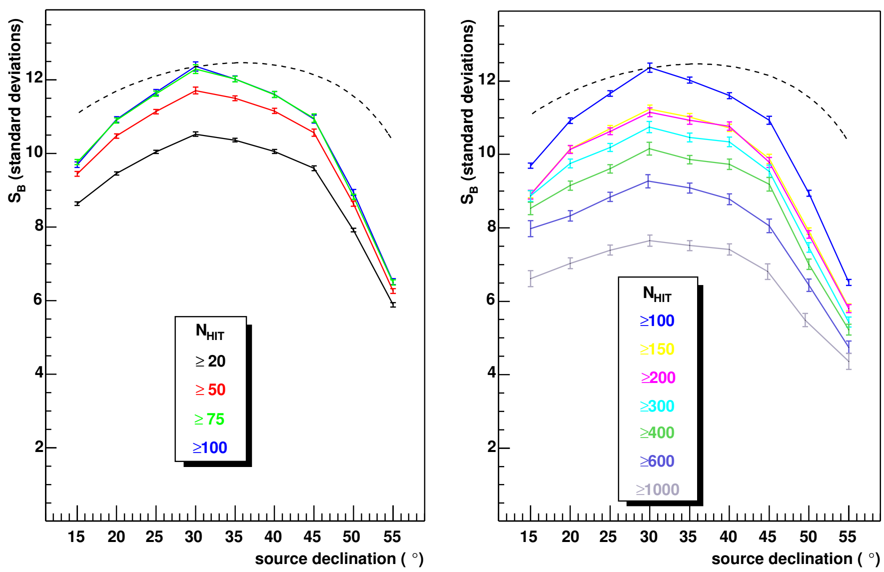

Figure 6.6: *Sensitivity to a Crab–like source computed with method B as a function of the source declination (analogous to Fig.6.5)*

The map is shown in galactic coordinates in Fig.6.8 and refers to a median energy is of about 3 TeV for a Crab—like source with an integral flux equal to 1 Crab Unit. It shows that a large fraction of the overhead sky can be monitored at high sensitivity ($> 10\sigma$/y). thus allowing for the search for continuous and episodic sources of VHE gamma ray sources.

Of course the validity of the map is limited to sources with a spectral index 2.49. The dependence on the actual slope can be extrapolated from the results of the previous section.

The discussion about the sensitivity to a point source has shown that a meaningful estimate requires the knowledge of source position and spectrum. However the following important results hold:

- in a wide range of declination a Crab–like source can be detected with a sensitivity comparable or even better than the sensitivity estimated for the Crab Nebula
- an increase of sensitivity and a decrease of the median energy is expected for sources with a steeper spectrum with respect to the Crab case
- harder spectra (at least up to $\beta = 2$) should be detected at a significance level higher than 5σ/y

Moreover, once that a source has been located, the energy interval of the detection and the significance level can be selected to a certain degree by choosing the more appropriate analysis and multiplicity threshold.

Results presented in this thesis, obtained without any gamma/hadron discrimination, show that the simple pointing of the source makes ARGO–YBJ competitive with current detectors. A further increase of the sensitivity is expected thanks to rejection of background events. The granularity of the detector can be used to separate background from gamma ray showers by making use of the different pattern of the shower front particles. Preliminary results are very promising and detailed studies are in progress.

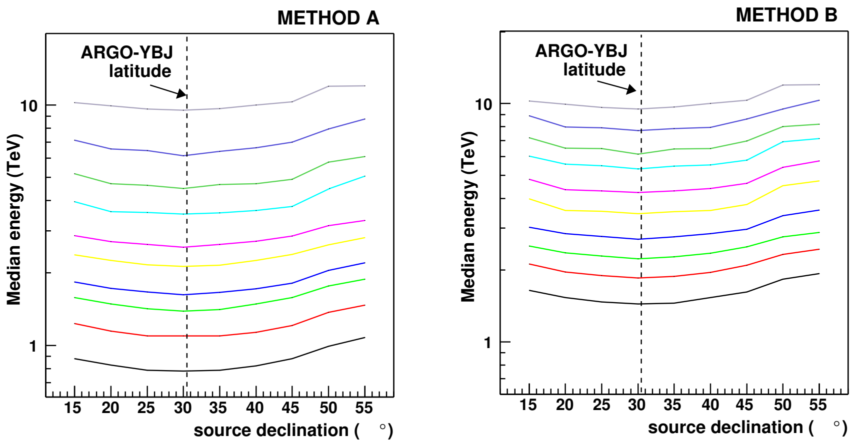

Figure 6.7: *Median energy as a function of the source declination. The same colors as in Fig.6.5 and Fig.6.6 have been used. Left and right plot have been obtained by using respectively method A and method B.*

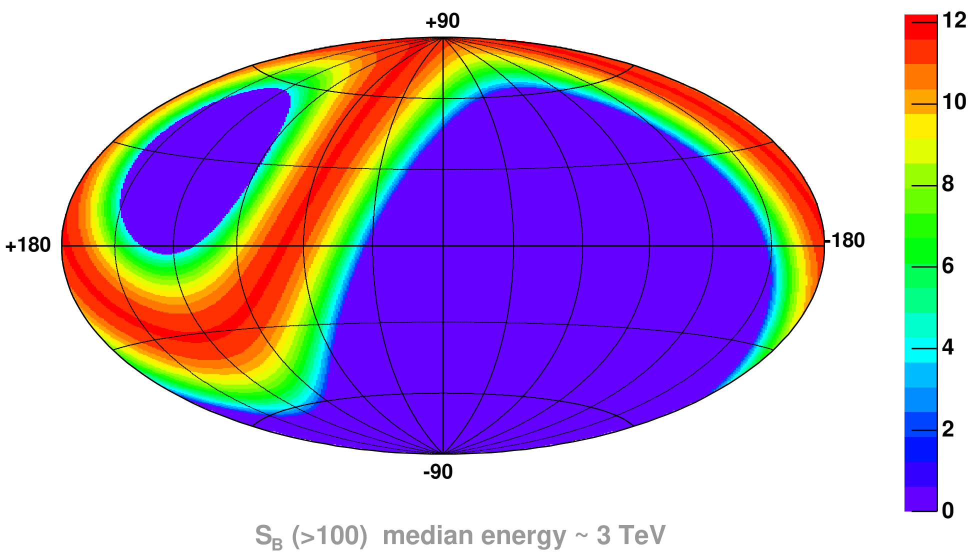

Figure 6.8: *ARGO–YBJ sensitivity sky map in galactic coordinates. The significance for the detection in 1 year of a Crab–like source has been estimated by means of method B at multiplicity >100. This corresponds to a median energy of about 3 TeV (see Fig.6.7)*

Appendix A

MC simulations and effective areas.

A.1 Tables of generation areas and numbers of simulated events.

As discussed in Ch.3 MC showers have been generated with their core positions distributed over square areas with half side L_{max} whose values are listed in Tab.A.1 for different primaries and energy ranges. The same values have been used both for the zenith range $0° - 15°$ and for $15° - 30°$

L_{max} (m)			
ΔE (TeV)	γ	p	He
0.01-0.03	150	-	-
0.03-0.1	150	500	-
0.1-0.3	150	300	-
0.3-1	200	300	-
1-3	300	300	500
3-10	400	400	600
10-30	500	500	700
30-100	700	700	900

Table A.1: *Values of L_{max}.*

Tab.A.2 and Tab.A.3 give the total number of generated MC showers for γ-rays, protons and helium nuclei.

$\Delta E\,(TeV)$	γ	p	He
0.01-0.03	40,000,000	-	-
0.03-0.1	2,400,000	15,300,000	-
0.1-0.3	400,000	1,662,580	-
0.3-1	180,000	196,929	-
1-3	54,000	32,517	240,000
3-10	24,000	35,634	60,000
10-30	9,300	12,000	6,000
30-100	-	9,600	1,500
TOTAL	43,067,300	17,249,260	307,500

Table A.2: *Total number of generated events in the zenith range* $0° - 15°$*.*

$\Delta E\,(TeV)$	γ	p	He
0.03-0.1	6,000,000	-	-
0.1-0.3	2,000,000	285,993	-
0.3-1	1,503,000	104,472	-
1-3	1,614,000	95,331	300,000
3-10	192,000	107,472	45,000
10-30	33,000	30,000	3,000
30-100	-	9,000	1,500
TOTAL	11,342,000	632,268	349,500

Table A.3: *Total number of generated events in the zenith range* $15° - 30°$*.*

A.2 Effective area.

Making use of the simulated showers, the effective area for triggering events has been computed. Results are shown in Fig.A.1 for γ–rays and Fig.A.2 for protons and helium nuclei. Events have been weighted in order to reproduce a distribution uniform in energy and in zenith. Therefore, each plotted point represents an unweighted (in the sense of referring to uniform distributions) average over the corresponding energy bin and zenith range. The effective area, as defined in Ch.2, does not include the geometrical factor $\cos\theta$ hence its reduction with increasing θ is due to the increasing effect of atmospheric absorption only.

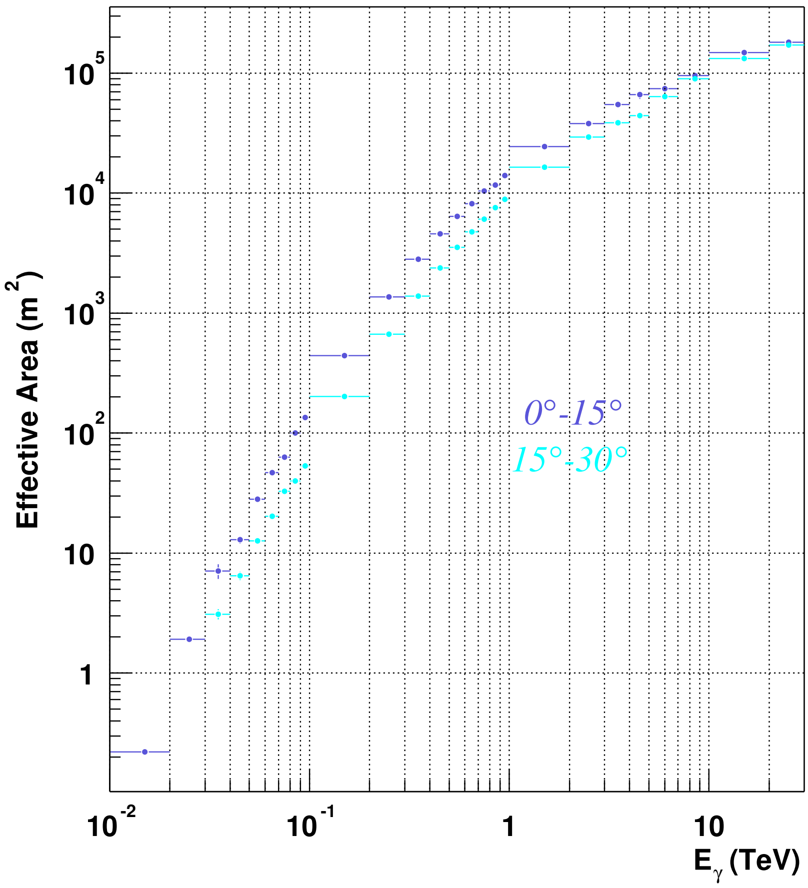

Figure A.1: *Effective area for γ-induced triggering events as a function of the energy of the primary particle. The average over the zenith angle has been computed in two broad zenith ranges.*

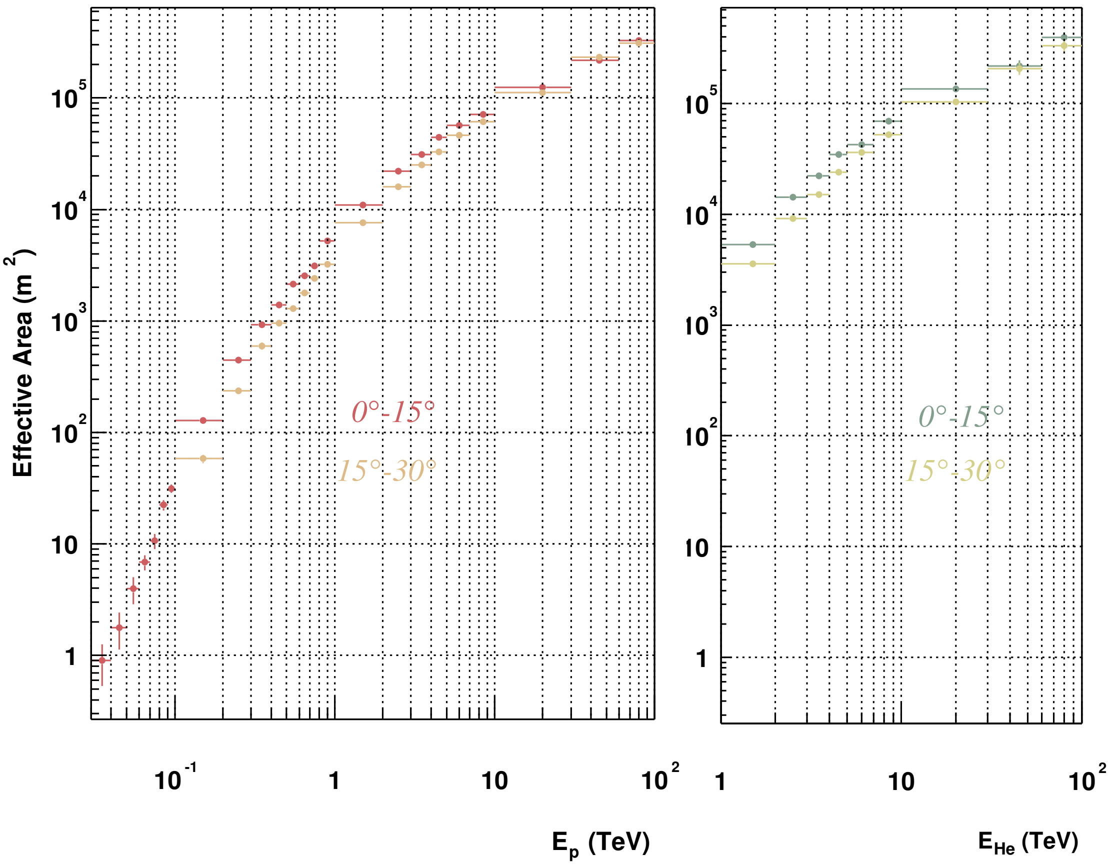

Figure A.2: *Effective area for protons (left) and helium nuclei (right) plotted versus the energy of the primary particle. The two set of points in each plot refer to the average over the corresponding θ range.*

Appendix B

Comparison of the reconstruction chains.

This appendix contains the sensitivity values resulting from a Monte Carlo integration of Eq.2.2. All the possible combinations of reconstruction algorithms and cuts have been considered.

Plots from Fig.B.1 to Fig.B.10 show the values of $S(\Delta N_{hit})$ computed in ten non overlapping multiplicity ranges. This comparison is used to set the optimal reconstruction with method A (see Ch.6).
The next figures refer to multiplicity ranges $[N_{min}, 15600]$ with varying N_{min}. They are used to set the optimal analysis according to method B.

In both cases each figure refers to a fixed multiplicity range. In each of the four plots (all in the same scale) a different core reconstruction algorithm has been used, as indicated by the plot title.
Each plot shows the sensitivity as a function of the area cut: the first four points refer respectively to A_1, A_2, A_3, A_4 (defined in Tab.4.3), whereas the last point represents the result obtained when no area cut is applied.
Black points have been computed by making use of the Planar fit, blue squares with Conical fit, red triangles with Conical2 fit.
A green circle marks the best configuration defined as the reconstruction chain that maximizes $S_A(\Delta N_{hit})$ or $S_B(> \Delta N_{hit})$. The subscript has been used to distinguish the two groups of plots, but the calculation has been done in the same way.

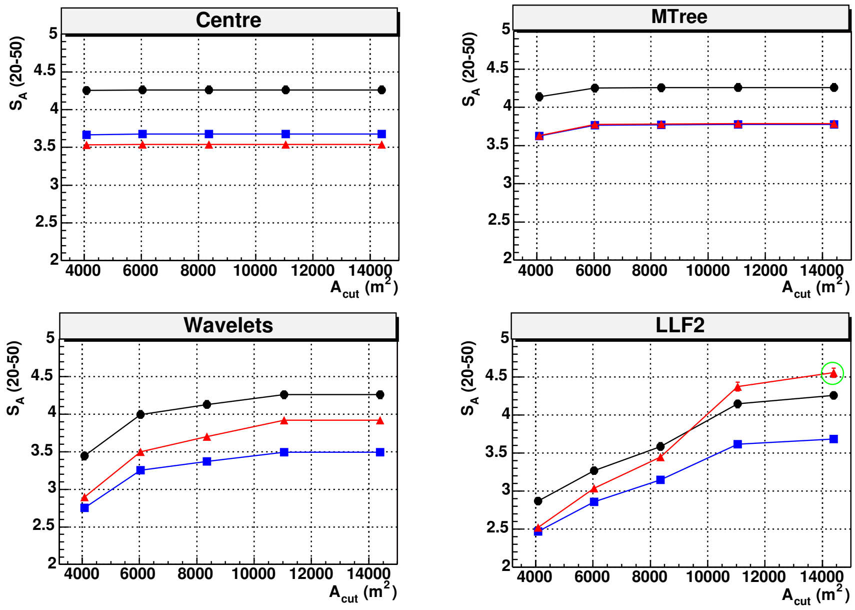

Figure B.1: *Sensitivity (method A) in the multiplicity range 20-50.*

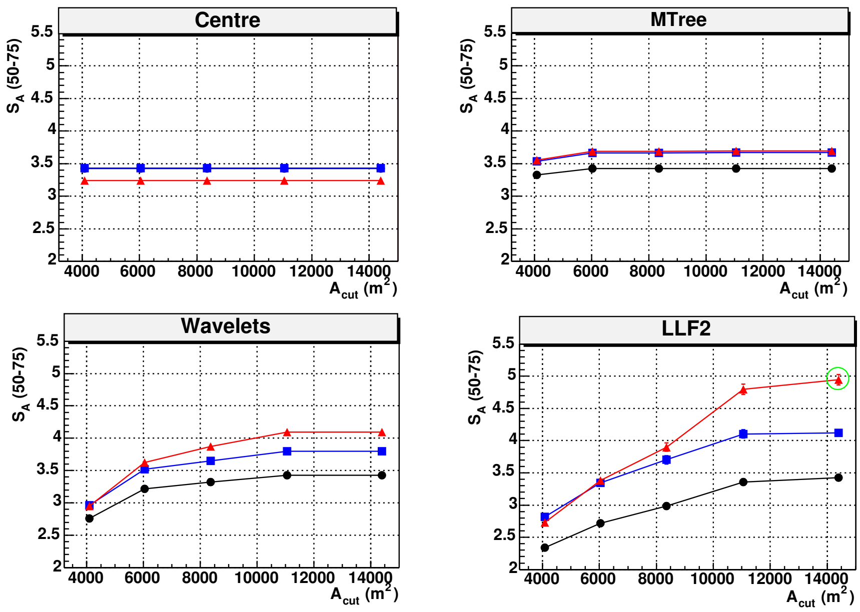

Figure B.2: *Sensitivity (method A) in the multiplicity range 50-75.*

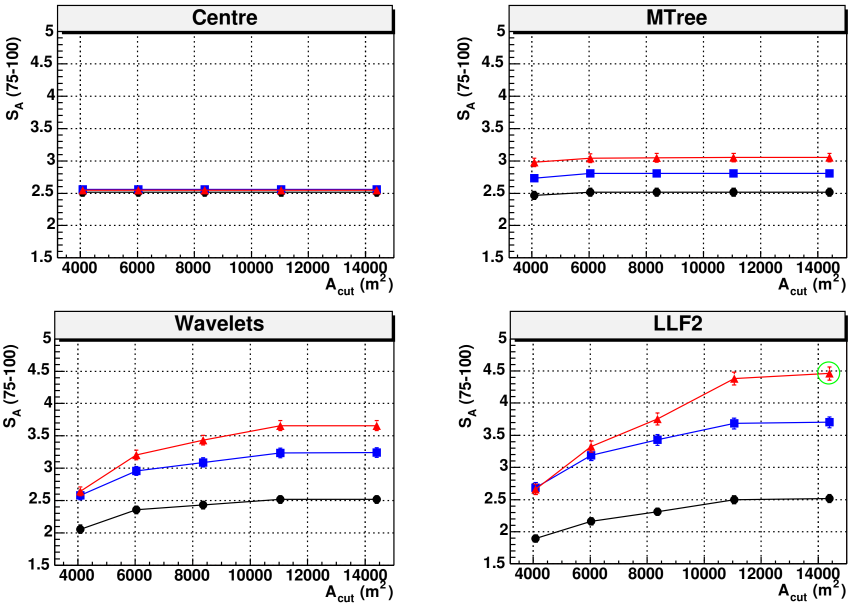

Figure B.3: *Sensitivity (method A) in the multiplicity range 75-100.*

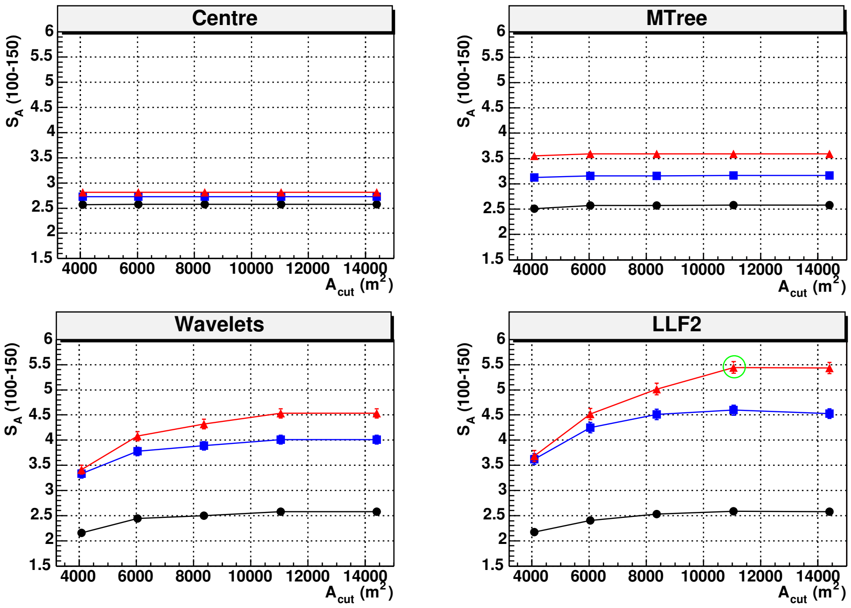

Figure B.4: *Sensitivity (method A) in the multiplicity range 100-150.*

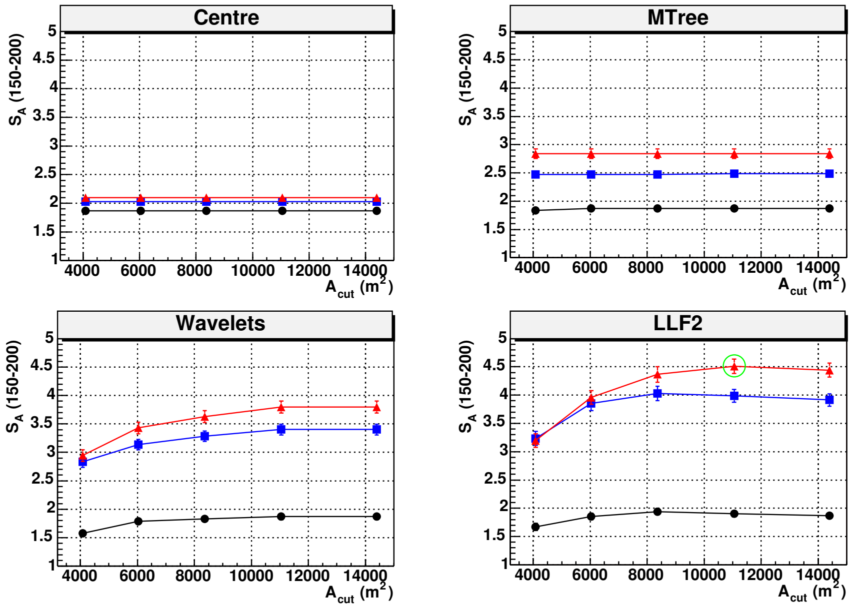

Figure B.5: *Sensitivity (method A) in the multiplicity range 150-200.*

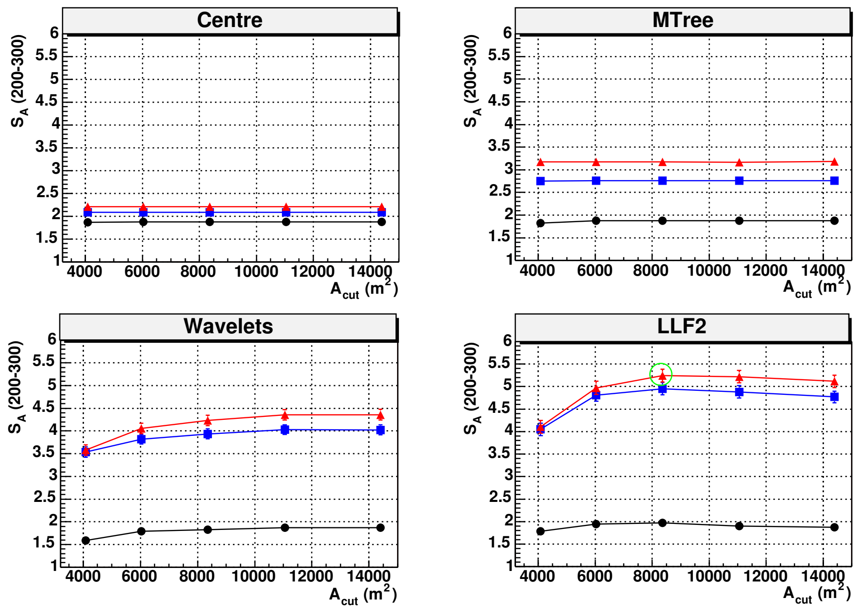

Figure B.6: *Sensitivity (method A) in the multiplicity range 200-300.*

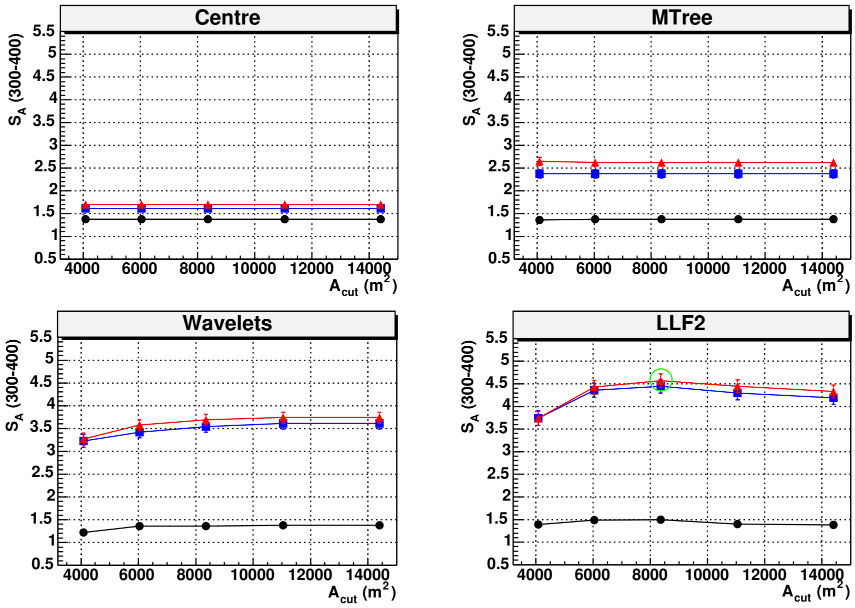

Figure B.7: *Sensitivity (method A) in the multiplicity range 300-400.*

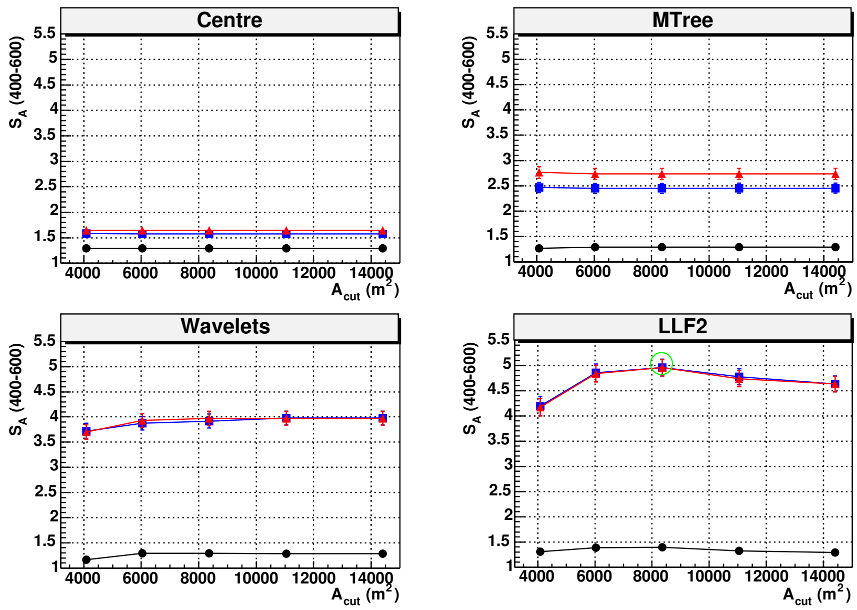

Figure B.8: *Sensitivity (method A) in the multiplicity range 400-600.*

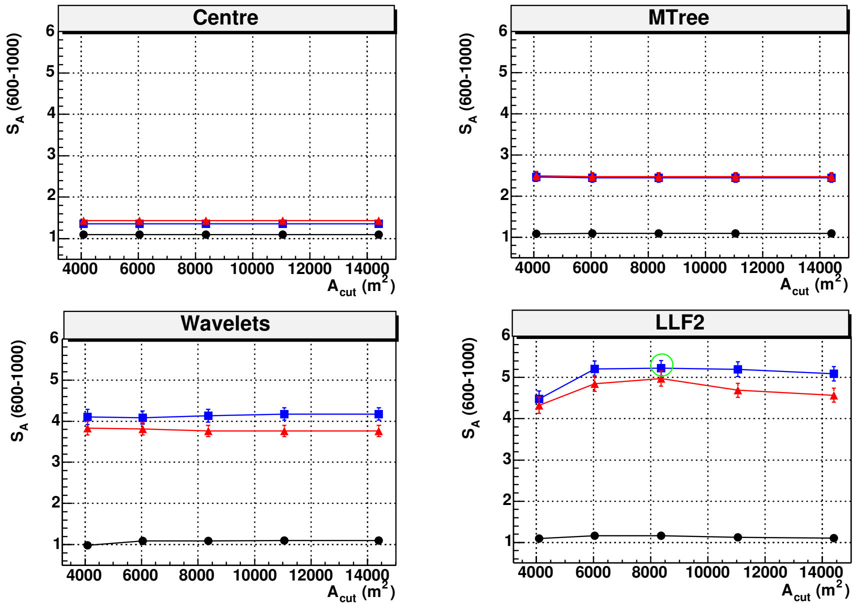

Figure B.9: *Sensitivity (method A) in the multiplicity range 600-1000.*

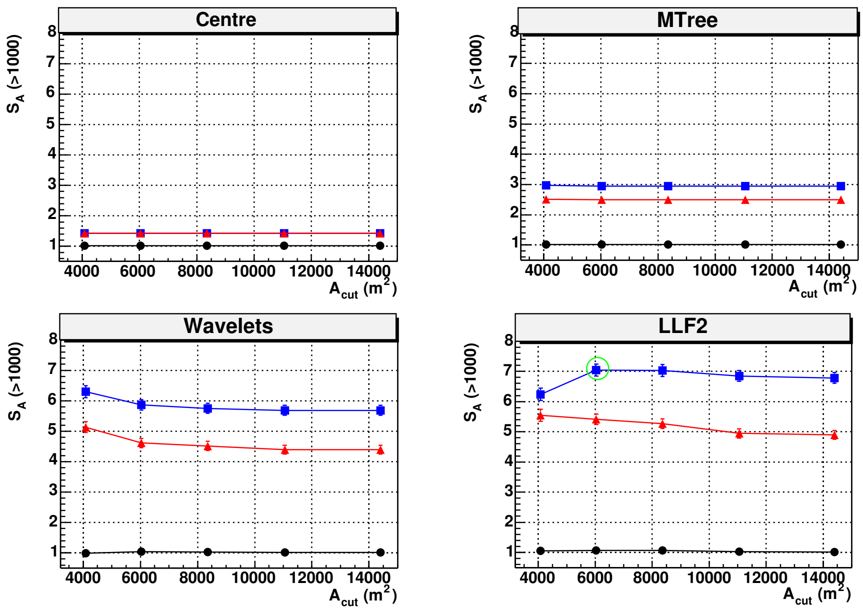

Figure B.10: *Sensitivity (method A) in the multiplicity range >1000.*

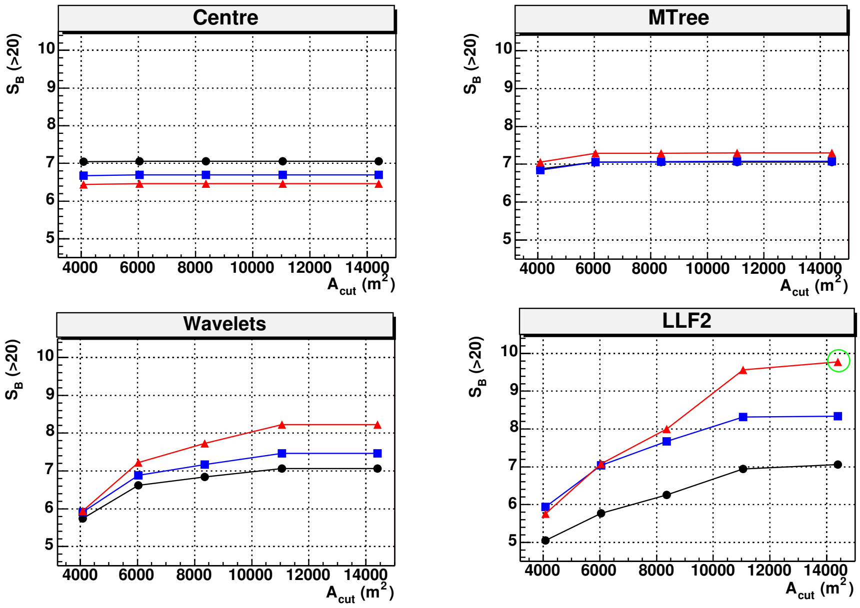

Figure B.11: *Sensitivity (method B) in the multiplicity range >20.*

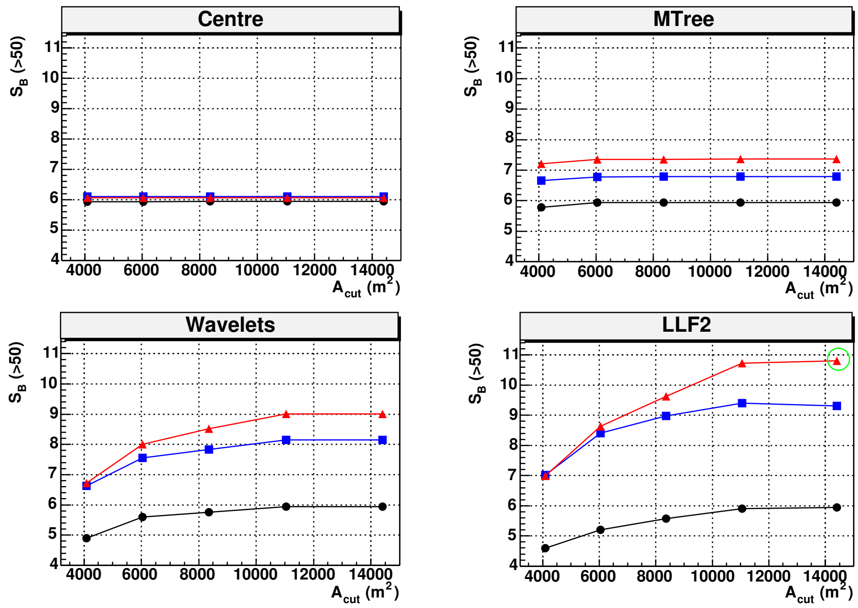

Figure B.12: *Sensitivity (method B) in the multiplicity range >50.*

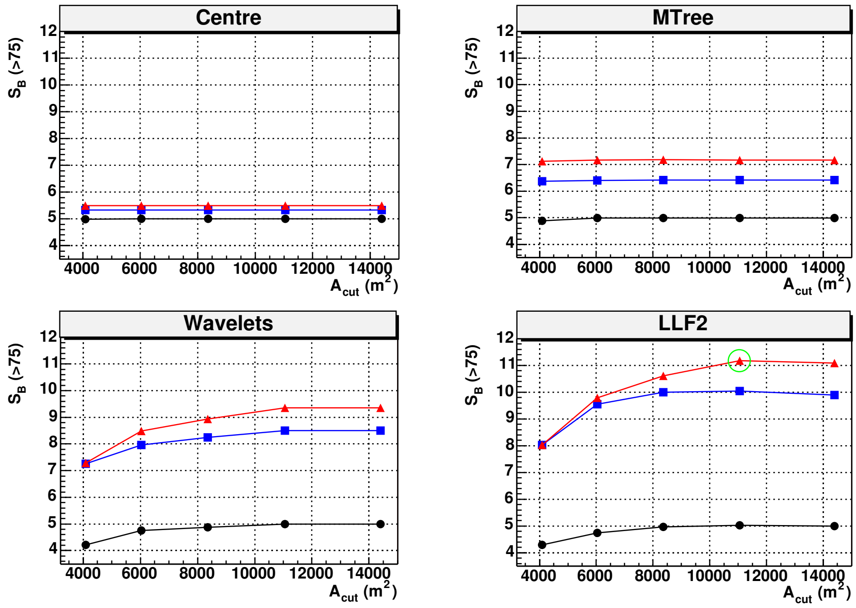

Figure B.13: *Sensitivity (method B) in the multiplicity range >75.*

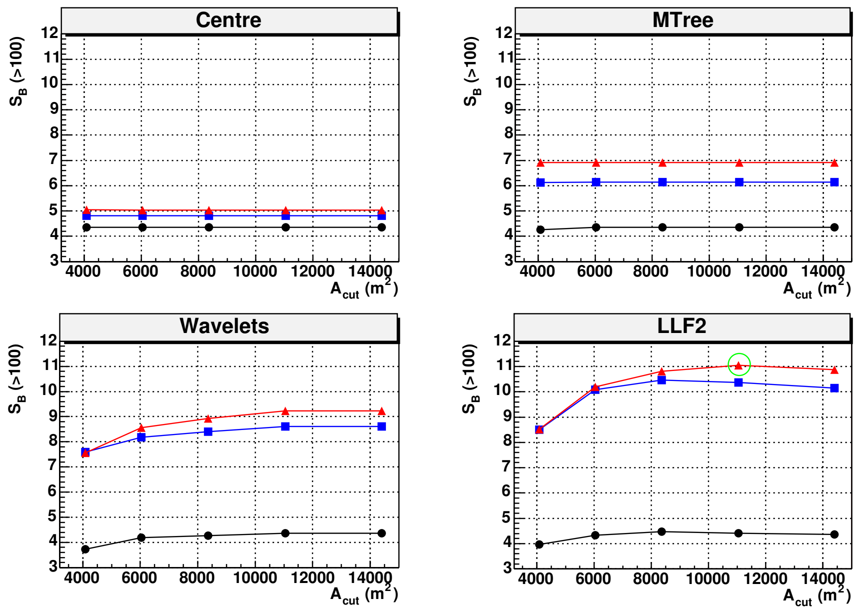

Figure B.14: *Sensitivity (method B) in the multiplicity range >100.*

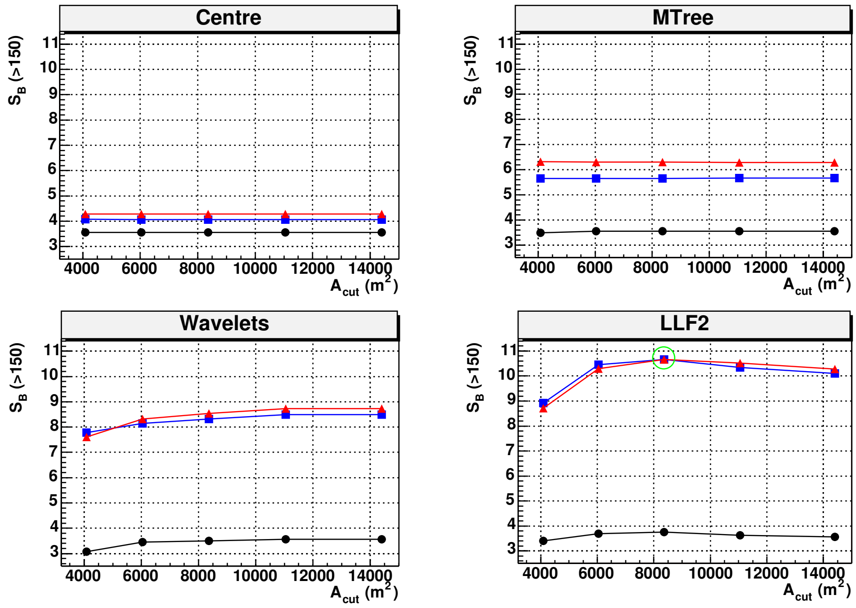

Figure B.15: *Sensitivity (method B) in the multiplicity range >150.*

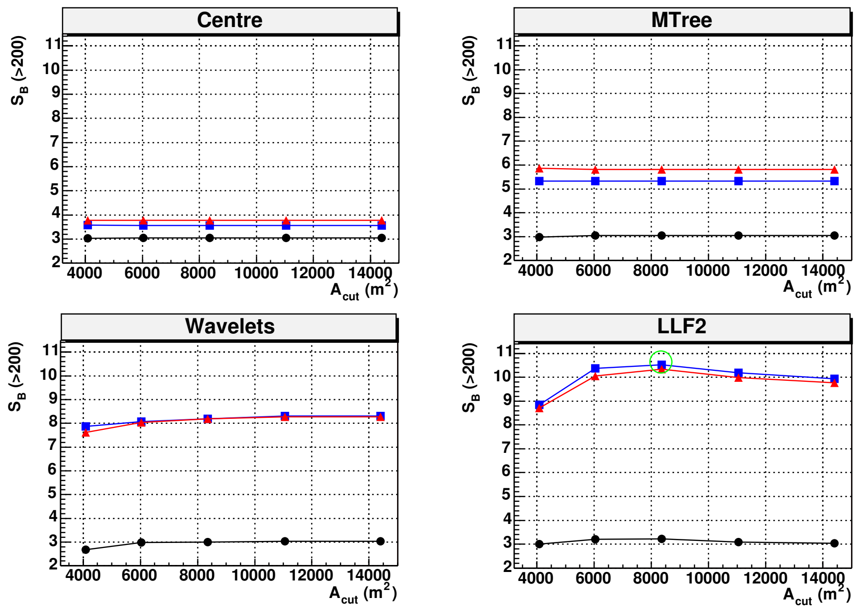

Figure B.16: *Sensitivity (method B) in the multiplicity range >200.*

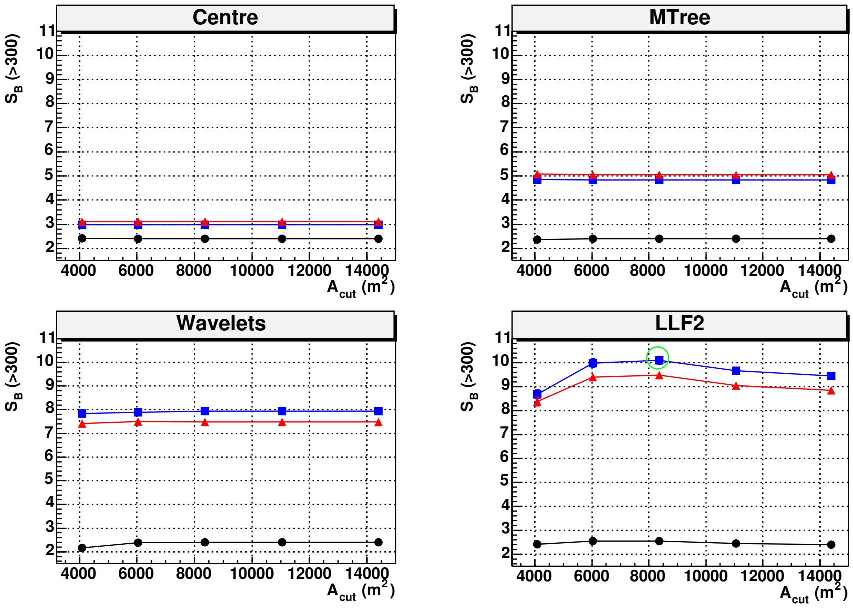

Figure B.17: *Sensitivity (method B) in the multiplicity range >300.*

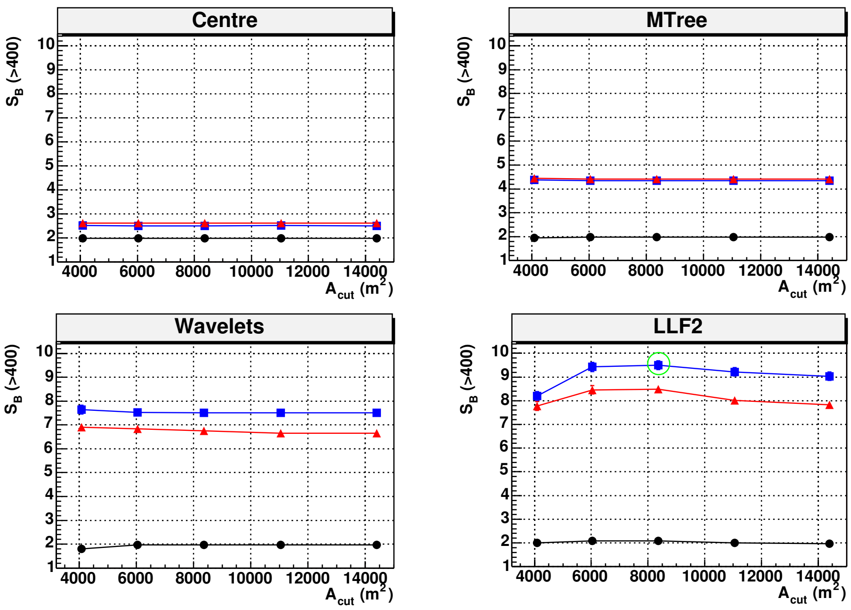

Figure B.18: *Sensitivity (method B) in the multiplicity range >400*

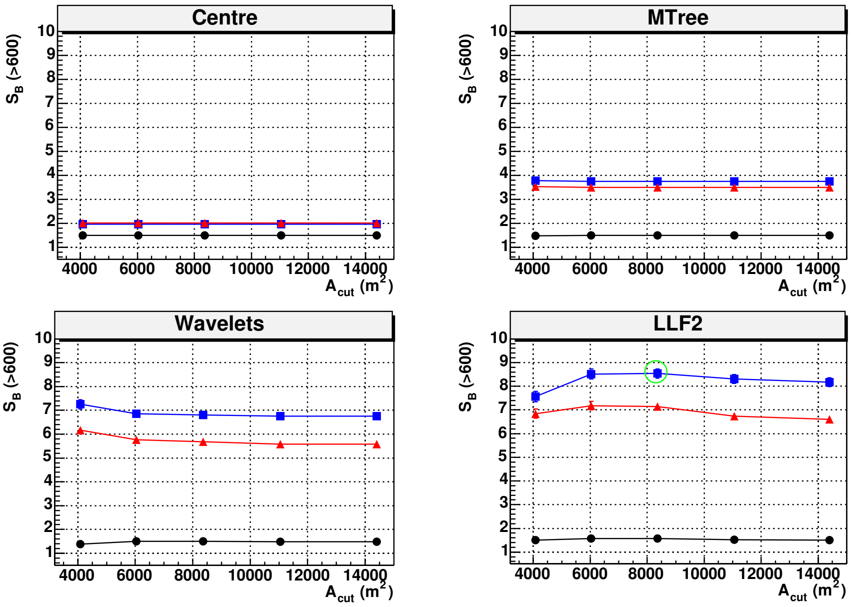

Figure B.19: *Sensitivity (method B) in the multiplicity range >600.*

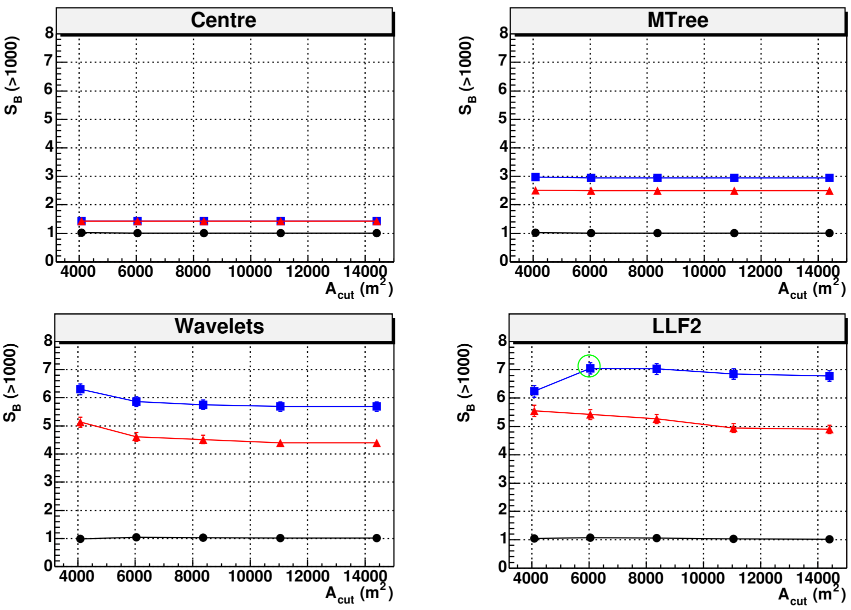

Figure B.20: *Sensitivity (method B) in the multiplicity range >1000.*

Bibliography

[1] C.M. Hoffman et al., Rev. Mod. Phys. **71** (1999) 897;

[2] R. Ong, Int. J. Mod. Phys. **A15S1** (2000) 740;

[3] T.C. Weekes et al., Astrophys. J. **342** (1989) 379;

[4] R. Hartman et al., Astrophys. J. Suppl. Series **123** (1999) 79;

[5] http://cossc.gsfc.nasa.gov/cossc/EGRET.html

[6] R. Ong, summary talk to be published in Proc. of Int. Symposium "Universe viewed in Gamma Rays", Kashiwa (2002) e–print Archive: astro-ph/0304336;

[7] R.D. Blandford & J.P. Ostriker, Astrophys. J. **221** (1978) 29;

[8] E. Fermi Phys. Rev. **75** (1949) 1169;

[9] V.L. Ginzburg & S.I. Syrovatskii, *The origin of Cosmic Rays* , Pergamon Press (1964);

[10] O.C. deJager & A.K. Harding, Astrophys. J. **396** (1992) 161;

[11] F. Aharonian et al, Astrophys. J. **539** (2000) 317;

[12] A.M. Hillas et al., Astrophys. J. **503** (1998) 744;

[13] T. Tanimori et al., Astrophys. J. **497** (1998), L25;

[14] M. Amenomori et al., Astrophys. J. **525** (1999) L525;

[15] L.O'C. Drury, F.A. Aharonian, H.J. Volk, A&A **287** (1994) 959;

[16] C.M. Urry & P. Padovani, PASP **107** (1995) 803;

[17] R.M. Sambruna et. al., Astrophys. J. **463** (1996) 444;

[18] R.D. Blandford & A. Levinson, Astrophys. J. **441** (1995) 79;

[19] L. Maraschi et al., Astrophys. J. **397** (1992) L5;

[20] K. Manheim, A&A **67** (1993), 269;

[21] J. Quinn et al. Astrophys. J. **518** (1999) 693;

[22] C. Itoh et al. A&A **396** (2002) L1;

[23] K.A. Weaver et al., Astrophys. J. **576** (2002) L19;

[24] F. Aharonian et al., A&A **384** (2002) L37;

[25] R. Ong, Phys. Rep. **305** (1998) 93;

[26] W.S. Paciesas, Astrophys. J. Suppl. Series **122** (1999) 465;

[27] R. Atkins et al., Astrophys. J. **533** (2000) L119;

[28] R. Atkins et al., Astrophys. J. **583** (2003) 824;

[29] N. Gehrels et al., Astropart. Phys. **11** (1999) 277;

[30] T.K. Gaisser, *Cosmic Rays and Particle Physics*, Cambridge Un. Press (1990);

[31] B. Rossi, "High Energy Particles", Prentice–Hall (1952);

[32] A.M. Hillas, Proc. of the 19^{th} ICRC (1985), La Jolla;

[33] S. Oser et al., Astroph. J. **547** (2001) 949 ;

[34] S. De Naurois et al., Astroph. J. **566** (2002) 343;

[35] M. Amenomori et al., Nucl. Phys. Suppl. **10B** (1989) 219 ;

[36] M. Amenomori et al., Proc. of the 26^{th} ICRC (1999), Salt Lake City;

[37] www.lanl.gov/milagro

[38] R. Atkins et al., e–print Archive: astro-ph/0305308 (submitted to Astrophys. J.);

[39] G. Sinnis for the Milagro Coll., Proc. of the 28^{th} ICRC (2003) 2583, Tsukuba;

[40] M. Abbrescia et al., Astroparticle Physics with ARGO, Proposal (1996); C. Bacci et al., The ARGO-YBJ Project, Addendum to the Proposal (1998). These unpublished documents can be downloaded at the URL: http://argo.na.infn.it/

[41] S. Mastroianni et al. for the ARGO–YBJ Coll., Proc. of the 28^{th} ICRC (2003) 769, Tsukuba;

[42] C. Bacci et al., NIM A **443** (2000) 342;

[43] C. Bacci et al., Astropart. Phys. **17** (2002) 151;

[44] A. Surdo et al. for the ARGO–YBJ Coll., Proc. of the 28^{th} ICRC (2003) 5, Tsukuba;

[45] G. Mancarella et al., Internal Note **ARGO–YBJ/2000-05** (2000);

[46] C. Bleve et al., Internal Note **ARGO–YBJ/2003-02** (2003);

[47] R. Brun & F. Rademakers, NIM **A389** (1997) 8;

[48] R. Brun et al., *PAW - Physics Analysis Workstation*, CERN Prog. Lib. **Q121** (1993);

[49] S. Bussino, S.M. Mari, Astropart. Phys. **15** (2001) 65;
S. Bussino for the Argo-YBJ Collab., Proc. of the 26^{th} ICRC (1999), Salt Lake City;
C. Bleve Deg. Thesis, Università di Lecce (1999);
F. Salamida, Deg. Thesis, Università di Lecce (2003);

[50] D. Heck, J. Knapp, J.N. Capdevielle, G. Schatz and T. Thouw, Report **FZKA 6019** (1998), Forschungszentrum Karlsruhe; http://www-ik3.fzk.de/~heck/corsika/physics_description/corsika_phys.html

[51] D. Heck and J. Knapp, *Extensive Air Shower Simulation with CORSIKA: A User's Guide (v6.014)*;

[52] W.R. Nelson, H. Hirayama and D.W.O. Rogers, Report **SLAC 265** (1985), Stanford Linear Accelerator Center;

[53] N.N. Kalmykov, S.S. Ostapchenko, Yad. Fiz. **56** (1993) 105; Phys. At. Nucl. **56**(3) (1993) 346; N.N. Kalmykov, S.S. Ostapchenko and A.I. Pavlov, Bull. Russ. Acad. Sci. (Physics) **58** (1994) 1966;

[54] H. Fesefeld, Report **PITHA-85/02** (1985), RWTH Aachen;

[55] R. Brun et al., *GEANT 3.21 - detector description and simulation tool*, CERN Prog. Lib., **W5013** (1993);

[56] D. Martello and A. Surdo, Internal Note **ARGO-YBJ/2000-001** (2000);

[57] T.K. Gaisser et al. Proc. of the 27^{th} ICRC (2001) 1643, Hamburg;

[58] T. Sanuki et al., Astrophys. J. **545** (2000) 1135;

[59] J. Alcaraz et al., Physics Letters B **490** (2000) 27;
J. Alcaraz et. al., Physics Letters B **494** (2000) 193;

[60] J. Buckley et al., Astrophys. J. **429** (1994) 736;

[61] I.P. Ivanenko et al., Proc. of 23^{rd} ICRC (1993), Calgary;

[62] K. Asakimori et al., Astrophys. J. **502** (1998) 278;

[63] K. Greisen, Prog. Cosmic Ray Phys. **3** (1956) 1;

[64] G. Di Sciascio, Internal Note **ARGO–YBJ/2002-02** (2002);

[65] F. James, *MINUIT - Function Minimization and Error Analysis*, CERN Prog. Lib. **D506** (1994);

[66] G. Di Sciascio et al., Astropart. Phys. **6** (1997) 313;

[67] E. Rossi, Deg. Thesis, Università di Napoli (2002)
(also on http://argo.na.infn.it/argo_pub_theses.html);

[68] D. Martello, private communication;

[69] G. Di Sciascio, talk given at the ARGO–YBJ Off–line meeting (2002), Lecce;

[70] D.E. Alexandreas, NIM **A328** (1993) 570.